



Measurement of the Strong Coupling Constant from Inclusive Jet Production at the Tevatron Collider.

A thesis presented to the faculty of
The Rockefeller University
in partial fulfillment of the requirements for
the degree of Doctor of Philosophy

by

Christina Mesropian

2000

Abstract

We present a measurement of the strong coupling constant from a single observable, the inclusive jet cross section. We use 86 pb^{-1} of data collected with the Collider Detector at Fermilab (CDF) from $p\bar{p}$ collisions at $\sqrt{s} = 1800 \text{ GeV}$. The data was analyzed and experimental systematic uncertainties estimated. The measured value $\alpha_s(M_Z) = 0.1129 \pm 0.0001(stat)_{-0.0089}^{+0.0078}(exp.syst)$ is consistent with the world average. The very small statistical error is due to the high statistics jet cross section. The theoretical uncertainties associated with this measurement, which are mainly due to renormalization scale uncertainty and input parton distributions, are estimated to be $\pm 5\%(theor.scale)$ and $\pm 10\%(theor.PDF)$. This is the first measurement which tests the running of α_s over the wide kinematical range in a single experiment from 40 to 450 GeV. The results demonstrate very good agreement with the QCD predictions.

Acknowledgments

I would like to express my gratitude to the entire Rockefeller University Experimental High Energy Physics Group. Especially, I would like to thank Professor Konstantin Goulianos, who gave me an opportunity to join the group and CDF experiment and was constantly supporting my work during all these years.

I would like to thank my research advisor, Professor Anwar Bhatti for his guidance and advice in all aspects of the research. It has been a pleasure to work with him.

I also would like to thank Walter Giele, who proposed the method of α_s measurement from the inclusive jet cross section, provided the program for theoretical calculations, and always took a time to discuss our analysis. I consider myself fortunate for having an opportunity to meet such colleagues as Giorgio Apollinari, Kerstin Borras, Mary Convery, Tim Cox, Luc Demortier, Nikos Giokaris, David Khazins, Stefano Lami and Michelle Galinaro. From working with them I have learned a great deal of experimental physics and professionalism.

My special thanks are due to Anwar Bhatti, Luc Demortier and Dino Goulianos for their extremely careful reading of the manuscript and numerous important corrections, which made this thesis less painful to a reader.

I thank all my colleagues in QCD group of CDF experiment for many discussions and suggestions. Especially, I would like to thank Brenna Flaughner and Joey Huston for their constant interest to this research.

I thank my fellow graduate students Suren Bagdasarov, Kenichi Hatakeyama, Alex Akopian, Andrei Solodsky and Alexey Titov for many physics and non-physics discussions we had and for sharing with me the unforgettable experience of being a graduate student at The Rockefeller University.

This thesis would not have been possible without the dedicated effort of the entire

CDF collaboration. All of the people involved have my sincerest thanks.

My very deep acknowledgments go to the Rockefeller University for providing exceptional research opportunity in New York City and creating unique democratic atmosphere between students and faculty.

I would like to thank director, Marjorie Goldsmith, and teachers at the Child and Family Center at the Rockefeller University for being the most wonderful people caring for my two daughters while I was working on my doctoral thesis.

Finally, my most important acknowledgment is for the love, support and encouragement of my family - my parents, husband and my children.

Contents

Table of Contents	vi
List of Figures	ix
List of Tables	xi
1 Introduction	1
2 Quantum Chromodynamics	5
2.1 Introduction	5
2.2 Basics of Quantum Chromodynamics	7
2.3 Running Coupling Constant	12
The Λ parameter	15
2.4 QCD Formalism for Hard Processes	15
3 Collider Detector at Fermilab	19
3.1 Tevatron	19
3.2 CDF Detector	22
CDF Coordinate System and Units	24
3.2.1 Tracking	24
The Silicon Vertex Detectors	25
The Vertex Time Projection Chamber	25
The Central Tracking Chamber	26
3.2.2 Calorimetry	26
The Central Calorimeters	27
The Plug and Forward Calorimeters	30
3.2.3 Muon Detection	31
3.2.4 Triggers	31

4	The Strong Coupling Constant in Inclusive Jet Production	35
4.1	Jets	36
4.1.1	The Inclusive Jet Cross Section	40
4.1.2	Monte Carlo calculations of jet cross section in hadronic collisions	42
4.2	α_s from the inclusive jet cross section	43
5	Data	47
5.1	Data Selection	47
5.1.1	Trigger Efficiency	50
5.2	Jet Corrections	51
	Calorimetry	53
5.2.1	Response functions	54
	Fragmentation	55
	Charged Pion Response	56
	Neutral Pion Response	56
	Underlying Event Correction	57
	Energy Scale Stability	58
5.3	The Unsmearing and Corrected Cross Section	58
6	Measurement of α_s	63
6.1	Measurement of α_s from the inclusive jet cross section	63
6.2	Measurement of $\alpha_s(M_Z)$	67
	Effect of the heavy quark masses	67
	The average value of $\alpha_s(M_Z)$	69
6.3	Comparison of Results with QCD	70
7	Systematic Uncertainties	75
7.1	Experimental Systematic Uncertainties	75
7.2	Theoretical Uncertainties	82
7.2.1	Choice of the Renormalization scale	84
7.2.2	Parton Distribution Functions	86
	CTEQ4 PDF sets	89
	MRSA' PDF sets	94
	MRS R PDF sets	95
	MRST PDF set	98
8	Summary and Outlook	103
8.1	Status of α_s	103
8.1.1	e^+e^- Annihilation	104
	Hadronic decay width	104

	Event Shape Observables	105
	τ Decays	106
8.1.2	Lepton-Hadron Scattering	107
	Sum rules	108
	Jet rates in ep collisions	109
8.1.3	Heavy Quarkonium Systems	109
	Heavy Quarkonium Decays	110
	Lattice Gauge Theory	110
8.1.4	Hadron-Hadron Collisions	111
	$(W + 1\text{-jet})/(W + 0\text{-jet})$ Ratio in $p\bar{p}$ Collisions	111
	Direct Photon Production in pp and $p\bar{p}$ Collisions	112
8.2	Discussion of Results and Future Outlook	112
8.2.1	Future Plans	114
	Bibliography	125

List of Figures

2.1	Feynman rules for QCD.	10
2.2	Divergent loops.	11
2.3	Running of the strong coupling constant $\alpha_s(Q^2)$ in the leading order approximation.	13
2.4	Typical effects of breaking a hadron	14
2.5	The schematic description of the hard-scattering process.	16
3.1	Schematic Overview of FNAL accelerator complex for $p\bar{p}$ collisions . .	20
3.2	Schematic overview of CDF detector	23
3.3	Calorimeter Segmentation map in $\eta-\phi$. The shaded area shows regions with only partial coverage for the HAD calorimeters, due to the low-beta quadrupole. The black area has no coverage due to the hole for the beampipe.	27
3.4	Layout of the CEM and CHA light-collection systems. The hadronic section is located directly on top of the electromagnetic section.	29
4.1	Lego display of a jet event from CDF.	38
5.1	The trigger efficiencies for jet_100, jet_70, jet_50, and jet_2- triggers. .	51
5.2	The response functions for different E_T^{true} jets.	58
5.3	The ratios of corrected E_T and corrected cross section to the measured E_T and measured cross section.	60
5.4	Corrected inclusive jet cross section	61
6.1	Effects of different renormalization scales on the inclusive jet cross section.	65
6.2	Measurement of $\alpha_s(E_T)$	66
6.3	Comparison of the “running” of the strong coupling constant with theoretical predictions.	73

6.4	Fit of $\alpha_s(M_Z)$ as a function of E_T with a linear function for (top) $E_T < 250$ GeV, (bottom) for all E_T spectrum.	74
7.1	Systematic uncertainties for the inclusive jet cross section.	77
7.2	α_s extracted for different sources of systematic uncertainties.	78
7.3	α_s extracted for different sources of systematic uncertainties.	79
7.4	Systematic uncertainties for α_s measurement.	81
7.5	Estimate of the uncertainty on $\alpha_s(M_Z)$ due to different choices of R_{sep}	83
7.6	Uncertainties due to the change in renormalization scale.	85
7.7	Various processes contributing to the inclusive jet cross section.	88
7.8	The percent difference between the preliminary Run1B inclusive jet cross section and QCD predictions for a variety of current PDFs [39].	91
7.9	α_s using the CTEQ4HJ PDF set.	92
7.10	α_s using the CTEQ4A series.	94
7.11	α_s using the MRSA' series.	95
7.12	α_s using the MRSA' PDF set, input $\alpha_s(M_Z)$ is 0.110.	96
7.13	α_s using the MRS R2 PDF set, input $\alpha_s(M_Z)$ is 0.120.	97
7.14	α_s using the MRST2 PDF set.	99
7.15	$\alpha_s(M_Z)$ as function of E_T using the MRST PDF sets.	100
7.16	α_s extracted for different PDFs.	101
7.17	Uncertainties due to the choice of different PDFs. The bottom boundary corresponds to the CTEQ4A1 set with output $\alpha_s = 0.1102$ and top boundary corresponds to the MRST4 set with output $\alpha_s = 0.1211$	102
8.1	α_s measurement using CTEQ4M parton distributions.	115
8.2	Summary of different measurements of $\alpha_s(M_Z)$. The dashed line corresponds to the world average of $\alpha_s(M_Z)$ with shaded band representing the uncertainty on this value.	116

List of Tables

3.1	Some of the Tevatron parameters determining the luminosity during Run 1B.	22
3.2	The Summary of the CDF Calorimetry.	28
5.1	E_T range and prescale factors (PS) for QCD triggers	49
5.2	Raw cross section at $\sqrt{s}=1800$ GeV	52
5.3	The parameters of the “standard curve”.	59
5.4	CDF corrected inclusive jet cross section from run 1B	62
6.1	Number of active flavors at different scales	68
6.2	The extracted $\alpha_s(E_T)$ and corresponding $\alpha_s(M_Z)$ values with associated statistical uncertainties.	71
7.1	Parameters for systematic error curves.	76
7.2	Experimental systematic uncertainty on the extracted $\alpha_s(M_Z)$ for the CTEQ4M PDF set.	80
7.3	μ -scale uncertainty on the extracted $\alpha_s(M_Z)$ for the CTEQ4M PDF set.	84
7.4	Experimental systematic uncertainty on the extracted $\alpha_s(M_Z)$ for the CTEQ4HJ PDF set.	93
7.5	The various MRST PDF sets used in the analysis.	98

Chapter 1

Introduction

Quantum Chromodynamics (QCD) is the theory of interacting quarks and gluons, which are the fundamental constituents of hadrons. Although widely accepted as the most successful theory of strong interactions for last three decades, QCD still lacks good understanding of quark-gluon interactions at large distances, low momentum transfers, mostly due to the mathematical complexity of the theory and the non-applicability of perturbative methods at this range. Despite mentioned difficulties Quantum Chromodynamics achieved remarkable success in describing hadron interactions at short distances, i.e. large momentum transfers, owing to the property of asymptotic freedom - weakening of interaction at short distances. Asymptotic freedom allows the application of well developed perturbative methods to processes between quarks and gluons. Using perturbative techniques any process can be presented as an expansion in powers of α_s , the strong coupling constant. α_s , which reflects the intensity of strong interactions, is a fundamental free parameter of the theory and must be measured from experiment.

Therefore, the determination of the strong coupling constant is the central measurement of Quantum Chromodynamics.

One of the striking features of Quantum Chromodynamics is the “running” of the strong coupling constant, namely, weakening of α_s with decreasing distance. The strong coupling constant has been measured by different experiments and at different energy scales, ranging from 1 GeV in measurements of structure functions in deep-inelastic scattering (DIS), all the way to 189 GeV at LEP-2. The consistency of the various measurements is remarkable: α_s is indeed a universal parameter.

Although numerous measurements of α_s were made at single energy scale, there are only few results providing proof of the “running” of the coupling constant and only in a limited momentum transfer range. Therefore, it is very important to test α_s dependence on energy scale for wide range of momentum transfers based on the single source of experimental data.

The best possibility of measuring α_s over extended momentum transfer range lies with jet production in hadron collisions. Appearance of jets, collimated sprays of hadrons produced in particle collisions, is one of the characteristic features of QCD. In hadron-hadron collisions, jet production can be understood as resulting from point-like collisions of a quark or gluon from one hadron with a quark or gluon from the other hadron. From jet studies one can obtain information about parent quarks and gluons. The high energies at which jets are produced provide an excellent opportunity to test perturbative QCD.

With the high luminosity runs at the Tevatron, when the CDF experiment collected 89 pb⁻¹ of data during 1994-1996, a new period started with the emphasis being placed on precision measurements. QCD tests in $p\bar{p}$ collisions may not be as clean as those at e^+e^- annihilations, partly due to the complications associated with partons in the initial state and the beam fragments. However, the variety and diversity of hard processes, together with the enormous energy reach, provide us

with a potential not accessible in current e^+e^- experiments. A measurement of the strong coupling constant at the Tevatron cannot be overestimated: it can provide an extension of the α_s measurements to the largest values of momentum transfers available, and contribute to the reduction of uncertainties in other studies at Fermilab.

In this dissertation we present a measurement of the strong coupling constant from inclusive jet production in $p\bar{p}$ collisions at $\sqrt{s}=1.8$ TeV. Our analysis is based on the method proposed by W. Giele *et al.* [1]. This is the first determination of α_s at the Tevatron, and the first measurement demonstrating the running of the strong coupling constant in the wide energy range from 40 to 450 GeV. The results of this study were included in the Review of Particle Physics 2000 by Particle Data Group [2] and reported at numerous international conferences [3]-[5].

The dissertation is organized as follows: in Chapters 2 and 3 we present two fundamental components of this study by giving overview of basics of Quantum Chromodynamics and describing in detail the experimental apparatus, Tevatron and CDF detector. In Chapter 4 we describe the process of interest, jet production in $p\bar{p}$ collisions, and present the method used for α_s extraction from the inclusive jet cross section. In Chapter 5 we explain how the data were collected and what triggers were used. In the same chapter we also provide a description of the method used by the CDF collaboration to correct the data for jet energy mismeasurements and for the effects of the finite energy resolution on the inclusive jet cross section. In Chapter 6 we present the results of the α_s measurement from the inclusive jet cross section in $p\bar{p}$ collisions at $\sqrt{s}=1800$ GeV, and compare our results with the theory. Chapter 7 is devoted to the analysis of experimental systematic uncertainties associated with this measurement, and the sensitivity of the results to various sources of theoretical uncertainties. In Chapter 8 we discuss our measurement in the context of the current

status of α_s and review future prospects for the determination of the strong coupling constant at the Tevatron.

Chapter 2

Quantum Chromodynamics

Quantum Chromodynamics (QCD) is the theory of the strong interaction, one of the four fundamental forces in nature. It describes the interactions between quarks and gluons, which are the basic constituents of hadrons. QCD made its appearance as a mathematically consistent theory in the 1970s, and presently is considered as one of the cornerstones of the “Standard Model” of the elementary particles and their interactions. The birth of QCD was the result of the assembling of many ideas and experimental results, which we will review below.

2.1 Introduction

In 1963, Gell-Mann and Zweig [6] introduced a model that explained the spectrum of particles that undergo strong or nuclear interaction in terms of fundamental constituents called *quarks*. According to their model mesons were expected to be quark-antiquark bound states, and baryons were interpreted as bound states of three quarks. To explain the electric charges and other quantum numbers of hadrons it was necessary to assume three species of quarks, up (u), down (d), and strange

(*s*). Additional discoveries since that time required the existence of the three more species: charm (*c*), bottom (*b*), and top (*t*). To make baryons with integer charges, the quarks needed to be assigned fractional electric charges: $+2/3$ for *u, c, t*, and $-1/3$ for *d, s, b*. For example, the proton would be a bound state of *uud*, and the neutron would be a bound state of *udd*. The six types of quarks are conventionally referred to as *flavors*.

Despite the success of the quark model it had serious problems. Assuming that quarks carry only the quantum numbers described by the model, the existence of bound states of three identical quarks such as Δ^{++} , violates the Pauli principle. To reconcile the baryon spectrum with Fermi-Dirac statistics, Greenberg, Han and Nambu [7] proposed that quarks carry an additional quantum number, called *color*.

Another approach to the quark model came from results of experiments probing the structure of an individual proton by scattering high-energy charged lepton, or deep-inelastic (DIS) experiments in which so called *Bjorken scaling* was observed. Bjorken scaling is, essentially, the statement that the structure of the proton looks the same to an electromagnetic probe no matter how hard the proton is struck. To explain the results of the experiment Bjorken and Feynman came up with the following simple model [9]. One can assume that the proton contains point-like constituents, called *partons*. Bjorken scaling implied that during rapid scattering process, when the transit time across target is less than the time scale of internal motion, interactions among partons can be ignored. We might imagine that partons are approximately free particles over very short time scales corresponding to energy transfers of a few GeV or more, although they have strong interactions on longer time scales. The parton model was simple, but it suggested a conflict between the observation of almost free particles and the basic principles of quantum field the-

ory. Thus the stage was set for the search for a quantum field theory suitable to describe the strong interaction. The appropriate theory turned out to correspond to the Yang-Mills fields [10], which were introduced in 1954, and were a theory of non-Abelian fields that interact with one another as well as with external matter. In contrast to the familiar example of Quantum Electrodynamics, the coupling constant of a Yang-Mills theory can become weak at large momenta. This kind of behavior is called *asymptotic freedom*, and was demonstrated in the early 1970's by 't Hooft, Politzer, Gross and Wilczek [11]. This result made use of the *renormalization group* concept [12], which specifies the dependence of quantum field theory parameters on scale variations. The theory of the strong interactions based on a Yang-Mills quantum field acting on the color degrees of freedom has come to be known as *Quantum Chromodynamics* or QCD. The quanta of QCD are called *gluons*, since they provide the “glue” holding hadrons together.

2.2 Basics of Quantum Chromodynamics

Strong interactions are described by a local non-Abelian gauge theory of quarks and gluons in which SU(3) is the gauge group and gluons are the gauge bosons. Three colored quarks form a triplet in the fundamental representation of SU(3) and eight gluons form an octet in the adjoint representation. The QCD Lagrangian is

$$\mathcal{L} = \mathcal{L}_{Yang-Mills} + \mathcal{L}_{gauge} + \mathcal{L}_{ghost}, \quad (2.1)$$

$$\mathcal{L}_{Yang-Mills} = -\frac{1}{4}F_{\mu\nu}^{(a)}F^{(a)\mu\nu} + \sum_f \bar{\psi}^f [\not{D} - m_f] \psi^f, \quad (2.2)$$

where the index f labels the flavor ($f = u, d, c, s, t, b$), m_f is the quark mass, a refers to color and assumes the values $1, \dots, N_c - 1$, $N_c = 3$ being the number of colors.

$$\not{D} = (\gamma)_{\beta, \alpha}^{\mu} (D_{\mu})_{ij} \quad (2.3)$$

$$(D_{\mu})_{ij} = \delta_{ij} \partial_{\mu} - ig T_{ij}^a A_{\mu}^a \quad (2.4)$$

$$F_{\mu\nu}^{(a)} = \partial_{\mu} A_{\nu}^a - \partial_{\nu} A_{\mu}^a + g_s f_{abc} A_{\mu}^b A_{\nu}^c \quad (2.5)$$

where D is the covariant derivative acting on the quark field. $F_{\mu\nu}^{(a)}$ is the non-Abelian field strength tensor derived from the gluon field A_{μ}^a , T^a are the $SU(3)$ generators, and g is the coupling constant which determines the strength of the interaction between colored quanta. f_{abc} are the structure constants of $SU(3)$ defining its *Lie algebra* in the commutation relationship

$$[T_a, T_b] = if_{abc} T_c \quad (2.6)$$

The QCD Lagrangian should be invariant under local gauge transformations, which means that the phase convention for a particle wavefunction can be set independently at each space-time point x . The importance of the gauge invariance property consists in the following: first, it requires the equality of the coupling constants g describing the quark interactions with gluons and gluon self-interactions; second, non-Abelian theories are renormalizable (i.e. calculable) only when they are gauge invariant; third, only non-Abelian theories can have the property of asymptotic freedom.

However the process of quantization of Yang-Mills fields requires a choice of gauge. The gauge fixing term is

$$\mathcal{L}_{gauge} = -\frac{\lambda}{2} (\partial^{\mu} A_{\mu}^a)^2 \quad 1 < \lambda < \infty \quad (2.7)$$

This expression defines a set of *covariant* gauges, the most familiar being the *Feynman gauge* ($\lambda = 1$). Introduction of a gauge fixing term breaks the gauge invariance of the Lagrangian. Due to gluons self-interactions the Lagrangian allows the production of unphysical states. The general method to solve this problem was introduced by Faddeev and Popov [13] and requires the addition of a *ghost* term to the QCD Lagrangian

$$\mathcal{L}_{ghost} = (\partial^\mu \bar{c}^a)(\partial_\mu \delta^{ac} - gf^{abc} A_\mu^b) c^c \quad (2.8)$$

where c_a and \bar{c}_a are scalar ghost and antighost fields. The ghost fields anticommute, despite their integer spin. The general physical interpretation of Faddeev-Popov ghosts is that they are unphysical particles acting as negative degrees of freedom to cancel the effects of unphysical states introduced by gauge-fixing term¹.

The Lagrangian needed to derive the Feynman rules in a covariant gauge is a sum of equations 2.2, 2.7, and 2.8:

$$\mathcal{L} = -\frac{1}{4} F_{\mu\nu}^{(a)} F^{(a)\mu\nu} + \sum_f \bar{\psi}^f [\not{D} - m_f] \psi^f - \frac{\lambda}{2} (\partial^\mu A_\mu^a)^2 + (\partial^\mu \bar{c}^a)(\partial_\mu \delta^{ac} - gf^{abc} A_\mu^b) c^c \quad (2.9)$$

The Feynman rules for QCD are summarized in Fig. 2.1.

However all quantities calculated according to the rules are suffering a severe problem after including diagrams with loops (Fig. 2.2). Since loop momenta can be arbitrary, the integral becomes divergent. This type of divergences are called ultra-violet (UV). To make the results of theory usable in practice, the procedure of reinterpreting infinite quantities in terms of physical ones, known as *renormalization* was used. The conversion of UV divergences to finite experimentally measurable quantities can be divided on two steps. First, the divergent expressions are

¹We will not discuss *axial gauges* which allow gauge-fixing with the advantage of not requiring ghost fields. The price for this simplicity is a very complicated gluon propagator.

$$a, \alpha \text{---}\overbrace{\text{wavy}}^p\text{---} b, \beta = \delta^{ab} \left[-g^{\alpha\beta} + (1 - \lambda) \frac{p^\alpha p^\beta}{p^2 + i\epsilon} \right] \frac{i}{p^2 + i\epsilon}$$

$$a \text{---}\overbrace{\text{dashed}}^p\text{---} b = \delta^{ab} \frac{i}{p^2 + i\epsilon}$$

$$i, n \xrightarrow{p} k, m = \delta^{ik} \frac{i}{\not{p} - m + i\epsilon} \Big|_{mn}$$

$$\begin{array}{c} b, \beta \\ | \\ \text{wavy } q \\ / \quad \backslash \\ \text{wavy } p \quad \text{wavy } r \\ a, \alpha \quad c, \gamma \end{array} = -g f^{abc} \left[g^{\alpha\beta} (p - q)^\gamma + g^{\beta\gamma} (q - r)^\alpha + g^{\gamma\alpha} (r - p)^\beta \right]$$

$$\begin{array}{c} a, \alpha \quad b, \beta \\ \backslash \quad / \\ \text{wavy} \\ / \quad \backslash \\ c, \gamma \quad d, \delta \end{array} = -ig^2 f^{xac} f^{xbd} (g^{\alpha\beta} g^{\gamma\delta} - g^{\alpha\delta} g^{\beta\gamma}) \\ - ig^2 f^{xad} f^{xbc} (g^{\alpha\beta} g^{\gamma\delta} - g^{\alpha\gamma} g^{\beta\delta}) \\ - ig^2 f^{xab} f^{xcd} (g^{\alpha\gamma} g^{\beta\delta} - g^{\alpha\delta} g^{\beta\gamma})$$

$$\begin{array}{c} a, \alpha \\ | \\ \text{wavy } q \\ / \quad \backslash \\ \text{dashed } b \quad \text{dashed } c \end{array} = g f^{abc} q^\alpha$$

$$\begin{array}{c} a, \alpha \\ | \\ \text{wavy } q \\ / \quad \backslash \\ \text{solid } i, n \quad \text{solid } k, m \end{array} = -ig t_{ki}^a \gamma_{mn}^\alpha$$

Figure 2.1: Feynman rules for QCD.

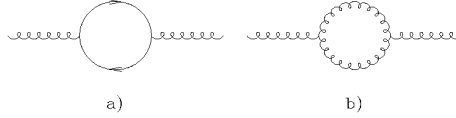


Figure 2.2: Divergent loops.

made mathematically “finite” by special procedure, called *regularization* scheme. All schemes introduce some parameter (ϵ , or λ), such that the original infinite integral is recovered with $\lambda \rightarrow \infty$ ($\epsilon \rightarrow 0$), but such that the integral is finite for finite λ (non-zero ϵ). The most commonly used method of regularization is the dimensional regularization, where the space-time dimension is set to when space-time dimension $D = 4$ can be substituted by $D = 4 - \epsilon$. This substitution will make the integral finite for arbitrary ϵ , except in the limit $\epsilon \rightarrow 0$, where the new expression will behave exactly as the original divergence. The other broadly used regularization schemes are the ultraviolet cut-off method and mass (Pauli-Villars) regularization.

In the next step, regularized divergences of the theory are removed by absorbing them into definitions of physical quantities through a *renormalization procedure*. This is done by some specified, although arbitrary prescription, which introduces a new dimensional scale μ . There are different renormalization schemes. The *momentum point subtraction* requires a specific form for the propagator at some point in momentum space. Two renormalization schemes are specifically linked to dimensional regularization: the *minimal subtraction* MS , and *modified minimal subtraction* \overline{MS} schemes by Bardeen, Buras, Duke, and Muta (1978). We will use \overline{MS} scheme throughout our analysis. All renormalization prescriptions must lead to the same observable amplitudes.

2.3 Running Coupling Constant

In order to introduce the concept of a running coupling α , let us consider a dimensionless physical observable G that can be expanded as a power series in α , assumed to be dimensionless, with possible UV divergent coefficients:

$$G = G(\alpha, Q^2, s_1, s_2 \cdots, s_n), \quad (2.10)$$

G depends on a single energy scale Q , the coupling α , and some invariants $s_1 \cdots s_n$ constructed out of the momenta and masses of the process in question. In the process of calculation we will be required to remove UV divergences by performing renormalization, which will introduce a second scale μ . However μ is an arbitrary parameter, therefore the physical quantity G cannot depend on it. The equation expressing the invariance of G under changes of the parameter μ is known as the *Renormalization Group Equation* (RGE)².

$$\mu^2 \frac{d}{d\mu^2} G(Q^2/\mu^2, \alpha) \equiv \left[\mu^2 \frac{\partial}{\partial \mu^2} + \mu^2 \frac{\partial \alpha}{\partial \mu^2} \frac{\partial}{\partial \alpha} \right] G = 0. \quad (2.11)$$

By introducing the notation

$$t = \ln\left(\frac{Q^2}{\mu^2}\right), \quad (2.12)$$

$$\beta(\alpha) = \mu^2 \frac{\partial \alpha}{\partial \mu^2}, \quad (2.13)$$

Eq. 2.11 changes to

$$\left[-\frac{\partial}{\partial t} + \beta(\alpha) \frac{\partial}{\partial \alpha} \right] G(e^t, \alpha) = 0 \quad (2.14)$$

To solve this equation we define a new function, the *running coupling* $\alpha_s(Q^2)$:

$$t = \int_{\alpha}^{\alpha_s(Q^2)} \frac{dx}{\beta(x)}, \quad \alpha_s(\mu^2) \equiv \alpha. \quad (2.15)$$

²Since G is a dimensionless quantity, μ can appear in the equation only in the ratio Q^2/μ^2 .

We can see that

$$\frac{\partial \alpha_s(Q^2)}{\partial t} = \beta(\alpha_s(Q^2)), \quad (2.16)$$

$$\frac{\partial \alpha_s(Q^2)}{\partial \alpha} = \frac{\beta(\alpha_s(Q^2))}{\beta(\alpha)}, \quad (2.17)$$

and hence $G(1, \alpha_s(Q^2))$ is a solution of Eq. 2.14. As we can see all the scale dependence in G enters through the running coupling constant $\alpha_s(Q^2)$.

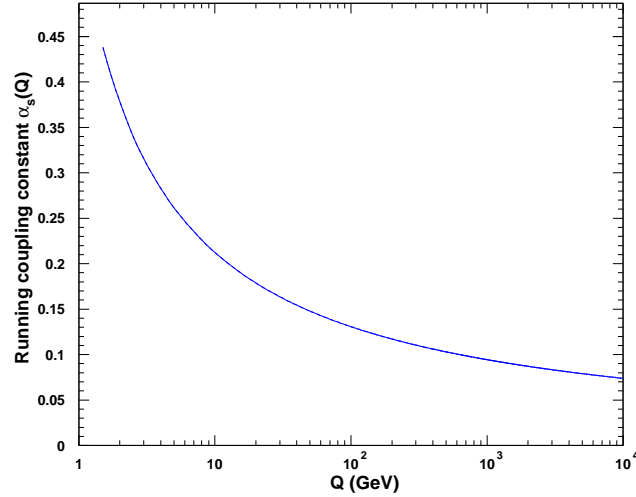


Figure 2.3: Running of the strong coupling constant $\alpha_s(Q^2)$ in the leading order approximation.

The β function has a perturbative expansion

$$\beta(\alpha_s) = -b_0 \alpha_s^2 (1 + b' \alpha_s + b'' \alpha_s^2 + \mathcal{O}(\alpha_s^3)). \quad (2.18)$$

We should note that the sign of b_0 is crucial: with the opposite sign the coupling constant increases as in the case of Quantum Electrodynamics. If we truncate this series to the first term only the expression for α_s relative to some fixed scale M is as follows:

$$\alpha_s(Q^2) = \frac{\alpha_s(M^2)}{1 + \beta_0/(4\pi) \alpha_s(M^2) \log(Q^2/M^2)}. \quad (2.19)$$

Here $\beta_0 = 3N - \frac{2}{3}n_f$, where $N = 3$ is the number of colors and $n_f = 5$ or 6 is the number of “active” flavors. Analyzing this dependence in Fig. 2.3 we can see that as $Q^2 \rightarrow \infty$ $\alpha_s(Q^2) \rightarrow 0$. The theory therefore approaches a free theory in the ultraviolet region. This property is called “*asymptotic freedom*”, which is an essential ingredient of the parton approach to the structure of hadrons. Asymptotic freedom explains why the methods of perturbation theory are useful at high energy, with the coupling constant becoming smaller at large Q^2 .

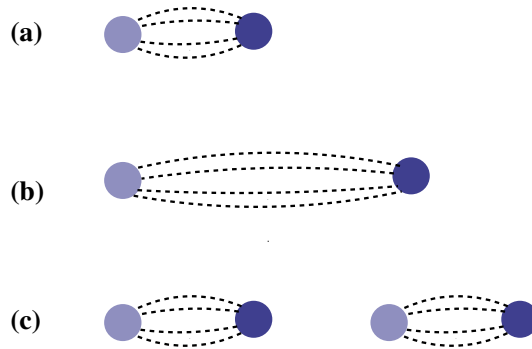


Figure 2.4: Typical effects of breaking a hadron

The other important consequence of Eq. 2.19 is that $\alpha_s(Q^2) \rightarrow \infty$ as $Q^2 \rightarrow 0$, so that perturbation techniques are not valid at small Q^2 . Due to gluon self-coupling, the coupling between quarks increases with their separation. The exchanged gluons attract each other (unlike photons in QED), so the color lines of force are constrained to a tube-like region between the quarks. The tubes have a constant energy density per unit length, thus the potential energy of the interaction increases with the distance, so the partons can never escape from the hadron. This so-called *infrared slavery* is believed to be the origin of the *confinement* mechanism (see Fig. 2.4) and explains why we do not observe free quarks and gluons [14].

As can be seen from Eq. 2.19 perturbative QCD predicts how the coupling constant varies with the scale, but does not give the value of α_s itself. The latter

has to be obtained from the experiment. To compare different values of coupling constant extracted from different experiments we should set common conventions. The convenient reference scale is chosen as the mass of the neutral weak boson Z_0 with \overline{MS} scheme as fixed renormalization scheme. The resulting standard coupling constant is called $\alpha_{s\overline{MS}}(M_Z)$.

The Λ parameter

The alternative approach, which was adopted historically and is still convenient for many purposes, is to introduce a dimensional parameter Λ . One way to define it is as the constant of integration

$$\ln \frac{Q^2}{\Lambda^2} = - \int_{\alpha_s(Q^2)}^{\infty} \frac{dx}{\beta(x)}. \quad (2.20)$$

Λ represents the order of scale at which $\alpha_s(Q^2)$ becomes strong and perturbative theory breaks down. However, values of Λ , which are in the neighborhood of 200 MeV, depends on the precise definition of number of flavors and the choice of renormalization scheme. Thus the preference is given to the $\alpha_s(M_Z)$ as the reference value for different measurements.

2.4 QCD Formalism for Hard Processes

We now turn to the description of hadron interactions such as proton-antiproton collisions. According to the parton model hadrons are composed of many pointlike particles called partons. The basic diagram of the process, $AB \rightarrow CX$, is shown in Fig. 2.5. The inelastic collision between incoming hadrons A and B with momenta P_A and P_B can be described as an elastic collision of parton a from hadron A with parton b from hadron B , producing partons c and d , which can be the

same as a and b . The momenta of a and b are parametrized as $x_a P_A$ and $x_b P_B$ with $0 \leq x_a, x_b \leq 1$. The non-colliding partons in the hadrons are called *spectator* partons or beam *fragments*. The *factorization* theorem of QCD states that the cross section of the hard scattering process can be *factorized* into two parts, a “hard” part describing the colliding partons, which can be calculated in perturbative QCD thanks to asymptotic freedom, and a “soft” part which carries information about the incoming partons. This information is contained in the parton distribution functions (PDF) $f_A^a(x_a)$ and $f_B^b(x_b)$, which are probability densities of partons inside hadron.

Here we have to define the *factorization* scale μ_F , which is the scale that separates “hard” and “soft” physics. This is a parameter that should be chosen to be of the order of the hard scale Q^2 characteristic of the parton-parton interaction. A parton emitted with a transverse momentum smaller than the μ_F -scale is included in the hadron structure whereas a parton emitted with large transverse momentum is part of the short-distance cross section.

Using the factorization theorem these two ingredients can be combined to calculate the cross-section of interest: The cross section would be:

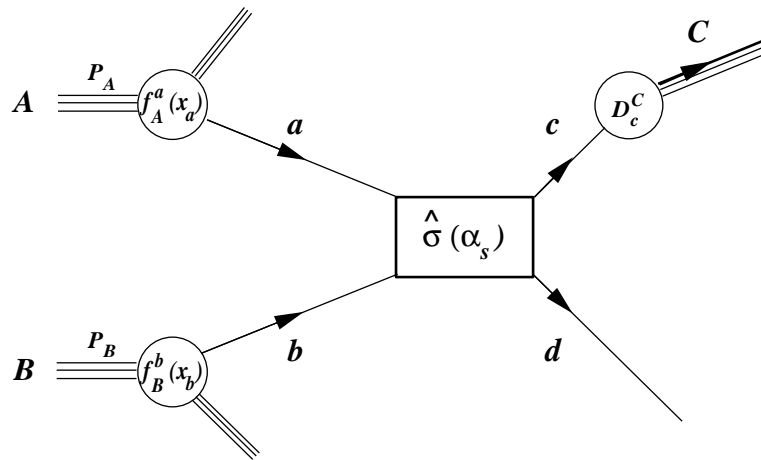


Figure 2.5: The schematic description of the hard-scattering process.

$$E_C \frac{d\sigma}{d^3p_C}(AB \rightarrow CX) = \sum_{abcd} \int_0^1 dx_a \int_0^1 dx_b f_A^a(x_a, \mu^2) f_B^b(x_b, \mu^2) \frac{1}{\pi z_c} \hat{\sigma} D_c^C(z_c). \quad (2.21)$$

The characteristic scale of the interaction is denoted by Q^2 . The functions $f_A^a(x, \mu^2)$ are the non-perturbative parton distribution functions describing the probability density to find a parton of type a carrying a fraction x of the hadron A momentum, and defined at the factorization scale μ . The “hard” part (differential cross section) is denoted by $\hat{\sigma} = \frac{d\sigma}{dt}(ab \rightarrow cd)$, where \sqrt{t} is the invariant momentum transfer for the parton sub-process $ab \rightarrow cd$.

The PDFs are usually obtained by parametrizing data from various scattering experiments at the scale Q_0 . The evolution of quark and gluon distribution functions (G_q, G_g) from one scale to another can be calculated using the Altarelli-Parisi equations:

$$\frac{dG_{q_i}(x, Q^2)}{dt} = \frac{\alpha_s(Q^2)}{2\pi} \int_x^1 \frac{dy}{y} [P_{qq}(x/y)G_{q_i}(y, Q^2) + P_{qg}(x/y)G_g(y, Q^2)] \quad (2.22)$$

$$\frac{dG_g(x, Q^2)}{dt} = \frac{\alpha_s(Q^2)}{2\pi} \int_x^1 \frac{dy}{y} [P_{gq}(x/y)G_{q_i}(y, Q^2) + P_{gg}(x/y)G_g(y, Q^2)] \quad (2.23)$$

where $t = \ln Q^2$ and the P functions are *splitting* functions (for example, P_{qq} is the quark \rightarrow quark splitting function, describing the probability of a quark turning into a quark.)

Colored quarks and gluons can be regarded as free during a hard collision, but subsequently, because of confinement, color forces will organize them into colorless hadrons, this process being called *fragmentation* or *hadronization*. In our scheme it corresponds to the transformation of parton c into hadron C . Typically it involves the creation of additional quark-antiquark pairs by the color force field, and at sufficiently high energies one expects the occurrence of *jets*, bunches of hadrons which all move in similar directions.

Fragmentation is governed by soft non-perturbative processes that have to be described semi-empirically, guided by general principles. For a hadron C produced by a parton c the probability to have momentum in the range from z to $z + dz$ is given by $D_c^C(z)dz$, where $D_c^C(z)$ is called *fragmentation* function. The evolution of fragmentation functions is described by equations analogous to the Altarelli-Parisi equations.

Chapter 3

Collider Detector at Fermilab

Almost all of the results in particle physics in the past half a century have been crucially dependent on continued progress in the development of accelerators at higher and higher energies and associated detector equipment. High energies are necessary for two reasons: first, in order to localize the study to very small distance scales, one has to be able to produce the smallest possible wavelengths and highest energies; second, many of the fundamental particles have large masses and require high energies for their creation and study. In this chapter we will describe the Tevatron collider and the CDF detector - the experimental apparatus used in our study.

3.1 Tevatron

The Tevatron at the Fermi National Accelerator Laboratory is currently the world's highest energy particle collider. It is a superconducting synchrocyclotron, two kilometers in diameter, which accelerates protons and antiprotons in opposite directions and brings them into head-on collision. The Tevatron is the final stage of an acceleration process involving several individual accelerators. Fig. 3.1 shows

an overview of the various machines used to accelerate, store and collide beams of protons and antiprotons at Fermilab.

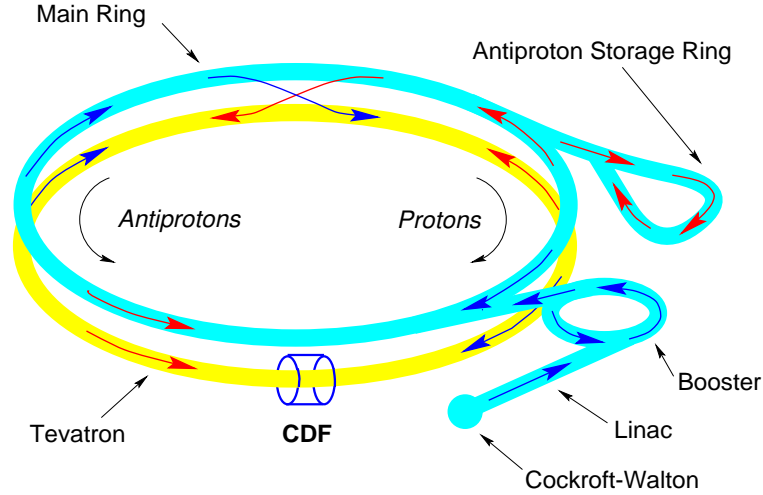


Figure 3.1: Schematic Overview of FNAL accelerator complex for $p\bar{p}$ collisions

The accelerator chain begins with charged negative ions of hydrogen (H^-), which are accelerated by a Cockcroft-Walton electrostatic accelerator to 750 KeV. These ions are fed via a transport line into the 500 feet long linear accelerator (LINAC), which consists, as well as all subsequent accelerators, of resonating RF cavities. The LINAC boosts the energy of hydrogen ions to 400 MeV. Then the H^- ions pass through a carbon foil, where both electrons are stripped off, leaving only bare protons, which are injected into the Booster, an 8 GeV synchrotron, 500 feet in diameter. Once at 8 GeV, the protons are extracted and transferred to the synchrotron, called the Main Ring. The Main Ring, which can achieve a maximum energy of 400 GeV per beam, occupies the same tunnel as the Tevatron and is similar to the Tevatron, except that it uses conventional copper-coiled magnets. The Main Ring is currently used to boost protons for the Tevatron and to provide primary protons to the antiproton source.

To produce antiprotons, the protons are accelerated to 120 GeV in the Main Ring and then directed onto a nickel target, producing roughly 1 antiproton for every 10^5 protons striking the target. The antiprotons are collected in the Debuncher Ring where they are stochastically cooled before being stored in the Accumulator. This process continues for several hours until a sufficient number of antiprotons is available for later injection into the Tevatron. About 5×10^{10} antiprotons are made per hour.

The antiproton beam is transferred to the Main Ring where it is accelerated to 150 GeV before being injected into the Tevatron. The proton beam is also injected into the Tevatron in the opposite direction. The Tevatron accelerates both beams to an energy of 900 GeV and circulates them in the same magnetic and RF fields in helical orbits. During collider Run 1B, the Tevatron was operated with the colliding beams grouped into six bunches each of protons and antiprotons. Electrostatic separators keep the proton and antiproton beams in different helical orbits to minimize the spreading of the beams from interaction. Quadrupole magnets focus the beams to collide at the interaction points, by minimizing the beam's beta function, β , used to characterize the beam's width and its change during circulation in the accelerator. The beams in the center of the CDF detector (B0 point) are roughly circular in the transverse plane, and have RMS spreads of σ_p and $\sigma_{\bar{p}}$. Longitudinally, the beam bunches are approximately Gaussian in shape with a width of σ_l .

One of the most important characteristics of colliding beams in an accelerator is the luminosity, \mathcal{L} , which is defined by:

$$\mathcal{L} = \frac{N_p N_{\bar{p}} B f}{2\pi(\sigma_p^2 + \sigma_{\bar{p}}^2)} \mathcal{F}(\sigma_l/\beta^*) \quad (3.1)$$

where B is the number of bunches (6), N_p and $N_{\bar{p}}$ are the numbers of protons and antiprotons per bunch, f is the revolution frequency (~ 57.3 kHz), \mathcal{F} is a form factor

Table 3.1: Some of the Tevatron parameters determining the luminosity during Run 1B.

\mathcal{F}	σ_l	σ_p or $\sigma_{\bar{p}}$	β^*	N_p	$N_{\bar{p}}$
~ 0.6	0.6m	$\sim 35\mu\text{m}$	0.35m	$1\text{-}2\times 10^{11}$	$4\text{-}7\times 10^{10}$

which is a function of σ_l , and β^* is the value of the beta function at the interaction point. Typical values of these parameters for Run 1B are given in Table 3.1. The average luminosity during Run 1B was around $1.6\times 10^{31}\text{cm}^{-2}\text{s}^{-1}$, with peak luminosity reaching $2.8\times 10^{31}\text{cm}^{-2}\text{s}^{-1}$.

As the proton/antiproton beams circle around, N_p and $N_{\bar{p}}$ decrease due to the collisions with each other and with the gas in the beam pipe (the beam also undergoes emittance growth, an increase in its width). Thus, the luminosity decreases with time, dropping by an order of magnitude after 10-12 hours. When the luminosity becomes unacceptably low, the remaining beams are dumped.

3.2 CDF Detector

The CDF detector is a general purpose detector (see Fig 3.2) designed to study $p\bar{p}$ collisions at the Fermi National Accelerator Laboratory's Tevatron Collider. The detector covers nearly 4π in solid angle with both azimuthal and forward/backward polar symmetry. Event analysis is based on particle energy, momentum, position and charge measurements. Particles coming from the interaction point encounter in sequence tracking detectors, sampling calorimeters and muon detectors.

Tracks are bent by a solenoidal magnetic field of about 1.4 Tesla, generated by a superconducting solenoidal magnet, 3 m in diameter and 4.8 m long. Events

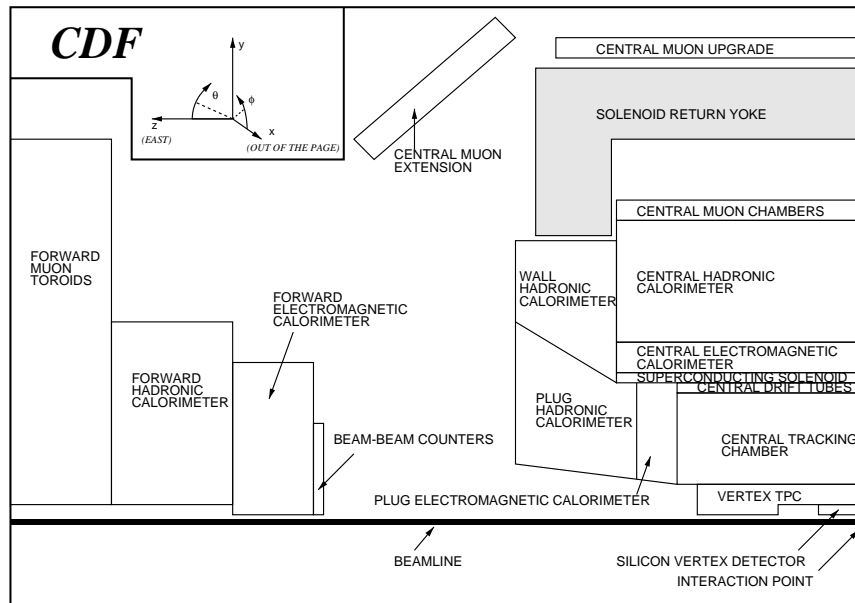
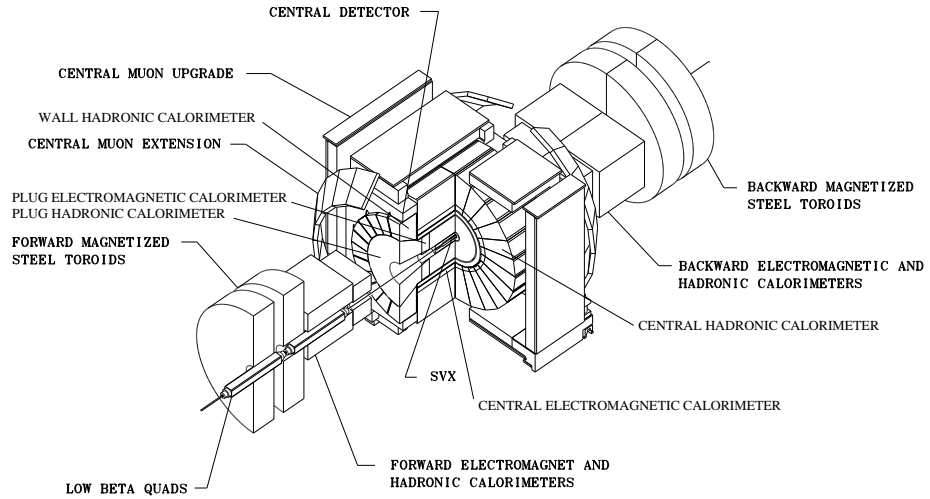


Figure 3.2: Schematic overview of CDF detector

are analyzed in short time (a few microseconds) by a powerful and flexible trigger system. A detailed description of CDF detector components can be found in [15]. In this chapter we will briefly discuss the full detector and describe the detector subsystems which are relevant to our analysis in more detail.

CDF Coordinate System and Units

CDF employs a conventional right-handed coordinate system with positive z -axis along the beam line in the proton direction (East), the positive y -axis pointing vertically upwards and the positive x -axis pointing outwards in the horizontal plane of the Tevatron ring. The origin is at the center of the detector, which is the nominal interaction point. The pseudorapidity η is defined as $\eta \equiv \ln[\tan(\theta/2)]$, where the polar angle θ is measured from the proton direction. The azimuthal angle ϕ is an angle in $x - y$ plane measured from the positive x -axis toward the positive y -axis. The radius r is the radial distance from the beam in the $x - y$ plane.

3.2.1 Tracking

CDF is equipped with several charged particle tracking systems which are positioned in a 1.5 Tesla magnetic field, provided by a superconducting solenoid coaxial with the beam.

The tracking system is used to provide position, momentum and charge information for charged particles along their helical trajectory. The primary components of the tracking system include the Silicon Vertex Detector (SVX), the Vertex Time Projection Chamber (VTX), and the Central Tracking Chamber (CTC), see Figs. 3.2.

The Silicon Vertex Detectors

Silicon Vertex Detectors [16] are placed very close to the interaction region in particle colliders to provide very high precision tracking information close to the beam collision point. This provides the ability to distinguish *secondary vertices* displaced from the primary vertex, which are indicative of heavy quark decays. The SVX', a radiation-hard version of the SVX that was installed in 1993, is a four layer silicon microstrip vertex detector, which occupies the radial region between 3.0 and 7.9 cm from the beamline and provides precision $r - \phi$ measurement. It consists of two cylindrical barrel modules placed end-to-end with their axes coincident with the beamline. Each barrel is composed of twelve *wedges* and each wedge covers 30 degrees in azimuth. The total coverage along the z direction is 51 cm. Axial microstrips provide precision track reconstruction with a single hit resolution of $13\ \mu\text{m}$ and an impact parameter resolution of $17\ \mu\text{m}$.

The Vertex Time Projection Chamber

The VTX [17] is a gas drift chamber that surrounds the SVX. Its main function is to provide precise tracking information for charged particles in the $r - z$ plane, to determine the location of the primary vertex along z and to distinguish multiple $p\bar{p}$ interactions in the same beam crossing. The VTX provides tracking information up to a radius of 22 cm. The VTX is divided in 28 modules along the z direction. Each module is divided in two by a central grid, creating 15 cm long drift regions. In addition, each module is subdivided into eight azimuthal wedges. The inner section of the VTX has a cavity built into it to contain the SVX. The VTX provides a z -vertex resolution of about 5 cm.

The Central Tracking Chamber

Both the VTX and SVX' are mounted inside a 3.2 m long drift chamber called the central tracking chamber [18]. The radial coverage of the CTC is from 31 to 132 cm. The CTC contains nine cylindrical “superlayers” of wires, five of which are strung parallel to the beamline to provide tracking information in the $r - \phi$ plane, and other four are tilted by $\pm 3\%$ in reference to the beamline, so together with the axial wires they provide tracking information in the $r - z$ plane. The two-track resolution of the CTC is $3.5 \mu\text{m}$ and the spatial resolution is better than $200 \mu\text{m}$ in $r - \phi$ and 6 mm in z .

For our analysis the CTC provides *in-situ* calibration of the response of the calorimeter to low energy particles along with a measurement of jet fragmentation properties. The momentum resolution of the SVX-CTC system is

$$\frac{\delta P_T}{P_T^2} = \sqrt{[(0.0009 P_T)^2 + (0.0066 P_T)^2]}, \quad (3.2)$$

where P_T is measured in GeV/c .

3.2.2 Calorimetry

Calorimeters are one of the important parts of the CDF detector for this analysis. All calorimeters have “tower” geometry, chosen because of the importance of jets in high-energy $p\bar{p}$ collisions. The calorimeters cover 2π in azimuth and $|\eta| < 4.2$, see Fig. 3.3. Each tower has an electromagnetic shower counter in front of a corresponding hadron calorimeter to allow comparisons of electromagnetic and hadronic energy on a tower-by-tower basis. All towers are “projective”, i.e. pointing to the nominal interaction point. The CDF calorimeters (see Table 3.2) are sampling calorimeters, consisting of a sandwich of the dense absorber and light active planes,

allowing to sample only a fraction of the energy deposited by a particle.

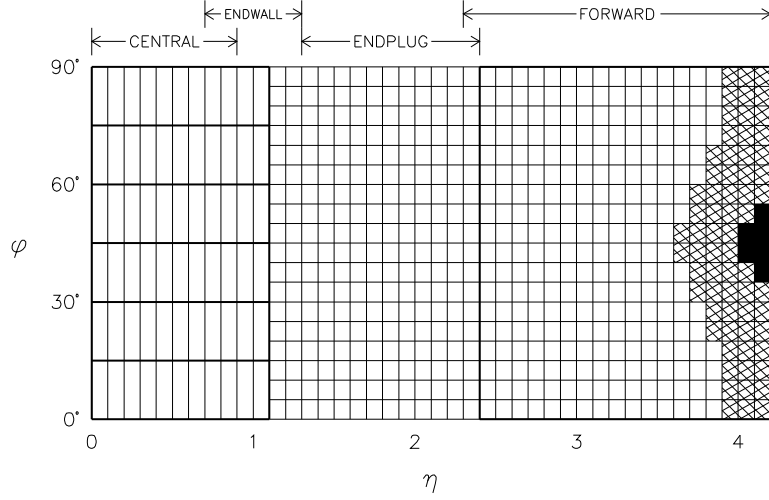


Figure 3.3: Calorimeter Segmentation map in $\eta - \phi$. The shaded area shows regions with only partial coverage for the HAD calorimeters, due to the low-beta quadrupole. The black area has no coverage due to the hole for the beam pipe.

Two types of sampling calorimeters are used at CDF. Scintillator sampling was chosen for the central and endwall calorimeters because of its good energy resolution. In the forward region the energy resolution is not as important, although finer transverse segmentation is required to obtain the same spatial resolution as in the central calorimeter. This was achieved by using gas sampling in the forward and plug calorimeters.

The Central Calorimeters

The Central electromagnetic calorimeter (CEM) [19] covers $|\eta| < 1.1$. The CEM is made up of 48 physically separated modules, called wedges, each covering 15° in ϕ . In the η direction all wedges are divided into 10 towers. The basic layout of a module is shown in Fig. 3.4. The aluminum inner plate, located at 173 cm from the

Table 3.2: The Summary of the CDF Calorimetry.

Calorimeter		η coverage	Energy Resolution	Thickness
Central	EM	$ \eta < 1.1$	$13.7\%/\sqrt{E_T} \oplus 2\%$	$18 X_0$
	Had	$ \eta < 0.9$	$50\%/\sqrt{E_T} \oplus 3\%$	$4.5 \lambda_0$
Endwall	Had	$0.7 < \eta < 1.3$	$75\%/\sqrt{E_T} \oplus 4\%$	$4.5 \lambda_0$
Endplug	EM	$1.1 < \eta < 2.4$	$22\%/\sqrt{E_T} \oplus 2\%$	$18-21 X_0$
	Had	$1.3 < \eta < 2.4$	$106\%/\sqrt{E_T} \oplus 6\%$	$5.7 \lambda_0$
Forward	EM	$2.2 < \eta < 4.2$	$26\%/\sqrt{E_T} \oplus 2\%$	$25 X_0$
	Had	$2.4 < \eta < 4.2$	$137\%/\sqrt{E_T} \oplus 3\%$	$7.7 \lambda_0$

beam line, is used as a base for the CEM calorimeter. The CEM contains 30 layers of 3.2 mm thick lead, interleaved with 31 layers of 5 mm thick plastic scintillator. In order to maintain a constant radiation length thickness as polar angle varies, acrylic is substituted for lead in some layers in some towers.

All towers of each CEM module use the same signal collection method. The light coming from the scintillator is captured by wavelength shifters, which are inserted in the gap between the steel cover plates and scintillator/absorber sandwiches, and transmitted by rectangular lightguides, which run radially out of the calorimeter to photomultiplier tubes. The photomultiplier tubes, which are positioned on both sides of each tower, can also receive light signals from the calibration system.

The CEM modules were initially calibrated with a 50 GeV electron test beam. The electron energy resolution was measured to be $\sigma/E_T = 13.5\%/\sqrt{E_T} \oplus 2\%$ where E_T is the transverse energy of the electrons in GeV and the symbol \oplus indicates that the independent contributions are added in quadrature.

Strip chambers are located near shower maximum, between the fifth and sixth scintillator layers. The chambers determine shower position and transverse

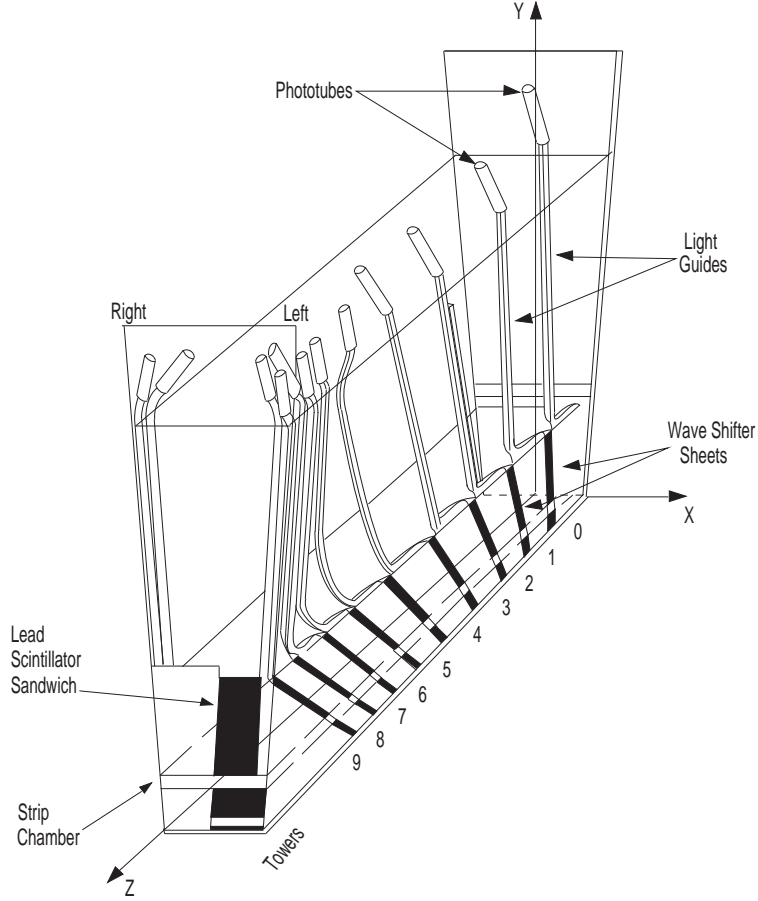


Figure 3.4: Layout of the CEM and CHA light-collection systems. The hadronic section is located directly on top of the electromagnetic section.

shape by measuring the charge deposition on strips and wires.

The CEM calorimeter is followed by the central hadronic calorimeters (CHA and WHA) [19] at larger radius, which covers the range $|\eta_d| < 0.9$ for CHA and $0.7 < |\eta_d| < 1.3$ for WHA. These calorimeters use iron as absorber. The interaction length of both CHA and WHA is $4.5 \lambda_0$. For hadrons the single particle resolution depends on angle and varies from roughly $50\%/\sqrt{E_T} \oplus 3\%$ in the CHA to $75\%/\sqrt{E_T} \oplus 4\%$ in the WHA.

The Plug and Forward Calorimeters

In the forward regions ($1.1 < |\eta_d| < 4.2$) calorimetric coverage is provided by gas proportional chambers [20].

The two Plug Electromagnetic Calorimeters (PEM) cover the regions $1.2 < |\eta_d| < 2.4$. They are cylindrical in shape and are made up of four 90° quadrants. The projective towers cover 5° in ϕ and there are 16 towers segmented in η_d . The first tower, at $|\eta_d| = 2.4$, is of size of 0.09 in units of η_d , the next four towers are only half that size, and the remaining 11 towers have a size of 0.09 again.

The PEM consists of 34 proportional layers sandwiched between lead plates. Each layer has a set of pads and anodes. Ten of the layers have finely grained strips etched into the back of the pad G10 boards for position and shower shape determination.

The Plug Hadronic Calorimeter (PHA) covers the region $1.2 < |\eta_d| < 2.4$. It is arranged in twelve 30° sectors. The towers cover 0.09 units in η_d and 5° in ϕ . The PHA is a sandwich of gas filled proportional tube layers and steel. The construction of proportional layers is similar to the PEM.

The forward electromagnetic (FEM) and hadronic calorimeters (FHA) cover the region from $2.2 < |\eta_d| < 4.2$. The segmentation of these detectors is roughly 0.1 in η and 5° in ϕ . The energy resolution for FEM calibrated with electrons is $\sigma/E_T = 25\%/\sqrt{E_T} \oplus 2\%$. The forward hadronic calorimeter was calibrated with pions and the energy resolution is $\sigma/E_T = 130\%/\sqrt{E_T} \oplus 4\%$.

3.2.3 Muon Detection

The location of the muon subsystems in the outer region of the CDF detector is motivated by the ability of the muon to penetrate matter. The material between the interaction region and the muon detection system, primarily the calorimeters, filters out the majority of electrons and hadrons. There are two separate systems to detect muons at CDF [21].

In the central region, the Central Muon Detector (CMU) covers the region $|\eta_d| < 0.65$ and is located on the outer edge of the central hadronic calorimeter, 3.47 m from the beam axis. There are approximately five interaction lengths of material between the beam axis and CMU detector. The Central Muon Upgrade Chambers (CMUP) were installed in 1992 to reduce false muon background from hadrons that punch through the calorimeter, surround the central region of the CDF detector with 630 tons of additional steel. The CMU and CMUP cover 85% and 80% in ϕ respectively. In the region $0.6 < |\eta_d| < 1.0$ two pairs of free standing conical arches support the central Extension Muon Chambers (CMX). These chambers provide coverage of 67% in ϕ and are located behind the central and wall calorimeters.

In the forward region CDF has a forward muon system (FMU) which covers the region of $2.0 < |\eta_d| < 3.0$ and consists of a pair of magnetized iron toroids. The drift chambers and scintillator counters instrumenting the toroids are used for muon momentum and charge determination.

3.2.4 Triggers

During Run I the Tevatron was operating with six bunches of protons colliding with six bunches of antiprotons. A crossing occurred every $3.5 \mu\text{s}$ in the center of

the CDF detector, corresponding to a rate of 285 kHz, with an estimated 12.5×10^9 proton-antiproton collisions [22]. Each collision is termed an *event* as far as the data and triggering systems are concerned. The rate of data taking is limited basically by two factors: the rate at which events can be written to the tape, about 8 Hz, and the rate at which physicists can analyze the data.

A three-level trigger system has therefore been developed at CDF, where each level examines fewer events in greater detail than the previous level in such a way that only events of particular interest are kept.

A trigger is a collection of physics requirements designed to select specific kinds of events. Event selection criteria for the three trigger levels are described in a trigger table which lists the software modules that are used to make a trigger decision (*the trigger logic path*) and the thresholds for criteria that are used both in the hardware and software in making these decisions (*cuts*).

The lowest level trigger is a hardware trigger, that selects the events at a rate of a few kHz and introduces no dead time. Level 1 makes its decision based on: (1) electromagnetic, hadronic, and total transverse energy, (2) the transverse energy imbalance, (3) stiff tracks in the central tracking chamber, (4) muon candidates in the muon chambers.

The Level 1 trigger uses trigger towers for looking at the calorimetry, with a width of about 15° in azimuth (ϕ) and 0.2 in pseudo-rapidity (η). This corresponds to two physical towers in η and one physical tower in ϕ for the central calorimeter or three physical towers in ϕ for the plug and forward calorimeters. The jet triggers are based on two calorimeter Level-1 triggers that require the presence of a tower with CEM and CHA E_T above thresholds. For the first of these triggers CEM and CHA E_T thresholds are 8 and 12 GeV respectively; for the second, both thresholds are 4

GeV.

The Level 2 trigger processes events selected by the Level 1 trigger. It is more sophisticated and requires $\sim 10 \mu\text{s}$ to make a decision. The Level 2 trigger consists of custom-built hardware and uses the information from the readout electronics. This trigger is responsible for the identification of photons, leptons and jets, and therefore the largest number of events are rejected at this level. The Level 2 distinguishes jet events based on the energy measured in single clusters. If an event deposits an energy of at least 3 GeV in a single electromagnetic or hadron calorimeter tower, the jet clustering algorithm starts. If any of the four neighboring electromagnetic or hadronic towers records more than 1 GeV, it is included in the cluster. This process continues until no more eligible towers are found, after which the energy is summed to determine the total energy of the cluster. There are four jet triggers: Jet_20, Jet_50, Jet_70, and Jet_100, each requiring a minimum energy of 20, 50, 70, and 100 GeV respectively. Since the cross sections for physical processes are usually falling function of E_T , the low-energy triggers are *prescaled*, i.e. only a fraction of these events is accepted.

If Level 2 accepts an event, a signal is sent to the front-end electronics on the detector to digitize the event and for scanners to read out the full event. The fully digitized event is then sent to the Level 3 processing system which runs event reconstruction software consisting of physics algorithms to determine if the event should be accepted or rejected. Most of the execution time is used for the three-dimensional track reconstruction in the CTC. The events which passed this filter are stored on magnetic tape for off-line processing at about 5 Hz output rate.

Chapter 4

The Strong Coupling Constant in Inclusive Jet Production

One of the most important areas of high energy studies consists of testing Quantum Chromodynamics. Since the theory has only one free parameter, the coupling constant α_s , tests of QCD can be quantified in terms of comparison of measurements of α_s in different processes and at different energy scales. A precise measurement of α_s is motivated by a number of considerations [23]:

- QCD with its one parameter α_s , must account for the rich phenomenology that is attributed to the strong interaction, including perturbative and non-perturbative phenomena. The determination of α_s from experimental measurements that probe complementary processes is a fundamental test of QCD.
- The couplings of the electroweak theory, α_{em} and $\sin^2\theta_W$, have been determined with a precision of about 0.1%. In contrast, the strong coupling is presently known only to about 5%. It is necessary to improve the accuracy with which the strong coupling has been measured in order to place it on an equal basis

with respect to the other interactions.

- The QCD β -function determines the evolution of the coupling. Accurate measurements of α_s over a wide range of momenta provide an additional fundamental test of the theory. Tests of the QCD β -function constrain physics beyond the Standard Model, in particular the models with additional colored particles.

Hadronic collisions at the Fermilab Tevatron offer excellent opportunities to study QCD over a broad range of energies ranging from a few GeV up to almost half of the beam energy. The availability of calculations beyond leading order and a better understanding of uncertainties associated with the experiment enabled a measurement of α_s from the inclusive jet cross section at CDF. Before discussing the measurement method we first give a more detailed description of the process in question.

4.1 Jets

As was discussed in Chapter 2, one of the characteristic signatures of QCD is the appearance of *jets* in high energy collisions.

Jets were first observed in 1975 in e^+e^- annihilations at SLAC and later at the PETRA collider [24]. However only at high energy $p\bar{p}$ colliders [25] did jet identification and measurements become relatively unambiguous¹.

The basic goal of jet studies is to perform “precision” measurements of the strong interaction, since jets can be thought of as “footprints” of the partons

¹At lower energies it is difficult to separate jets from the so-called *underlying* hadrons. In addition to that the jet identification method in earlier experiments suffered from “trigger” bias. Events were selected with high-momentum tracks, thereby favoring the appearance of jet-like structures due to momentum balancing. To prevent this, jet triggers should not be biased by event shape features such as the total transverse energy.

participating in hard interactions.

The first question in studying jets is that of jet definition, which is rather ambiguous.

From the theoretical point of view jets are simply manifestations of partons (gluons or quarks) as relatively isolated sprays of energetic hadrons observed in the final states of high energy collisions. In these processes the long-distance contributions (such as hadronization) can be separated out from the hard collision (factorization property) and therefore perturbative techniques are appropriate. The ideal jet definition would allow to associate a unique set of final hadrons with the jet from a single scattered parton. However, this can not be achieved in principle, since quarks and gluons carry color charge and are considered massless in theoretical calculations, whereas jets are colorless and often have large invariant mass.

From the experimental point of view jets are defined as large energy depositions in a localized group of calorimeter cells, see Fig. 4.1. These energy depositions are identified with the help of a clustering algorithm.

To minimize the difference between theoretical predictions and experimental measurements, the Snowmass [26] algorithm was proposed. It is called the *cone* algorithm:

A jet is defined as the set of particles i whose momenta lie within an (η, ϕ) cone of radius R and centered on the jet axis (η_{jet}, ϕ_{jet}) :

$$\sqrt{(\eta_n - \eta_{jet})^2 + (\phi_n - \phi_{jet})^2} < R. \quad (4.1)$$

The jet E_T , pseudorapidity and azimuthal angle are calculated as averages over the particles contained in the jet:

$$E_T^{jet} = \sum_i E_T^i, \quad (4.2)$$

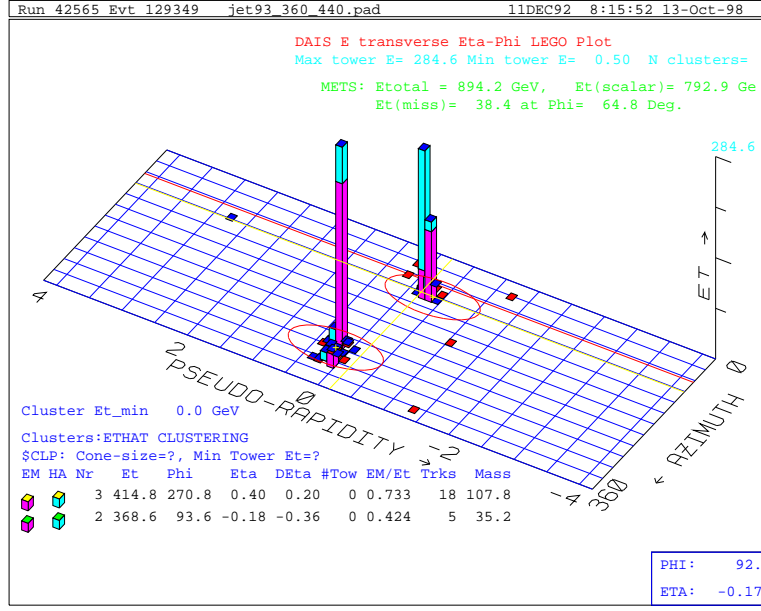


Figure 4.1: Lego display of a jet event from CDF.

$$\eta_{jet} = \frac{\sum_i E_T^i \eta_i}{E_T^{jet}}, \quad (4.3)$$

$$\phi_{jet} = \frac{\sum_i E_T^i \phi_i}{E_T^{jet}}. \quad (4.4)$$

where E_T^i is the transverse energy in the cell. This process of finding the center and then recalculating the cone is iterated until the cone center matches the jet center (η_{jet}, ϕ_{jet}) .

CDF uses a slightly different clustering algorithm, which consists of the following steps:

1. a list of towers with $E_T > 1.0$ GeV is created;
2. preclusters are formed from an unbroken chain of contiguous seed towers with decreasing tower E_T ; if a tower is outside a window of 3x3 towers surrounding the seed, it is used to form a new precluster;
3. the preclusters are grown into clusters by finding the E_T weighted centroid and

collecting the energy from all towers with more than 100 MeV within $R = 0.7$ of the centroid;

4. a new centroid is calculated from the set of towers within the cone and a new cone is drawn around this position;
5. steps 3 and 4 are repeated until the set of towers contributing to the jet remains unchanged;
6. overlapping jets are merged if they share $\geq 75\%$ of the smaller jet's energy; if they share less, the towers in the overlap region are assigned to the nearest jet;
7. the final jet parameters are computed according to following formulae:

$$E^{jet} = \sum_i E^i, \quad (4.5)$$

$$P_x = \sum_i E_i \sin(\theta_i) \cos(\phi_i), \quad (4.6)$$

$$P_y = \sum_i E_i \sin(\theta_i) \sin(\phi_i), \quad (4.7)$$

$$P_z = \sum_i E_i \cos(\theta_i), \quad (4.8)$$

$$\phi_{jet} = \tan^{-1} [P_y/P_x], \quad (4.9)$$

$$\sin \theta_{jet} = \frac{\sqrt{P_x^2 + P_y^2}}{\sqrt{P_x^2 + P_y^2 + P_z^2}}, \quad (4.10)$$

$$E_T^{jet} = E^{jet} \sin \theta_{jet}. \quad (4.11)$$

The principal difference between the CDF and Snowmass algorithms is that CDF jets are not massless.

The Snowmass algorithm has two main problems, the solutions of which introduced the slight differences in the experimental definitions. First, global maximization (i.e. clustering over entire (η, ϕ) space) is very time consuming, that is

why local maximization or “seeds”¹ are used, as in the CDF clustering algorithm. Second, after performing the maximization, several jets can overlap, sharing particles. According to the Snowmass algorithm, two partons will be defined as separate jets only if they are $2R$ apart from each other. The CDF algorithm is more efficient in identifying overlapping jets, even if the distance between them is less than $2R$. Therefore an additional parameter was introduced in the parton clustering algorithm applied in theoretical calculations: two partons have to be separated by more than $R_{sep} \times R$, (where R is the radius of the jet cone and R_{sep} is the new parameter) to be considered as separate jets. This corresponds to 50% efficiency in jet separation, i.e. two jets at $R_{sep} = 1.3$ are merged 50% of the time and identified as individual jets 50% of the time. The value $R_{sep} = 1.3$ gives the best agreement with data.

4.1.1 The Inclusive Jet Cross Section

The inclusive jet cross section represents the probability of observing a hadronic jet with given E_T and rapidity in $p\bar{p}$ collisions. Since jets are produced via scattering of small number of partons, it is a large angle scattering which involves only short distance process (see Section 2.4), where the strong interactions are relatively weak (small α_s), so that perturbative techniques are appropriate. The non-perturbative corrections to the perturbative results are small, because we are dealing with an inclusive process. The term *inclusive process* indicates that all jets are included in the cross section measurement, regardless of the presence of additional objects.

¹The introduction of a precise definition of seed into the theoretical calculation makes the merging/splitting step infrared-unsafe. It was not noticed for a while, since divergences manifested themselves only in calculations of four-parton final states. Exact calculations for two jet cross sections have only reached NLO, corresponding to the three-parton final states.

In theoretical calculations the invariant cross section is expressed as:

$$\frac{Ed^3\sigma}{d^3p} \equiv \frac{d^3\sigma}{dyd^2p_T}, \quad (4.12)$$

where E and p are the jet energy and momentum, and on the right side of the equation the same cross section is expressed in variables that have simple transformation under longitudinal boosts:

$$y = \frac{1}{2} \ln \left(\frac{E + p_z}{E - p_z} \right), \quad (4.13)$$

y is the rapidity and p_T is the transverse momentum of the jet.

In practice the rapidity is often approximated by the pseudorapidity η (see Section 3.2):

$$\eta = -\ln \tan(\theta/2), \quad (4.14)$$

which coincides with rapidity in the massless jet limit $m \rightarrow 0$. It is also standard to use the transverse energy:

$$E_T = E \sin \theta, \quad (4.15)$$

instead of the transverse momentum p_T ; again in the massless jet limit $p_T = E_T$. These substitutions are motivated by convenience, since the angle θ from the beam direction is measured directly in the experiment and E_T is the quantity measured in the calorimeter.

The cross section measured in the experiment is the number of jets N observed in given $\Delta\eta$ and ΔE_T intervals and normalized by the total luminosity \mathcal{L} :

$$\frac{d^2\sigma}{dE_T d\eta} = \frac{N}{\Delta E_T \Delta \eta \mathcal{L}}. \quad (4.16)$$

It is related to Eq. 4.12 by:

$$\frac{Ed^3\sigma}{d^3p} \xrightarrow{m \rightarrow 0} \frac{1}{2\pi E_T} \frac{d^2\sigma}{dE_T d\eta}, \quad (4.17)$$

where the integration over the azimuthal angle ϕ has been performed.

4.1.2 Monte Carlo calculations of jet cross section in hadronic collisions

As discussed before, a particular jet algorithm can affect the number of jets observed in a given event, and as a result the jet cross section will depend on the procedure used to define an experimental jet. However, once the procedure is defined at the experimental level, we will have a precisely determined number of jets for each event.

In theoretical calculations, the jet algorithm plays an important role in determining the minimal transverse energy of a jet, which determines how soft radiation is removed. At the same time, the hadronic information is averaged out by replacing all hadrons within the jet cone by a jet axis and energy. This allows to compare the jet axis and energy from the hadronic shower with the jet axis and energy from the partonic shower, calculated within perturbative QCD (pQCD). Of course, non-perturbative hadronization effects are not predicted by pQCD, and neither are contributions from the *underlying event*. The ideal jet algorithm minimizes these effects and allows a more direct comparison between theory and experiment.

Leading order (LO) matrix elements for $p\bar{p} \rightarrow n \text{ jets}$ are computed for $n \leq 5$ by using special techniques such as color decomposition, recursion relations and helicity amplitudes, to control the increase in the number of Feynman diagrams. The jet cross section is calculated by Monte Carlo integration over the phase space of the final state partons. This method allows for any particular experimental algorithm to be applied. Important fact that one should not miss is that at LO, each jet is modeled by a single parton, to which all jet defining cuts are applied. NLO calculations introduce very important additions to the results: the dependences on the renormalization

and fragmentation scales (μ_R, μ_F) are reduced, we can reconstruct parton shower by combining two partons to form one jet, calculations become more sensitive to the detector limitations. The exact order by order calculation corresponding to NLO has been done for the case of the three-parton final state.

Full NLO matrix elements have been calculated by R.K. Ellis and J. Sexton [30], with the analysis of the inclusive jet cross section available from Ellis, Kunszt, and Soper [28]; and Giele, Glover, and Kosower [29]. The EKS program can generate analytic predictions for jet cross sections as a function of final state parameters. The JETRAD program by Giele, Glover, and Kosower generates weighted events with final state partons. Cross sections are calculated by generating large numbers of events as a function of final state parameters. The two programs agree exactly provided the same input parameters are used.

4.2 α_s from the inclusive jet cross section

One can define a class of inclusive observables X^{QCD} that describe QCD processes and hence are potentially sensitive to α_s . X^{QCD} can be separated into perturbative and non-perturbative contributions:

$$X^{QCD} = X^{pert} + X^{non-pert}. \quad (4.18)$$

The perturbative contribution can in principle be calculated as a power series in α_s , though in practice the large number of Feynman diagrams involved makes calculations beyond the first few orders unmanageable. An observable must be calculated to at least NLO to reduce the dependence on the non-physical fragmentation scale. The solution of the renormalization group equation to the same order can then be used to translate consistently to $\alpha_s(M_Z^2)$. The non-perturbative contribution, often called a

“hadronization correction” in e^+e^- annihilations and $p\bar{p}$ collisions or a “higher twist effect” in lepton-hadron scattering, is expected to have the form of a power-suppressed series, i.e. A/Q^p , where Q is the physical scale of the hard process¹. In general, due to the presence of “renormalon ambiguities” in perturbation theory, the perturbative contribution cannot be calculated without taking into account the non-perturbative power-law contribution. For several inclusive observables the perturbative series has been calculated to NNLO. The power-law corrections cannot in general be calculated. Therefore, in any comparison of a QCD prediction with data, the uncertainties relating to both the uncalculated higher-order perturbative, as well as non-perturbative, contributions should be estimated, and a *theoretical uncertainty* on the extracted value of $\alpha_s(M_Z^2)$ assigned accordingly.

However if we apply this very general method to the inclusive jet cross section at hadron colliders we can see from the discussion at the beginning of this chapter that non-perturbative corrections are small and perturbative calculations at next-to-leading order are available. All this makes it very tempting to try to extract such a fundamental parameter as α_s from the process at hadron colliders. This method was suggested by Walter Giele [1].

The details of the program for the extraction of α_s is as follows.

We can calculate the perturbative expansion of our observable, the inclusive jet cross section, and compare it with the data:

$$X^{pert} = X^{data}. \quad (4.19)$$

¹The *renormalon* or dispersive method is frequently used to estimate non-perturbative corrections by using the connection between divergences of the QCD perturbative series and low-momentum dynamics.

The perturbative expansion can be written as:

$$X^{pert} = \alpha_s^m(\mu_R) \hat{X}^{(0)} K^{(\infty)}(\alpha_s(\mu_R), \mu_R/Q_R), \quad (4.20)$$

where the scale Q_R is the characteristic scale of the observable, in this case the jet transverse energy distribution E_T . The leading order prediction is given by :

$$\alpha_s(\mu_R) \hat{X}^{(0)}, \quad (4.21)$$

and all higher order contributions are included in the K-factor:

$$K^{(n)}(\alpha_s(\mu_R), \mu_R/Q_R) = 1 + \sum_{l=1}^n \alpha_s^l(\mu_R) k_l(\mu_R/Q_R). \quad (4.22)$$

For the inclusive jet cross section $m = 2$ and the K-factor is known up to the NLO, giving $K^{(1)}$. Then

$$X^{pert} = \alpha_s^2(\mu_R) \hat{X}^{(0)} K^{(1)}(\alpha_s(\mu_R), \mu_R/Q_R), \quad (4.23)$$

$$X^{data} = \alpha_s^2(\mu_R) \hat{X}^{(0)} + \alpha_s^3(\mu_R) \hat{X}^{(0)} k_1(\mu_R/Q_R). \quad (4.24)$$

We can define:

$$\sqrt{\frac{X^{data}}{X^{(0)}}} = \alpha_s^{(LO)}. \quad (4.25)$$

Using new definitions we can write the expression for α_s at the n -order as:

$$\alpha_s^{(n)}(\mu_R) = \frac{\alpha_s^{(LO)}}{\sqrt[n]{K^{(n)}(\alpha_s^{(n)}, \mu_R/Q_R)}}, \quad (4.26)$$

So for α_s at next-to-leading order Eq. 4.26 will be substituted by solution of the $m+1$ order polynomial:

$$k_1(\mu_R/Q_R) \left[\alpha_s^{(NLO)}(\mu_R) \right]^{(m+1)} + \left[\alpha_s^{(NLO)}(\mu_R) \right]^m - \left[\alpha_s^{(LO)} \right]^m = 0. \quad (4.27)$$

To extract NLO α_s we use next-to-leading order parton level Monte Carlo JETRAD [29] which is based on the techniques we described above (see Section 4.1.2)

and on the matrix elements of reference [30]. All the experimental jet cuts were applied at the parton level. We calculated the leading order coefficient $X^{(0)}$ and the next-to-leading order coefficient k_1 . JETRAD uses specified parton-distribution functions and associated $\alpha_s(M_Z)$ as input. There is an uncertainty associated with the choice of PDFs which affects the final measurement.

The huge advantage of this method over existing ones is the possibility to measure α_s for different momentum transfers using the same data set. The range of transverse energy distribution is very wide and allows to test the “running” of α_s in addition to extracting measurement at some common energy scale.

Chapter 5

Data

For the measurement of the strong coupling constant we used the inclusive jet cross section measurement from the data from Run 1B of the Tevatron Collider. During 1994-1996 the CDF collaboration collected $\approx 87 \text{ pb}^{-1}$ of data, which were taken at $\sqrt{s} = 1800 \text{ GeV}$. In this chapter we will discuss the data selection criteria and the correction procedures used to obtain the inclusive jet cross section.

5.1 Data Selection

The data for the inclusive jet analysis [38] have been collected using the trigger system described in Section 3.2.4.

The most important trigger requirement for jet analysis was at Level 2, where jet events are identified based on the nearest neighbor clustering algorithm, in which a cluster is defined to be a contiguous group of calorimeter towers with energy above some threshold, surrounded by towers with no energy above threshold¹.

¹In comparison to the cone-algorithm used by the CDF offline analysis, this algorithm uses a seed tower threshold of 3 GeV and a single tower threshold of 1 GeV, the E_T of the calorimeter towers was calculated with the assumption that the interaction occurs at the center of the detector.

There are four jet triggers, requiring a minimum energy of 20, 50, 70 and 100 GeV respectively. The highest E_T clusters came from the two unscaled paths: single cluster of $E_T > 100$ GeV, or a sum of E_T over all clusters > 175 GeV. The jet_20 and jet_50 triggers have the additional requirement that they must satisfy the Level-1 calorimetry triggers described in Section 3.2.4, whereas the jet_70 and jet_100 are required to pass any Level 1 trigger.

Table 5.1 shows the jet E_T thresholds, prescale factors and E_T ranges used in triggers of different levels. The prescale factors are implemented for the purpose of reducing the trigger rate to an acceptable level: only a fraction $\frac{1}{PS}$ of events are allowed to pass the trigger. The effective prescale factors were determined for each of the low E_T samples by calculating the ratio of this sample to the next highest E_T sample in the bins which overlapped. The uncertainties on these effective prescale factors were taken to be half of the difference between the calculated factors and their nominal values.

Level 3 trigger requirements were used to remove backgrounds that produced clusters at Level 2. For Level 3 jets were reconstructed using the standard CDF jet clustering algorithm, which is described in Section 4.1, and has lower E_T requirements (see Table 5.1) than Level 2 triggers, because of the smearing of jet E_T 's, due to the z -vertex mis-assignment.

The so-called *raw* data were required to pass additional clean-up cuts:

- Bad runs and duplicate events
- Total energy detected in the calorimeter < 1800 GeV
- Cosmic ray removal with COSFLT cut
- $E_T/\sqrt{\sum E_T} < 6.0$

Table 5.1: E_T range and prescale factors (PS) for QCD triggers

	Level 2	Level 3	Offline		PS
Trigger	E_T^{min}	E_T^{max}	E_T^{min}	E_T^{max}	L2×L1
Jet_20	20	10	40	75	25×40
Jet_50	50	35	75	100	1×40
Jet_70	70	55	100	130	8×1
Jet_100	100	80	130	440	1×1

- $|z_{vertex}| < 60$ cm
- $0.1 < |\eta_d| < 0.7$

Bad runs and duplicate events cut “Bad” runs are rejected by using the official CDF “good run” list. This list contains the run numbers that are good for general analyses and those good for analyses relying on muon detectors.

Total energy detected in the calorimeter < 1800 GeV cut Since Run 1B had more background events from main ring leftover even after cosmic ray removal and E_T cuts, an additional cleanup cut, requiring the total energy detected in the calorimeter to be less than 1800 GeV, was introduced.

Cosmic ray removal with COSFLT cut Cosmic rays passing through the detector will leave large energy deposits that are unbalanced and could be a significant source of events with large E_T . However, in general these energy deposits will occur out-of-time with a $\bar{p}p$ bunch collision. Any tracks left of these cosmic rays will point to the event vertex too. COSFLT rejects events by examining the out-of-time energy in the hadronic calorimeter. All events with timing outside of the bunch crossing window (-20 ns $< t < 30$ ns, for central wedges, -25 ns $< t < 55$ ns for the endwall calorimeters) and total energy of 6 GeV anywhere

in the CHA or WHA are rejected.

Missing E_T significance cut Missing E_T significance is defined as $\cancel{E}_T/\sqrt{\sum E_T}$, where \cancel{E}_T is the magnitude of the vector sum of the transverse energy in the event and $\sum E_T$ is the total transverse energy. In generic jet events, \cancel{E}_T mainly results from fluctuations during shower propagation in the calorimeter. The effects of undetected neutrinos from semileptonic decays of heavy quarks are small. The cut of $\cancel{E}_T/\sqrt{\sum E_T} < 6.0$ ensures that the \cancel{E}_T requirement is independent of the E_T of the jets.

Z vertex cut The $p\bar{p}$ interactions can occur anywhere in z along the beamline. For each event, the vertex reconstruction is performed using the information provided by the VTX detector. The vertex distribution has a roughly Gaussian shape with 30 cm width and centered within a few cm of $z = 0$. To ensure good coverage of the central detector, each event is required to have a vertex within $|z| < 60$ cm of the center of the detector ($z = 0$) along the beamline.

5.1.1 Trigger Efficiency

Trigger efficiencies are dominated by the Level-2 trigger. To estimate the efficiency of a given Level-2 trigger, we use data collected with the next-lower threshold trigger. For example, to estimate the trigger efficiency of the jet_100 trigger, we look at jet_70 data. The efficiency as a function of jet E_T will be equal to the ratio of the jet E_T spectrum of events from the jet_70 sample that have a Level 2 cluster with $E_T > 100$ GeV to the E_T spectrum of all jet_70 events. This method was used for the jet_100, jet_70 and jet_50 trigger efficiencies. For the jet_20 sample the second highest E_T jet was used to determine the ratio of the second jet E_T spectra for events which

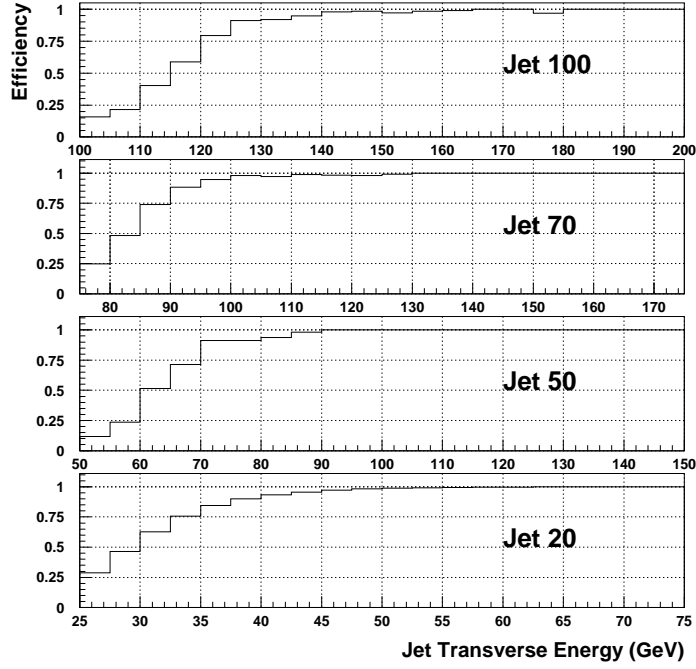


Figure 5.1: The trigger efficiencies for jet_100, jet_70, jet_50, and jet_2- triggers.

had Level 2 $E_T > 20$ GeV to the total second jet E_T spectra. The efficiencies of the triggers as a function of E_T are presented in Fig. 5.1. The uncertainty was estimated using binomial statistics. To select events with high trigger efficiency ($\geq 95\%$) jet E_T thresholds of 130, 100, 75, and 40 GeV were introduced in the offline analysis for jet_100, jet_70, jet_50, and jet_20 samples respectively.

5.2 Jet Corrections

The measured cross section for the E_T bins used in the analysis can be calculated using the following formula:

$$\frac{1}{\Delta\eta} \int d\eta \frac{d\sigma}{dE_T d\eta} = \frac{1}{\Delta\eta} \frac{1}{\mathcal{L}} \frac{N_{jet}}{\Delta E_T}, \quad (5.1)$$

	E_t -bin GeV	$< E_t >$ GeV	number of jets	$d^2\sigma/dE_t d\eta$ nb/GeV	$\delta(d^2\sigma/dE_t d\eta)$ nb/GeV
Jet_20					
1	40-45	42.26	22621	0.469×10^2	0.132×10^1
2	45-50	47.26	12277	0.246×10^2	0.608×10^0
3	50-55	52.27	7083	0.140×10^2	0.324×10^0
4	55-60	57.30	4046	0.794×10^1	0.189×10^0
5	60-65	62.34	2431	0.476×10^1	0.127×10^0
6	65-70	67.33	1655	0.323×10^1	0.969×10^{-1}
7	70-75	72.39	1062	0.207×10^1	0.729×10^{-1}
Jet_50					
8	75-80	77.34	16819	0.142×10^1	0.189×10^{-1}
9	80-85	82.36	11609	0.948×10^0	0.128×10^{-1}
10	85-90	87.36	8330	0.677×10^0	0.916×10^{-2}
11	90-90	92.39	5897	0.478×10^0	0.764×10^{-2}
12	95-100	97.34	4368	0.353×10^0	0.624×10^{-2}
Jet_70					
13	100-105	102.38	15097	0.256×10^0	0.290×10^{-2}
14	105-110	107.38	11151	0.186×10^0	0.228×10^{-2}
15	110-115	112.36	8501	0.141×10^0	0.186×10^{-2}
16	115-120	117.40	6541	0.108×10^0	0.157×10^{-2}
17	120-125	122.35	4980	0.823×10^{-1}	0.132×10^{-2}
18	125-130	127.40	3748	0.618×10^{-1}	0.111×10^{-2}
Jet_100					
19	130-140	134.57	43006	0.435×10^{-1}	0.302×10^{-3}
20	140-150	144.58	25970	0.263×10^{-1}	0.163×10^{-3}
21	150-160	154.61	16486	0.167×10^{-1}	0.130×10^{-3}
22	160-170	164.63	10650	0.108×10^{-1}	0.104×10^{-3}
23	170-180	174.65	7055	0.714×10^{-2}	0.850×10^{-4}
24	180-190	184.64	4804	0.486×10^{-2}	0.701×10^{-4}
25	190-200	194.69	3178	0.321×10^{-2}	0.570×10^{-4}
26	200-220	208.78	3527	0.178×10^{-2}	0.300×10^{-4}
27	220-240	228.79	1746	0.883×10^{-3}	0.211×10^{-4}
28	240-260	248.92	957	0.484×10^{-3}	0.156×10^{-4}
29	260-280	268.92	416	0.210×10^{-3}	0.103×10^{-4}
30	280-300	288.98	202	0.102×10^{-3}	0.719×10^{-5}
31	300-320	309.32	116	0.587×10^{-4}	0.545×10^{-5}
32	320-360	336.10	100	0.253×10^{-4}	0.253×10^{-5}
33	360-440	385.46	31	0.392×10^{-5}	0.704×10^{-6}

Table 5.2: Raw cross section at $\sqrt{s}=1800$ GeV

where N_{jet} is the number of jets in the E_T range of ΔE_T , \mathcal{L} is the luminosity corrected for the prescale factor, and $\Delta\eta$, the pseudorapidity range, for this analysis is equal to 1.2.

However, the measured jet spectrum differs from the spectrum of the *true* jets from the hadron-hadron interactions due to energy mismeasurements and finite energy resolution. We have to make appropriate corrections to be able to compare our results with those from other experiments and with theoretical predictions. At CDF both the corrections for energy mismeasurements and the finite E_T resolution are made simultaneously. The correction procedure is called *unsmearing*. The first step of this program is to produce and parameterize detector *response functions*.

The detector components relevant to the jet analysis are the calorimeters, and therefore the origin of jet mismeasurements can be understood in general after explaining in a few words the basics of calorimetry.

Calorimetry

Neutral and charged particles incident on a block of material deposit their energy through creation and destruction processes. The deposited energy is rendered measurable by ionization or excitation of the atoms of matter in the active medium. The active medium can be the block itself (homogeneous calorimeter) or a set of layers in the sandwich structure of a sampling calorimeter, as in CDF. The measured signal is usually proportional to the incident energy. Calorimeters have the following features:

- They can measure energies of both neutral and charged particles
- The absorption of energy of incident particles is via a cascade process that leads

to a number of secondary particles, n , where n is proportional to the incident energy.

- The development of the cascade is statistical in nature and the uncertainty on the measurement of energy (σ) is governed by the statistical fluctuation on n , thus the relative energy resolution improves with energy as $\sigma/E \propto 1/\sqrt{n} = 1/\sqrt{E}$.
- The cascade develops differently both longitudinally and laterally, for electrons, photons, hadrons, and muons. This difference can be used to determine the identities of the particles.

According to the above, the jet energy resolution is limited by effects from: (a) algorithms used to define jets (energy depends on cone radius, lateral segmentation of cells, etc.); (b) fluctuations in the particle content of jets due to differences in fragmentation from one jet to another; (c) fluctuations in the underlying event; (d) fluctuations in energy pileup¹ in high luminosity hadron colliders. All of the above factors apply to our measurement.

To estimate the calorimeter response to jets we measure both the response to single particles and the number and P_T spectrum of particles within a jet.

The “unsmearing” procedure [31] is applied for the simultaneous correction for detector response and energy resolution.

5.2.1 Response functions

The response of the calorimeter to jets of different *true* E_T is measured and parametrized with the Monte Carlo simulation tuned to the CDF data [34], where

¹The energy equivalent of electronics noise and fluctuations in energy carried by particles other than the ones of interest, entering the measurement area, is labeled *pileup*.

we define E_T^{true} as the E_T of all particles in a cone with radius $R = 0.7$ around the jet axis. We will call $E_T^{smeared}$ the E_T of the jet after the detector simulation. The distribution of $E_T^{smeared}$ will be fitted with a function of four parameters (mean, sigma, and two tails) for a given E_T^{true} . These functions are called the *response functions*. The response functions represent the probability that a true jet with transverse energy E_T^{true} will be measured as a jet with transverse energy $E_T^{smeared}$.

Fragmentation

A major factor involved in the jet energy correction and jet resolution is the non-linearity in the response of the detector to charged particles. Therefore the Monte Carlo program was tuned to reproduce the P_T spectrum of charged particles in jets (fragmentation functions). The simulation was performed using the following path:

- SIMJET Monte Carlo routine generated jets. It created two partons in a spectrum defined to match the spectrum measured in the inclusive jet cross section.
- The ISAJET (SETPRT) routine was used for fragmenting the jets. Since fragmentation is a non-perturbative process, different phenomenological models are used for its description. SETPRT is based on the Feynman-Field fragmentation model, which allows easy tracking of the particles to the originating partons. The jet fragmentation functions can be tuned to reproduce the data.
- The detector response is simulated with the QFL program, which is based on a parametrization of the detector response to single particles instead of the direct simulation of the energy loss of particles traveling through the active media of the detector. The simulation included calorimeter non-linearity, cracks and less

sensitive regions, etc. The response of the detector to single particles was tuned with test beam data ($10 < E_{beam} < 227$ GeV) and *in-situ* calibration data using CTC tracking information for single hadrons with momentum ranging from 400 MeV/ c to 10 GeV/ c .

The main reason for tuning the fragmentation functions is to account for the non-linearity of the calorimeter. The fragmentation uncertainty, which can be treated as Gaussian, is mostly due to the lack of knowledge of the track reconstruction efficiencies.

Charged Pion Response

The response of the calorimeter to charged pions can be studied in two ways depending on the momentum of the particle. For high momenta $P_T > 15$ GeV/ c the calibration of the calorimeter was measured by using test-beam data. The main contribution comes from the uncertainty of the test-beam momentum. Additional contributions include the disagreement in the ϕ -crack response (face of the tower) and variations in tower-to tower responses. For low- P_T pions the detector calibration was done by choosing isolated tracks and extrapolating them to the calorimeter, and comparing the P_T of the track to the deposited energy in the calorimeter. Since charged pions are accompanied by neutral pions, the latter contribution should be subtracted. The neutral pion background is the main source of uncertainty here.

Neutral Pion Response

The uncertainty in calorimeter response to electrons and photons is due to the uncertainty in the EM calorimeter response (EM has good resolution and is linear and thus does not contribute significantly to the jet energy scale uncertainty).

Underlying Event Correction

The underlying event energy is the energy from the fragmentation of partons *not associated* with the hard scattering, and is not completely defined theoretically. The method used to estimate the underlying event energy in the jet cone is based on the *Minimum Bias* data sample (events triggered by the presence of hits in the detector in front and in back of the collision region). A cone of radius of 0.7 was randomly placed in the central detector and the energy in the cone was measured as a function of the number of found vertices. By combining the energy measured in the cone in the minimum bias data and the number of interactions in the jet data, the average correction was derived to be equal to 2.2 GeV¹. Despite the possibility to make a precise measurement, at the level of a few percent, of the average energy deposited in random cones, the uncertainty in the definition of the underlying event forces us to assign a rather large 30% uncertainty on the underlying event energy.

The underlying event correction is applied as a shift to the mean of the jet response functions. The tails of the response functions are scaled appropriately.

Another physics effect which could be considered in jet corrections is the *out-of-cone* energy. Some particles which are produced by fragmentation of a parton fall outside of the cluster cone and are therefore missed. Since the out-of-cone energy is process dependent, usually it is accounted for in the theoretical predictions for the process. In this analysis no corrections are made for *out-of-cone* particles.

¹An alternative method to estimate underlying event energy is based on a comparison of the energies deposited in cones $\pm 90^\circ$ in ϕ from the jet axis. Separate averages of the maximum and minimum energies of 90° cones were calculated. The quantity $E_T^{min-cone}$ was independent of the jet E_T and believed to represent the underlying event energy. The estimate of the UE energy with this method gave 2.2 ± 0.1 GeV.

Energy Scale Stability

The calorimeter response to particles can change with time. During studies of calorimeter response to muons and low energy isolated charged particles, it was determined that the absolute calibration was stable and the associated uncertainty is $\pm 1\%$ since the 1988/89 run.

5.3 The Unsmearing and Corrected Cross Section

Using the response functions (see Fig. 5.2), we can now determine the true spectrum from the measured distribution. We parametrize the true inclusive jet

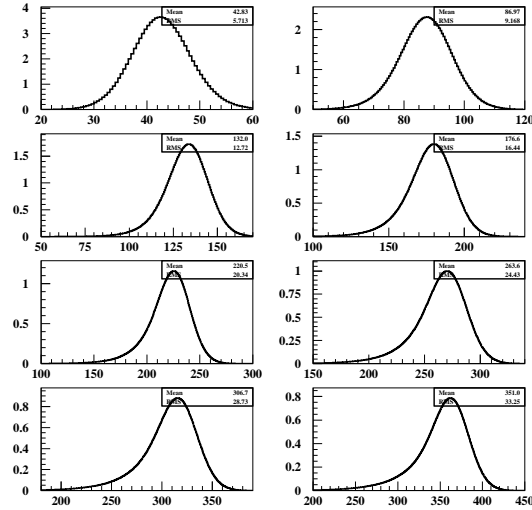


Figure 5.2: The response functions for different E_T^{true} jets.

spectrum with the following function:

$$\frac{d\sigma(E_T^{true})}{dE_T^{true}} = P_0 \times (1 - x_T)^{P_6} \times 10^{F(E_T^{true})}, \quad (5.2)$$

P_0	P_1	P_2	P_3	P_4	P_5	P_6
0.14946E+07	-2.9228	4.4881	-4.9447	1.7891	-0.2297	5.6147

Table 5.3: The parameters of the “standard curve”.

where $F(x) = \sum_{i=1}^5 P_i \times [\log(x)]^i$, $P_0 \dots P_6$ are fit parameters and x_T is defined as $2E_T^{true}/\sqrt{s}$. The smeared cross section in a bin is the convolution of the *true* cross section and detector response functions:

$$\sigma^{smeared}(bin) = \int_L^U dE_T \int_5^{600} dE_T^{true} \left\{ \frac{d\sigma(E_T^{true})}{dE_T^{true}} \right\} Response(E_T^{true}, E_T), \quad (5.3)$$

where U,L are the upper and lower measured E_T values of the bin. The smeared cross section should be compared with the measured cross section.

The corrections to the measured cross section come from the correspondence of the true and smeared spectra for each bin. After an iterative procedure of fitting the smeared spectrum $\sigma^{smeared}$ to the measured cross section, the parameters of the true spectrum are obtained, see Table 5.3. These parameters correspond to the minimum χ^2 , where

$$\chi^2 = \sum ((\sigma^{smeared} - \sigma^{measured})/\delta\sigma^{measured})^2, \quad (5.4)$$

The χ^2 minimization was performed with the MINUIT package [35]. The function $d\sigma/dE_T^{true}$ with these optimized parameters is referred to as the *standard curve*.

After obtaining the true spectrum we can make bin-by-bin corrections to the raw cross section. The $\langle E_T^{corrected} \rangle$ for a bin is defined as:

$$\langle E_T^{true} \rangle \times \frac{\langle E_T^{measured} \rangle}{\langle E_T^{smeared} \rangle}. \quad (5.5)$$

The corrected cross section is correspondingly equal to:

$$\sigma^{true}(E_T^{corrected}) \times \frac{\sigma^{measured}(bin)}{\sigma^{smeared}(bin)}. \quad (5.6)$$

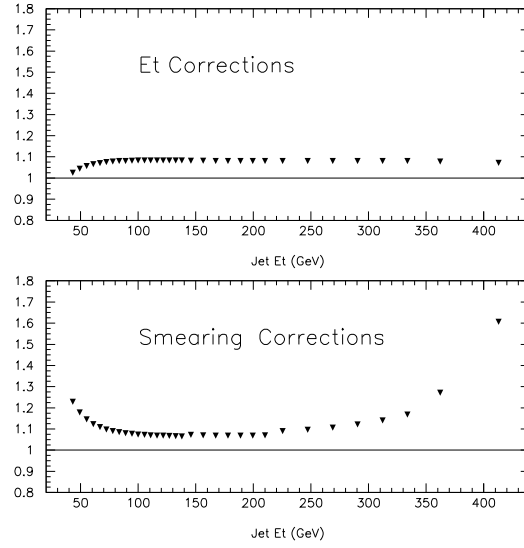


Figure 5.3: The ratios of corrected E_T and corrected cross section to the measured E_T and measured cross section.

The correction factors for the cross section and E_T , which are correlated, are plotted in Fig.5.3.

The corrected inclusive jet cross section from Run 1B is shown in Fig. 5.4 and tabulated in Table 5.4. The uncertainties on the data bins are the quadrature sum of the trigger efficiencies, the uncertainty on the prescale factors and the statistical errors from the number of events in each bin, which are uncorrelated bin-to-bin.

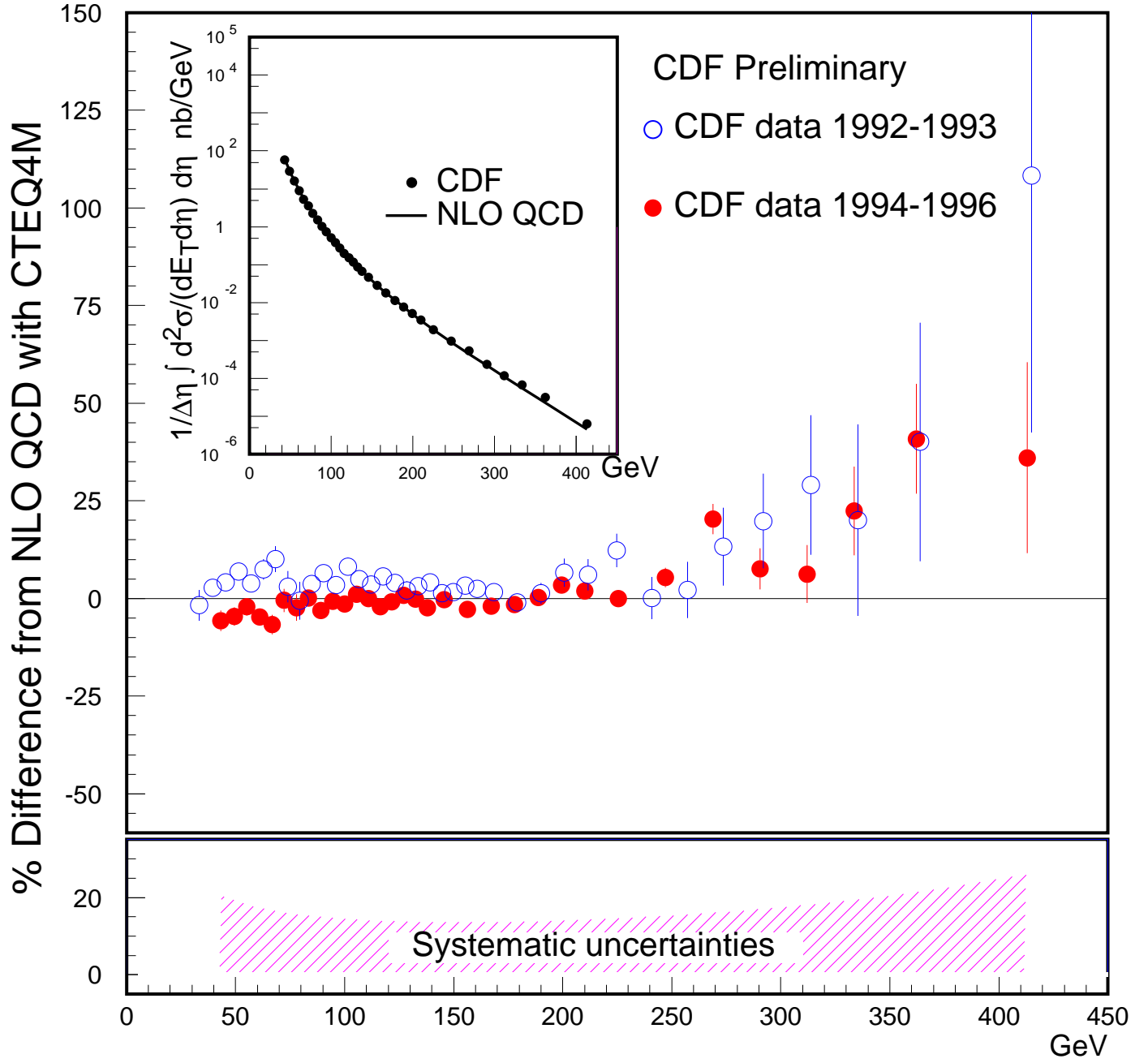


Figure 5.4: Corrected inclusive jet cross section

Table 5.4: CDF corrected inclusive jet cross section from run 1B

Bin	E_T		cross section(σ)	
	$< measured >$	$< corrected >$	$< measured >$	$< corrected >$
1	42.3	43.3	0.469×10^2	$(0.576 \pm 0.016) \times 10^2$
2	47.3	49.3	0.246×10^2	$(0.290 \pm 0.007) \times 10^2$
3	52.3	55.2	0.140×10^2	$(0.160 \pm 0.003) \times 10^2$
4	57.3	61.0	0.794×10^1	$(0.893 \pm 0.021) \times 10^1$
5	62.3	66.7	0.476×10^1	$(0.528 \pm 0.014) \times 10^1$
6	67.3	72.3	0.323×10^1	$(0.355 \pm 0.011) \times 10^1$
7	72.4	77.9	0.207×10^1	$(0.226 \pm 0.008) \times 10^1$
8	77.3	83.5	0.142×10^1	$(0.154 \pm 0.002) \times 10^1$
9	82.4	89.0	0.948×10^0	$(0.102 \pm 0.001) \times 10^1$
10	87.4	94.5	0.677×10^0	$(0.729 \pm 0.010) \times 10^0$
11	92.4	100.0	0.478×10^0	$(0.513 \pm 0.008) \times 10^0$
12	97.3	105.5	0.353×10^0	$(0.378 \pm 0.007) \times 10^0$
13	102.4	110.9	0.256×10^0	$(0.274 \pm 0.003) \times 10^0$
14	107.4	116.3	0.186×10^0	$(0.199 \pm 0.002) \times 10^0$
15	112.4	121.7	0.141×10^0	$(0.151 \pm 0.002) \times 10^0$
16	117.4	127.1	0.108×10^0	$(0.116 \pm 0.002) \times 10^0$
17	122.3	132.5	0.823×10^{-1}	$(0.877 \pm 0.014) \times 10^{-1}$
18	127.4	137.9	0.618×10^{-1}	$(0.659 \pm 0.012) \times 10^{-1}$
19	134.6	145.7	0.435×10^{-1}	$(0.466 \pm 0.003) \times 10^{-1}$
20	144.6	156.4	0.263×10^{-1}	$(0.281 \pm 0.002) \times 10^{-1}$
21	154.6	167.2	0.167×10^{-1}	$(0.178 \pm 0.001) \times 10^{-1}$
22	164.6	177.9	0.108×10^{-1}	$(0.115 \pm 0.001) \times 10^{-1}$
23	174.7	188.7	0.714×10^{-2}	$(0.763 \pm 0.009) \times 10^{-2}$
24	184.6	199.5	0.486×10^{-2}	$(0.520 \pm 0.008) \times 10^{-2}$
25	194.7	210.2	0.321×10^{-2}	$(0.344 \pm 0.006) \times 10^{-2}$
26	208.8	225.4	0.178×10^{-2}	$(0.195 \pm 0.003) \times 10^{-2}$
27	228.8	247.1	0.883×10^{-3}	$(0.968 \pm 0.023) \times 10^{-3}$
28	248.9	268.8	0.484×10^{-3}	$(0.535 \pm 0.017) \times 10^{-3}$
29	268.9	290.5	0.210×10^{-3}	$(0.236 \pm 0.012) \times 10^{-3}$
30	289.0	312.1	0.102×10^{-3}	$(0.117 \pm 0.008) \times 10^{-3}$
31	309.3	333.6	0.587×10^{-4}	$(0.685 \pm 0.064) \times 10^{-4}$
32	336.1	362.2	0.253×10^{-4}	$(0.322 \pm 0.032) \times 10^{-4}$
33	385.5	412.9	0.392×10^{-5}	$(0.630 \pm 0.113) \times 10^{-5}$

Chapter 6

Measurement of α_s

In this chapter we will present the results of the strong coupling constant extraction from the CDF Run1B inclusive jet cross section. The “running” behavior of the coupling constant is demonstrated and the values of $\alpha_s(E_T)$ are evolved to a common scale, the mass of the Z boson. The averaged value of $\alpha_s(M_Z)$ from our measurement is $\alpha_s(M_Z) = 0.1129 \pm 0.0001(\text{exp.stat})$. The comparison of our results with theoretical predictions is discussed at the end of the chapter.

6.1 Measurement of α_s from the inclusive jet cross section

One of the advantages of using $\bar{p}p$ collisions is the possibility to measure α_s over a very broad interval of momentum transfer Q^2 . The CDF inclusive jet E_T spectrum extends to approximately 500 GeV, providing sensitivity to α_s over a range in momentum transfer extending from 50 GeV to values nearly equivalent to that proposed for the next generation of electron-positron and electron-proton colliders.

The agreement between QCD next-to-leading order predictions of the inclusive jet cross section and the data allows us to fit the CDF data with the theoretical curves, and determine the evolution of α_s from this fitting procedure.

For each data point from the inclusive jet cross section we will obtain an α_s value at a corresponding momentum transfer scale. By only using the inclusive jet cross section we will be able to observe the running of the coupling constant with Q^2 .

As discussed in Section 4.2, the basic scheme for α_s extraction can be summarized as following:

$$k_1(\mu_R/Q_R) \left[\alpha_s^{(1)}(\mu_R) \right]^3 + \left[\alpha_s^{(1)}(\mu_R) \right]^2 - \left[\alpha_s^{(0)} \right]^2 = 0.$$

where

$$\alpha_s^{(0)} = \sqrt{\frac{\frac{d\sigma}{dE_T d\eta}}{X^{(0)}}}$$

where $(d\sigma)/(dE_T d\eta)$ is the experimental data corresponding to the inclusive jet cross section, the $X^{(0)}$ and k_1 are coefficients calculated with the NLO JETRAD Monte Carlo program, adapted to the extraction of α_s . The coefficient $X^{(0)}$ corresponds to calculations at leading order and the coefficient k_1 corresponds to next-to-leading order contributions. The input parameters to the program are the values of the factorization and renormalization scales μ_R and μ_F , the minimal and maximal E_T ranges for the jets, as well as the η intervals. JETRAD allows to make calculations with different recombination schemes, like those used by the CDF or D0 experiments. The sizes of the cone radius and parameter R_{sep} also can be changed. The JETRAD program uses parton distribution functions (PDF) obtained from the global fitting procedure with the associated $\alpha_s(M_Z)$ as input parameter. We assume the PDFs to be correct in order to extract α_s .

Let's assume as input PDF set the CTEQ4M parton distributions, which

correspond to the global fit of the world data including the Tevatron jet data and the latest high-precision HERA measurements. The associated $\alpha_s(M_Z)$ is equal to 0.116.

Since it is desirable to have renormalization and factorization scales of the order of the characteristic scale of the process, μ should be comparable with the jet transverse energy E_T . Different choices are possible:

- $\mu = \mu_R = \mu_F$ is equal to the sum E_T of all jets in a given event;
- Original JETRAD choice: $\mu_R = \mu_F = E_T^{max}/2$, where E_T^{max} is the E_T of the leading jet in a given event;
- $\mu_R = \mu_F = E_T^{jet}/2$, the program calculates the cross section at a particular jet E_T , integrating over all configurations that contribute the given E_T .

We will use the third choice. The difference between the cross section calculated according to the last two choices is shown in Fig. 6.1. For convenience we choose the

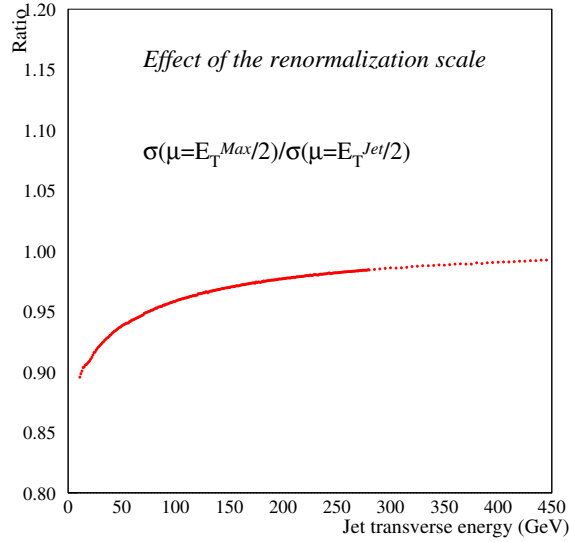


Figure 6.1: Effects of different renormalization scales on the inclusive jet cross section.

factorization scale μ_F to be equal to the renormalization scheme μ_R , which is equal to the $E_T/2$, where E_T is the jet transverse energy. The CDF Run1B inclusive jet

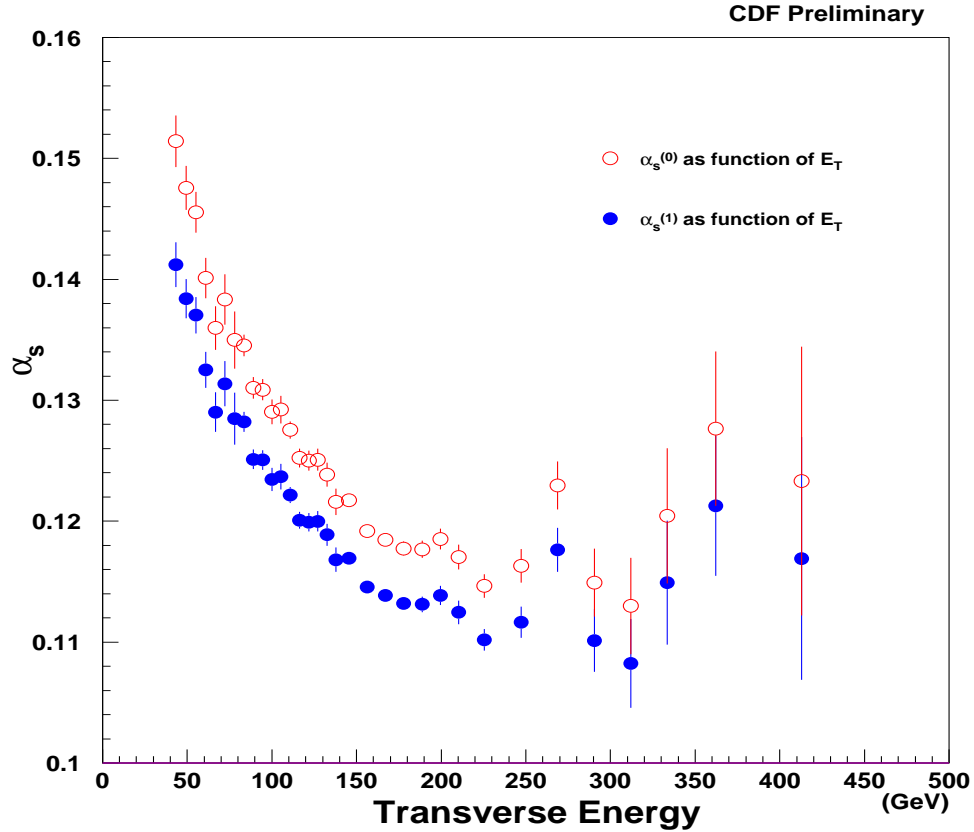


Figure 6.2: Measurement of $\alpha_s(E_T)$.

spectrum has 33 data points (bins), which will correspond to 33 measurements of $\alpha_s(E_T)$, see Fig. 6.2. The values of E_T and the corresponding coupling constants are presented in Table 6.2.

6.2 Measurement of $\alpha_s(M_Z)$

The next step is to determine the strong coupling constant at some common scale for comparison with other experimental results.

We will use the second order of the renormalization group equation solution:

$$\alpha_s(M) = \frac{\alpha_s(\mu_R)}{1 - \alpha_s(\mu_R)L^{(2)}(\mu_R^2/M^2)}, \quad (6.1)$$

where

$$L^{(1)} = b_0 t \quad (6.2)$$

$$L^{(2)} = (b_0 + b_1 \alpha_s(M))t \quad (6.3)$$

$$L^{(3)} = (b_0 + b_1 \alpha_s(M) + b_2^{\overline{MS}} \alpha_s^2(M))t - \frac{b_0 b_1}{2} \alpha_s^2(M) t^2. \quad (6.4)$$

The first coefficients of the β -function are given by [36] are:

$$b_0 = \frac{11N_c - 2n_f}{6\pi} \quad (6.5)$$

$$b_1 = \frac{34N_c^2 - 13N_c n_f + 3n_f/N_c}{24\pi^2} \quad (6.6)$$

$$b_2^{\overline{MS}} = \frac{5741N_c^3 - 3391N_c^2 n_f + 224N_c n_f^2 + 507n_f + 54n_f/N_c - 66n_f^2/N_c}{3456\pi^3}, \quad (6.7)$$

where N_c is the number of colors and is equal to 3. Although b_0 and b_1 are independent of the renormalization scheme, b_2 is renormalization scheme dependent and in this case was calculated in the \overline{MS} scheme. n_f is the number of *active* flavors. This concept is explained in more detail below.

Effect of the heavy quark masses

Let us consider a theory in which there are just two quarks of very different mass, a light quark a of mass m and a heavy quark A of mass M , with $M \gg m$. It

Table 6.1: Number of active flavors at different scales

Scale Q	number of active flavors
$1 < Q < 3 \text{ GeV}$	3
$3 \text{ GeV} < Q < 10 \text{ GeV}$	4
$10 \text{ GeV} < Q < m_t$	5
$m_t < Q$	6

is conventional to treat a light quark as massless when studying physics at “large” momentum scales, which means that we can neglect m when $Q \gg m$. If we deal with really large momentum scales where $Q \gg M$ then we can neglect both m and M and can effectively use “massless” theory with two massless quarks. But the most interesting region is in between, where $m \ll Q \ll M$. Intuitively we will assume that A can not play any role at scales $Q \ll M$ and we should ignore A completely. While true in QCD, this statement is not trivial to prove with regard to renormalization and forms the basis of the *decoupling* theorem [37]. As a consequence of the decoupling theorem we can understand how to treat quarks with non-negligible mass parameters. Let q_1, q_2, \dots, q_N be a sequence of quarks with masses $m_1 < m_2 < \dots < m_N$ and suppose that $m_j \ll m_{j+1}$. Then for momentum scales Q in the range

$$m_j \ll Q \ll m_{j+1}$$

the β -function should be calculated as if the theory contains only j massless quarks, and j is defined to be the number n_f of *active* quark flavors. When Q is close to a particular quark mass, then the mass of that quark has to be taken into account explicitly in the calculations. In Table 6.1 we show realistic QCD approximations. However the question remains of how to relate values of α_s measured in two regions $Q \ll m$ and $Q \gg m$. It is achieved by requiring $\alpha_s(\mu)$ to be continuous at different μ scales despite a step-function change in the β -function. The simplest prescription

would be to require this continuity at the scale $Q = m$, the heavy quark mass. With the β -function at leading order:

$$\frac{1}{\alpha_s^+(Q^2)} - b_0^+ \ln \frac{Q^2}{m^2} = \frac{1}{\alpha_s^-(Q^2)} - b_0^- \ln \frac{Q^2}{m^2} = \frac{1}{\alpha_s(m^2)}, \quad (6.8)$$

where

$$b_0^- - b_0^+ = \frac{1}{6\pi}, \quad (6.9)$$

and hence

$$\alpha_s^+(Q^2) = \alpha_s^-(Q^2) \left[1 - \frac{1}{6\pi} \alpha_s^-(Q^2) \ln \frac{Q^2}{m^2} \right]^{-1}. \quad (6.10)$$

Since our measurement covers a region of almost 500 GeV, this is an important aspect to take into account.

The average value of $\alpha_s(M_Z)$

The mass of the Z boson is used as common scale for comparison of α_s between different experiments and different momentum transfers. The advantage of using M_Z is that it is measured with very high precision at CERN, safely in the perturbative region $\alpha_s(M_Z) \ll 1$, and far from the quark mass thresholds, $m_b \ll M_Z \ll m_t$.

By evolving $\alpha_s(E_T)$ for all 33 bins, we obtain 33 independent measurements of $\alpha_s(M_Z)$. As can be seen Fig. 6.4 the extracted values are almost independent of E_T . The values of $\alpha_s(E_T)$ and corresponding $\alpha_s(M_Z)$ with their statistical uncertainties are listed in Table 6.2. By assuming that the next-to-leading order is sufficient to describe the data and by using the fact that $\alpha_s(M_Z)$ is independent of E_T i.e.

$$\frac{\partial \alpha_s(M_Z, \mu_R = E_T)}{\partial E_T} = 0, \quad (6.11)$$

we perform an error-weighted average of $\alpha_s(M_Z)$:

$$\alpha_s(M_Z) = \frac{1}{w} \sum_{i=1}^{N_{bins}} w_i \alpha_s(M_Z, \mu_R = E_T), \quad (6.12)$$

where

$$\frac{1}{w_i} = \Delta\alpha_s^{stat}(M_Z, \mu_R = E_T^i), \quad (6.13)$$

$$w = \sum_{i=1}^{N_{bins}} w_i \quad (6.14)$$

$\Delta\alpha_s^{stat}$ is the statistical uncertainty on the measurement, and N_{bins} is the number of bins. For the calculation of the average value we took into account only the bins with $E_T < 250$ GeV to avoid the bias associated with high E_T jets and the observed excess in the cross-section compared to the theoretical predictions. Even if the high- E_T bins were included the error-weighted average would not be that different due to the large statistical uncertainties in these bins.

The resulting value for $\alpha_s(M_Z)$ with CTEQ4M as input PDF for **JETRAD** is:

$$\alpha_s(M_Z) = 0.1129 \pm 0.0001. \quad (6.15)$$

The small statistical error of this measurement is explained by tens of thousands of jets at medium E_T .

6.3 Comparison of Results with QCD

We can compare our results for $\alpha_s(E_T)$ with the running of the coupling constant predicted by theory. For the theory we will use the solution to the RGE with $\alpha_s(M_Z)$ set equal to the average $\alpha_s(M_Z)$ obtained from our measurement (Eq. 6.12). Since our measurement of the strong coupling constant used parton distribution functions, in this case CTEQ4M with associated α_s obtained from the global

Bin	E_T	Strong Coupling Constant			
		$\alpha_s(E_T)$	error	$\alpha_s(M_Z)$	error
1	43.3	0.1412	0.0019	0.1119	0.0012
2	49.3	0.1384	0.0016	0.1122	0.0010
3	55.2	0.1370	0.0015	0.1132	0.0010
4	61.0	0.1325	0.0015	0.1117	0.0011
5	66.7	0.1290	0.0016	0.1106	0.0012
6	72.4	0.1314	0.0019	0.1136	0.0014
7	77.9	0.1285	0.0022	0.1127	0.0016
8	83.5	0.1282	0.0008	0.1136	0.0006
9	89.0	0.1251	0.0008	0.1122	0.0006
10	94.5	0.1250	0.0008	0.1131	0.0007
11	100.0	0.1235	0.0009	0.1127	0.0008
12	105.5	0.1237	0.0010	0.1138	0.0009
13	110.9	0.1222	0.0007	0.1133	0.0006
14	116.3	0.1201	0.0007	0.1123	0.0006
15	121.7	0.1199	0.0008	0.1129	0.0007
16	127.1	0.1200	0.0008	0.1137	0.0007
17	132.5	0.1189	0.0009	0.1134	0.0008
18	137.9	0.1168	0.0010	0.1121	0.0009
19	145.7	0.1169	0.0004	0.1131	0.0004
20	156.4	0.1146	0.0003	0.1121	0.0003
21	167.2	0.1139	0.0004	0.1125	0.0004
22	177.9	0.1132	0.0005	0.1128	0.0005
23	188.7	0.1131	0.0006	0.1137	0.0007
24	199.5	0.1139	0.0008	0.1154	0.0008
25	210.2	0.1125	0.0010	0.1148	0.0010
26	225.4	0.1102	0.0009	0.1136	0.0010
27	247.1	0.1116	0.0013	0.1167	0.0014
28	268.8	0.1176	0.0018	0.1249	0.0021
29	290.5	0.1101	0.0026	0.1178	0.0030
30	312.1	0.1082	0.0037	0.1169	0.0043
31	333.6	0.1149	0.0051	0.1261	0.0062
32	362.2	0.1213	0.0058	0.1342	0.0072
33	412.9	0.1169	0.0100	0.1319	0.0127

Table 6.2: The extracted $\alpha_s(E_T)$ and corresponding $\alpha_s(M_Z)$ values with associated statistical uncertainties.

fit, it is important to note that all our conclusions will make sense only if the “input” α_s is consistent with the “output” α_s .

The measured value of $\alpha_s(M_Z)$ is:

$$\alpha_s(M_Z) = 0.1129 \pm 0.0001(stat.)^{+0.0078}_{-0.0089}(exp.syst), \quad (6.16)$$

where the last numbers correspond to the experimental systematic errors which will be discussed in the next chapter. As we can see the measured and CTEQ4M values are consistent within errors:

$$\alpha_s^{CTEQ4M} = 0.116. \quad (6.17)$$

Fig. 6.3 shows excellent agreement between the QCD predictions for the running coupling constant and our results derived from the inclusive jet cross section at CDF. The behavior of α_s at high E_T is the direct reflection of the excess at these energies in the inclusive jet cross section.

We can also test whether $\alpha_s(M_Z)$ is independent of the energy scale at which scattering takes place. To do this we will allow for:

$$\frac{\partial \alpha_s(M_Z, \mu_R = E_T)}{\partial E_T} = constant. \quad (6.18)$$

If the *constant* is zero within errors then QCD is correct. We tried to fit the data points with a linear function of E_T :

$$\alpha_s(M_Z, \mu_R = E_T/2) = P_1 + P_2 * (\frac{E_T}{E_T^0} - 1). \quad (6.19)$$

The $min \chi^2 = 1.77$ was obtained for $E_T^0 = 104$ GeV and corresponds to the coefficients:

<i>parameter</i>	<i>=</i>	<i>value</i>	\pm	<i>error</i>
P_1	$=$	0.1125	\pm	0.0003
P_2	$=$	0.2838×10^{-3}	\pm	0.2474×10^{-3}

As we can see (Fig. 6.4) the fit shows independence of $\alpha_s(M_Z, \mu_R = E_T/2)$ with respect to the μ scale without assuming the correctness of the underlying theory.

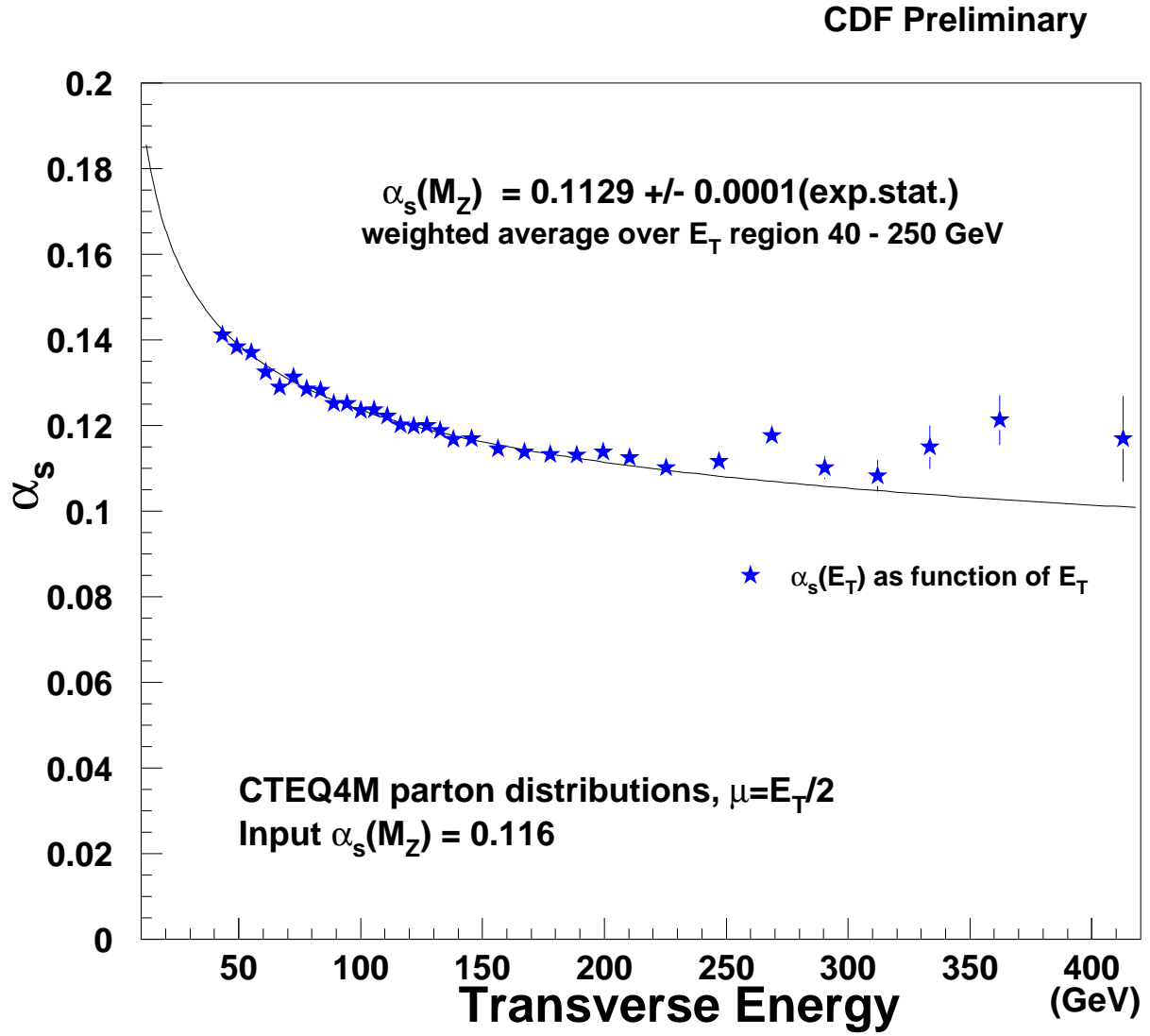


Figure 6.3: Comparison of the “running” of the strong coupling constant with theoretical predictions.

CDF Preliminary

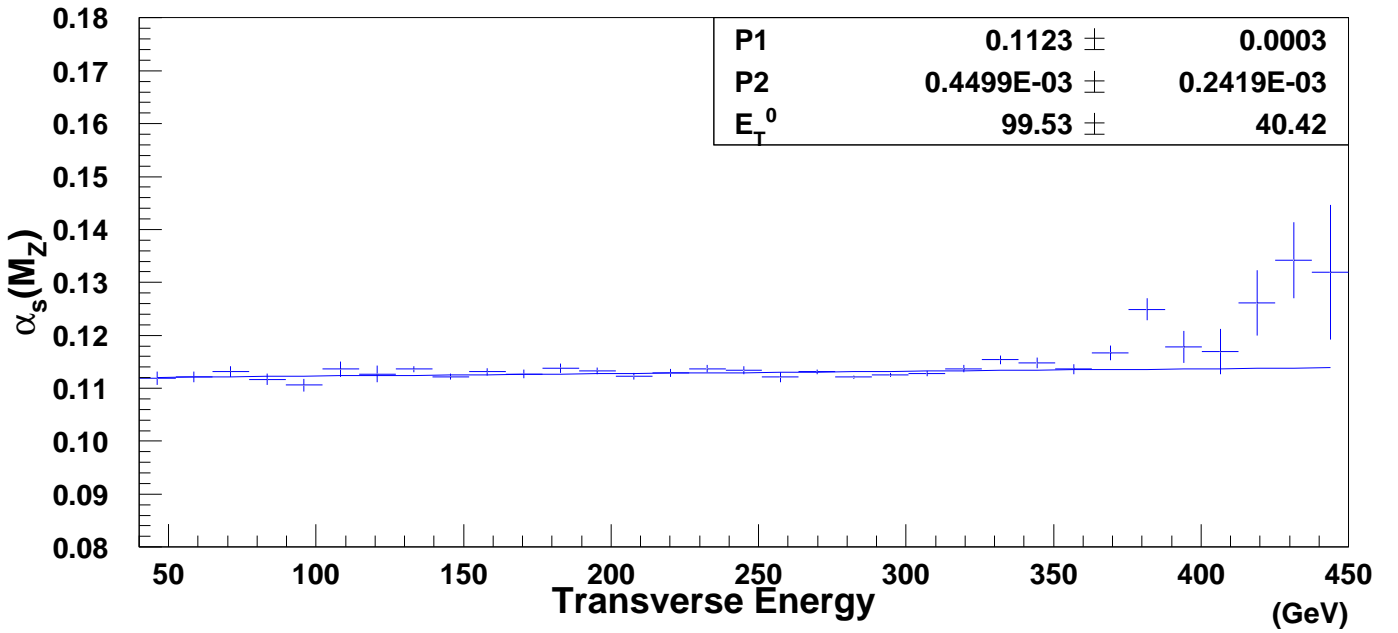
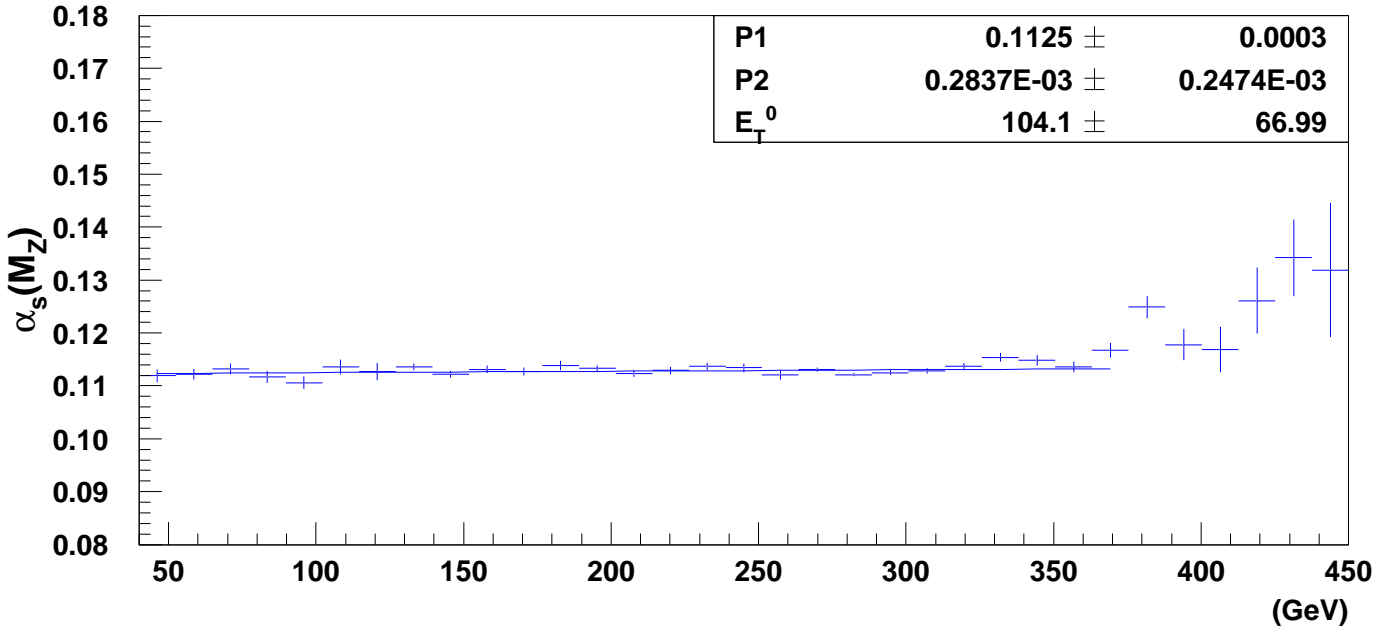


Figure 6.4: Fit of $\alpha_s(M_Z)$ as a function of E_T with a linear function for (top) $E_T < 250$ GeV, (bottom) for all E_T spectrum.

Chapter 7

Systematic Uncertainties

In this chapter we will discuss the systematic uncertainties associated with the measurement of the strong coupling constant in jet production. The experimental systematic uncertainties originating from the uncertainties in the inclusive jet cross section are calculated. The theoretical uncertainties such as renormalization scale uncertainty and different choice of parton distribution functions are estimated.

7.1 Experimental Systematic Uncertainties

To estimate the experimental systematic uncertainty on the α_s measurement we should first consider experimental uncertainties associated with inclusive jet production at CDF. As described above (Section 5.2), most of the systematic uncertainties in the inclusive jet cross-section measurement arise from our understanding of the calorimeter response to jets. The detector response and jet energy corrections are derived from a combination of test-beam data and Monte-Carlo simulations. The eight potential sources of uncertainties in jet measurements were identified and discussed in Section 5.2.1. For each of these sources the shifts in the response func-

Uncertainty	P0	P1	P2	P3	P4	P5	P6
Nominal	0.14946×10^7	-2.9228	4.4881	-4.9447	1.7891	-0.2297	5.6147
+							
High Pt Pion	0.11521×10^7	-2.7511	4.4129	-4.9487	1.7989	-0.2325	5.3079
Low Pt Pion	0.16445×10^7	-2.9824	4.4867	-4.9415	1.7911	-0.2287	6.3165
Energy Scale	0.15275×10^7	-2.9176	4.4883	-4.9449	1.7889	-0.2297	5.4732
Fragmentation	0.17922×10^7	-3.0070	4.4857	-4.9406	1.7917	-0.2285	6.5970
Under. Event	0.23917×10^6	-2.2945	4.4609	-4.9923	1.7764	-0.2228	5.8629
EM Scale	0.14852×10^7	-2.9146	4.4884	-4.9451	1.7888	-0.2298	5.4920
Resolution	0.10392×10^7	-2.8451	4.4958	-4.9455	1.7878	-0.2304	5.4340
-							
High Pt Pion	0.12506×10^7	-2.7639	4.3972	-4.9442	1.8030	-0.2324	5.6243
Low Pt Pion	0.13604×10^7	-2.8651	4.4891	-4.9479	1.7870	-0.2306	4.9412
Energy Scale	0.14757×10^7	-2.9299	4.4878	-4.9444	1.7892	-0.2296	5.7798
Fragmentation	0.12561×10^7	-2.8404	4.4904	-4.9487	1.7865	-0.2308	4.6655
Under. Event	0.34976×10^7	-3.1079	4.4710	-4.9422	1.7923	-0.2279	6.3048
EM Scale	0.15065×10^7	-2.9332	4.4877	-4.9443	1.7893	-0.2296	5.7700
Resolution	0.20458×10^7	-2.9888	4.4814	-4.9441	1.7901	-0.2291	5.7412

Table 7.1: Parameters for systematic error curves.

tions were evaluated. The modified response functions were then used to perform the unsmearing procedure and to obtain a new corrected cross section. The difference between the new corrected cross section and the nominal one is defined as the *one σ* uncertainty. The curves corresponding to each of these uncertainties are presented in Fig. 7.1. The parameters for the systematic uncertainty curves are listed in Table 7.1 and are quoted from [38]. The subgroups of experimental systematic errors for the jet cross section are denoted by (1)-(8), see Fig. 7.1. The uncertainties on the charged pion response (1), (2) are divided into two parts depending on the particle momenta, and determined either from test beam data for high p_T pions or from isolated charged tracks in the CTC. The jet energy scale (3) includes the calorimeter response stability over time, which is estimated to be better than 1%. The error

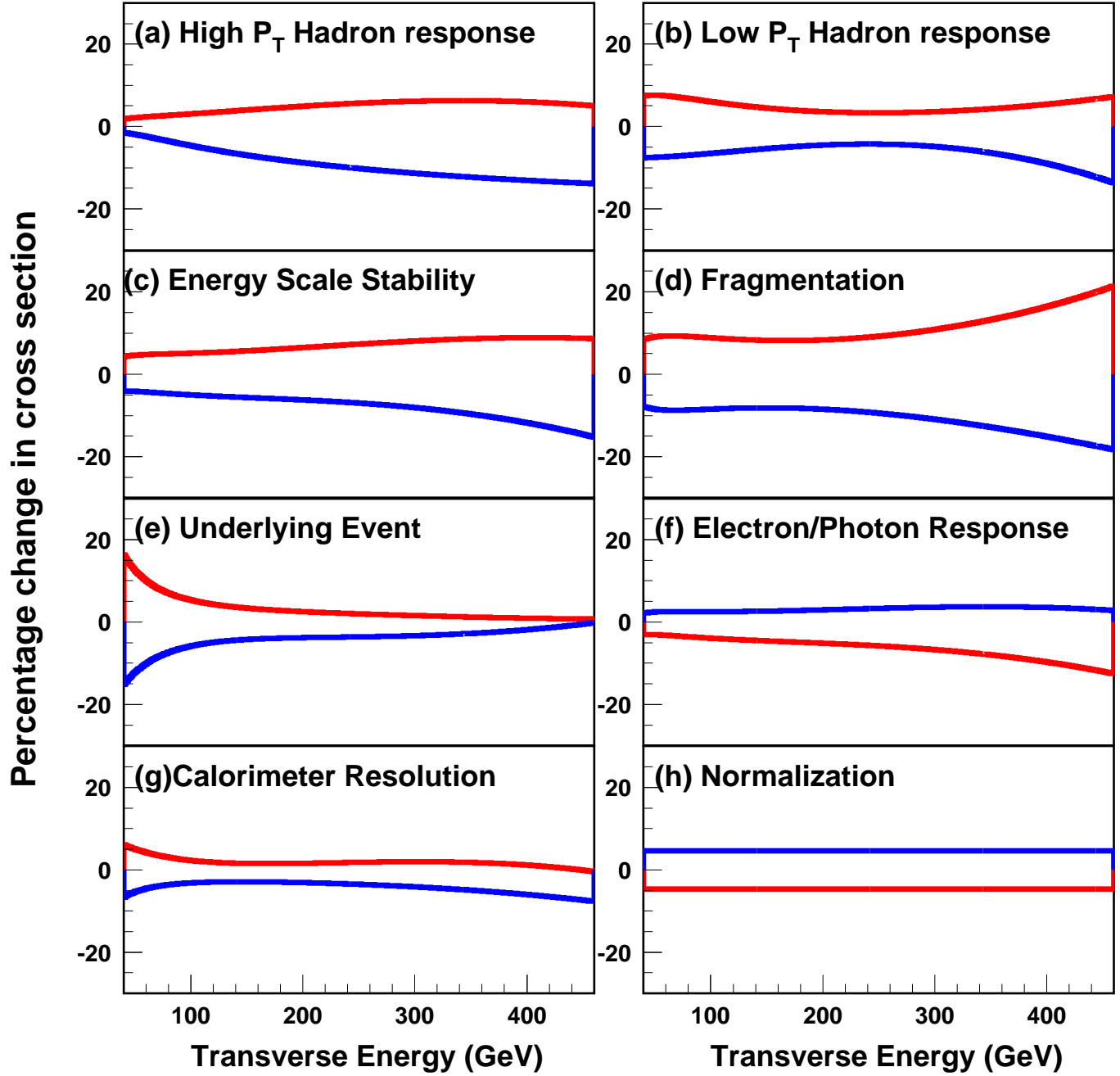
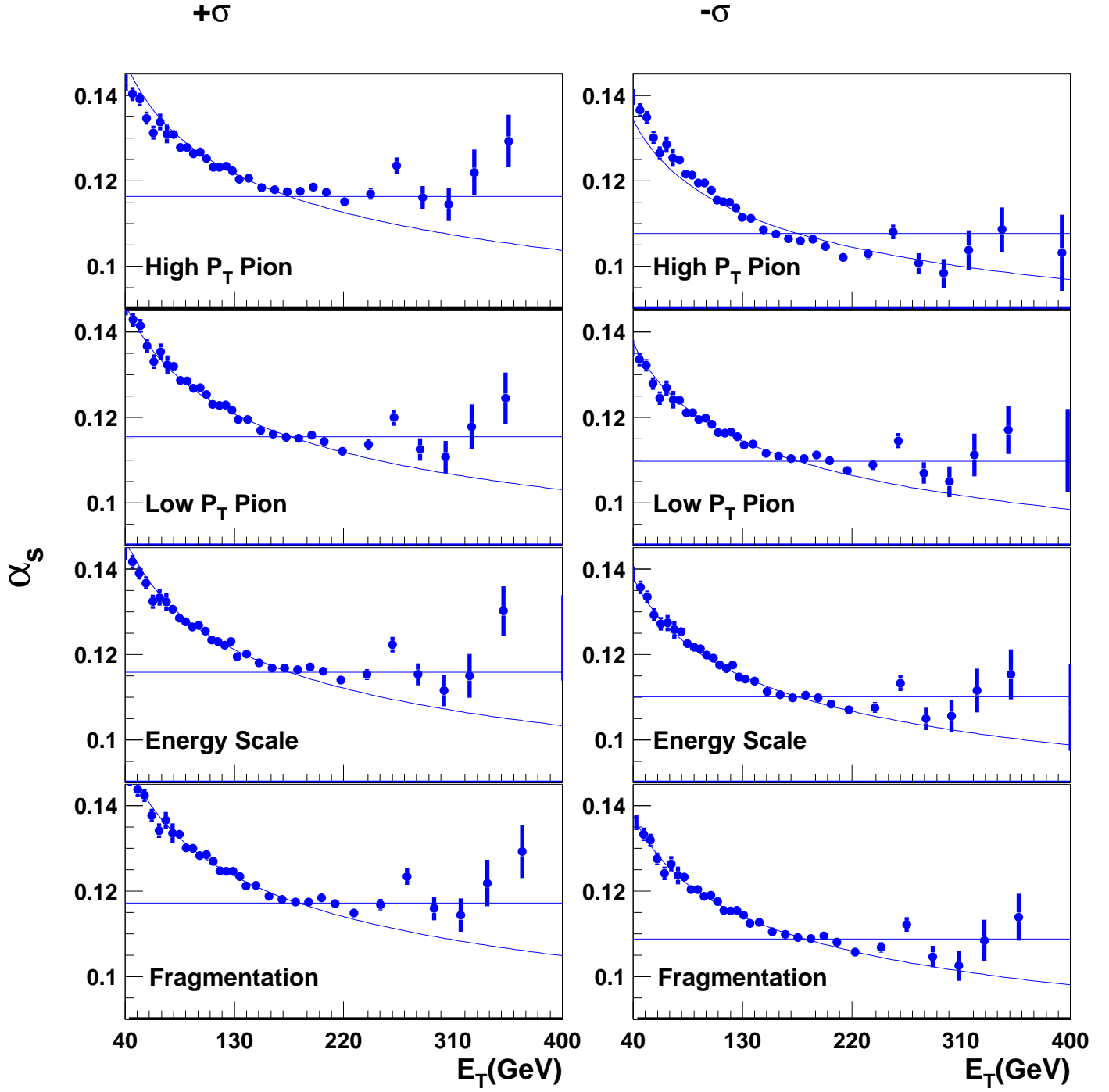
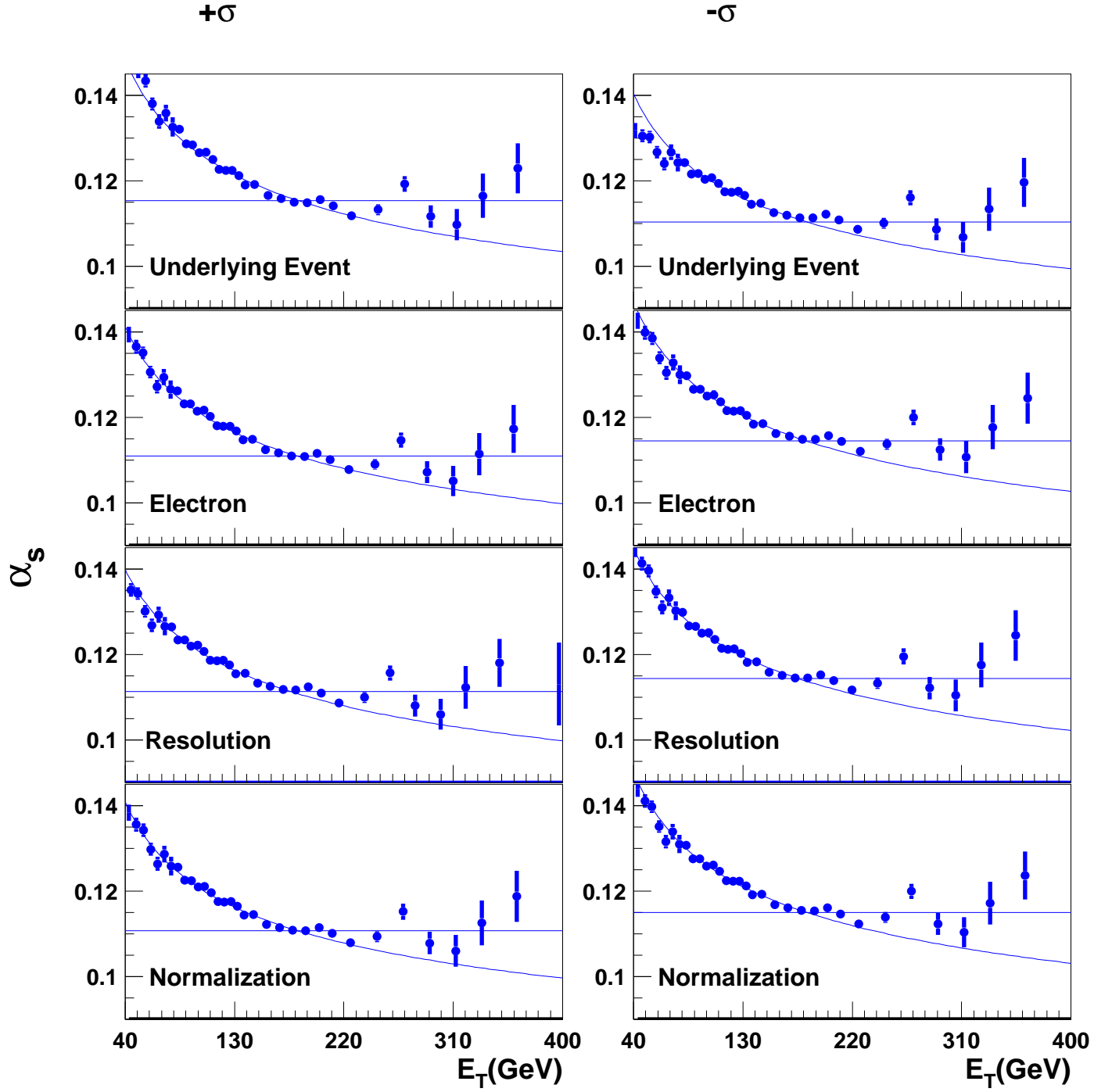


Figure 7.1: Systematic uncertainties for the inclusive jet cross section.

Figure 7.2: α_s extracted for different sources of systematic uncertainties.

Figure 7.3: α_s extracted for different sources of systematic uncertainties.

Source of Uncertainty	α_s	$\Delta\alpha_s$	$\Delta\alpha_s/\alpha_s$ (%)
Standard	0.1129	–	–
Calorimeter Electron Response	0.1145 0.1110	+0.0016 –0.0019	+1.4% –1.7%
Underlying Event Energy Subtraction	0.1153 0.1104	+0.0024 –0.0025	+2.1% –2.2%
Jet Fragmentation Functions	0.1173 0.1088	+0.0044 –0.0041	+3.9% –3.6%
Jet Energy resolution	0.1143 0.1114	+0.0014 –0.0015	+1.2% –1.3%
Calorimeter Low P_T Pion Response	0.1155 0.1098	+0.0026 –0.0031	+2.3% –2.7%
Calorimeter High P_T Pion Response	0.1163 0.1077	+0.0034 –0.0052	+3.0% –4.6%
Energy Scale	0.1158 0.1100	+0.0029 –0.0029	+2.6% –2.6%
Normalization	0.1150 0.1107	+0.0021 –0.0022	+1.9% –1.9%

Table 7.2: Experimental systematic uncertainty on the extracted $\alpha_s(M_Z)$ for the CTEQ4M PDF set.

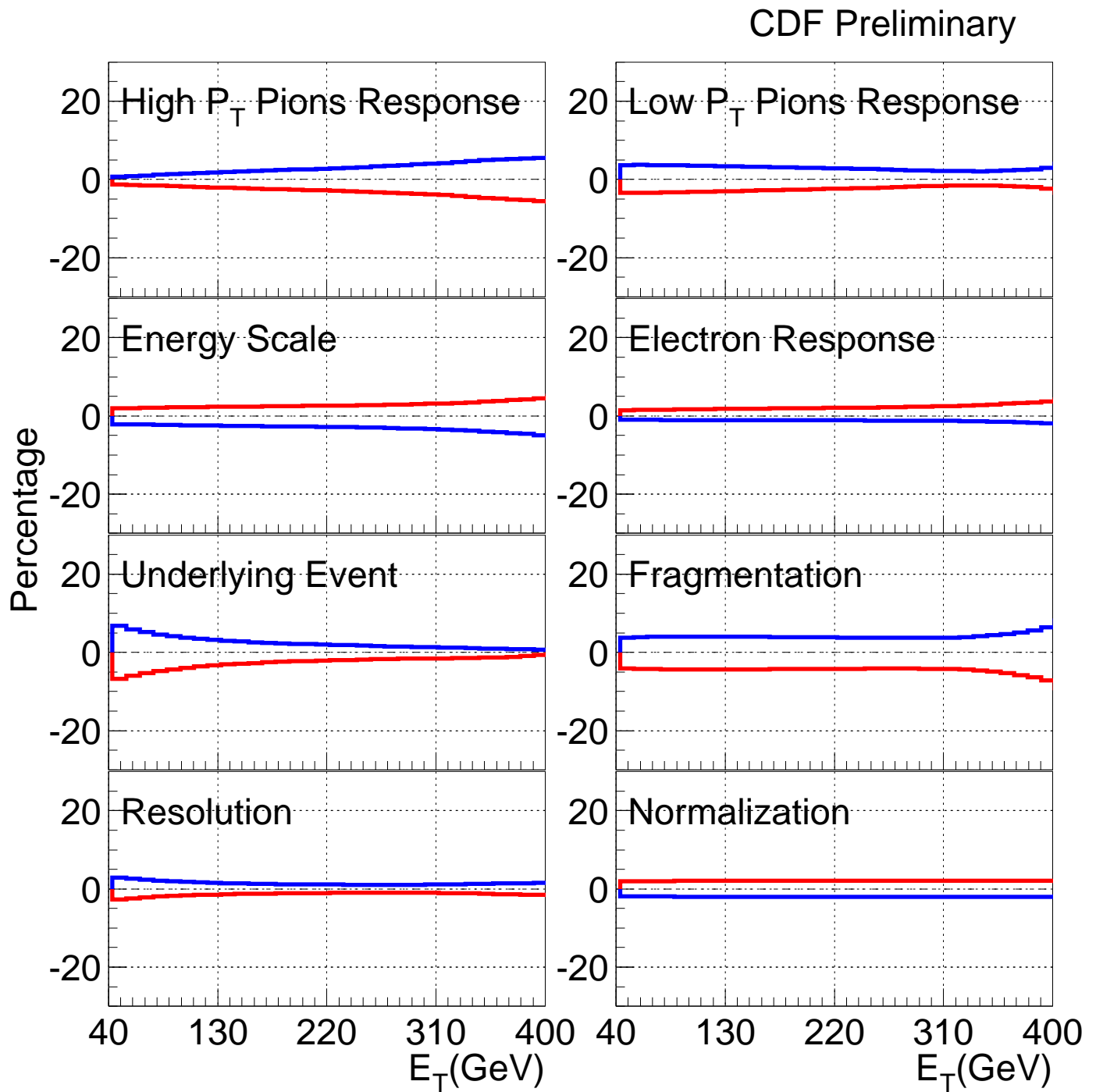


Figure 7.4: Systematic uncertainties for α_s measurement.

from the jet fragmentation functions (4), such as track multiplicity, track momentum distribution, etc, is due to a lack of knowledge of the track properties. The error from the underlying event subtraction (5) is assigned a very conservative uncertainty of 30%. The jet energy resolution (6) error is $\pm 10\%$. The electron response error (7) is assigned $\pm 2\%$. The normalization uncertainty (8) for the CDF 1994-1996 data is 4.5% and comes from the uncertainty on the luminosity measurement (4.1%) and the efficiency of the z_{vertex} cut (2%).

The next step in estimating the uncertainties in the α_s measurement is to extract $\alpha_s^{sources}(E_T)$ from the shifted physics curves with the parameters from Table 7.1, and to compare with $\alpha_s^{standard}(E_T)$ extracted from the nominal physics curve. The $\alpha_s^{sources}(E_T)$ as a function of E_T are shown in Fig. 7.2 and 7.3. We define the experimental systematic uncertainties in our measurement as the ratios of $\alpha_s^{standard}$ to $\alpha_s^{sources}$. The error curves are shown in Fig. 7.4. The biggest source of uncertainty comes from the high- P_T pion response, see Table 7.2. When added in quadrature, the experimental systematic uncertainty is $^{+0.0078}_{-0.0089}$ or about $^{+6.9\%}_{-7.9\%}$.

7.2 Theoretical Uncertainties

The theoretical uncertainties on the α_s measurement are mostly associated with the lack of knowledge of higher order terms in pQCD and our understanding of non-perturbative effects, which are mirrored as uncertainties in the input parameters for the JETRAD program. The main sources of uncertainties are the choice of renormalization and fragmentation scales μ_R and μ_F , the choice of clustering algorithm, the dependence on the parameter R_{sep} , and certainly the choice of parton distribution functions (PDFs).

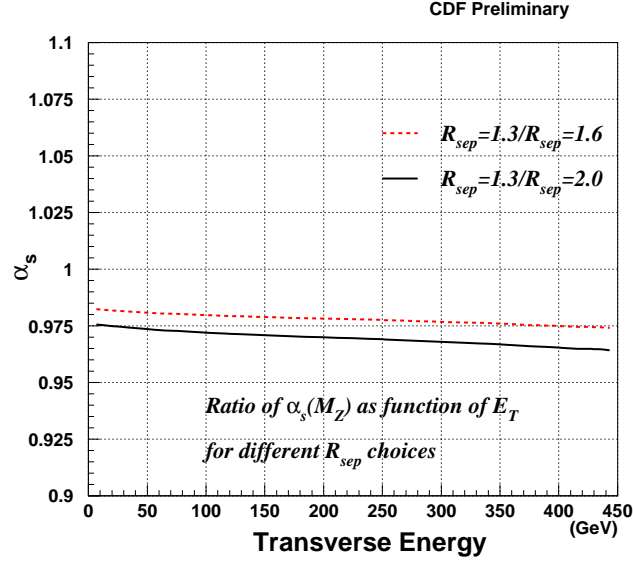


Figure 7.5: Estimate of the uncertainty on $\alpha_s(M_Z)$ due to different choices of R_{sep} .

From this list the biggest uncertainties come from the choices of the scale and PDFs, which we will discuss later.

In Section 4.1 we discussed basic features of theoretical and experimental clustering algorithms. A more efficient jet-jet separation by the experimental algorithm led to the introduction of a new parameter R_{sep} in the theoretical algorithm to approximate the experimental way of separating and merging. As mentioned before, the best agreement with the experimental results corresponds to the value $R_{sep} = 1.3$. The uncertainty associated with different choices of R_{sep} (from $R_{sep} = 1.3$ to 2) corresponds to a 5–7% normalization uncertainty on the jet cross section, and to a 2–3% uncertainty on the $\alpha_s(M_Z)$ measurement, see Fig. 7.5.

μ_R	$\alpha_s(M_Z)$	$\Delta\alpha_s(M_Z)$ (%)
$\mu_R^{standard} = E_T/2$	0.1129	—
$\mu = 3E_T/4$	0.1158	+2.5%
$\mu = E_T$	0.1178	+4.3%
$\mu = 5E_T/4$	0.1198	+6.1%
$\mu = 3E_T/2$	0.1217	+7.8%
$\mu = 7E_T/4$	0.1233	+9.2%
$\mu = 2E_T$	0.1249	+10.6%

Table 7.3: μ -scale uncertainty on the extracted $\alpha_s(M_Z)$ for the CTEQ4M PDF set.

7.2.1 Choice of the Renormalization scale

The fundamental theorem of the renormalization scheme dependence states that physical quantities calculated to all orders in perturbation theory do not depend on the renormalization scheme. This means that truncated series *do* exhibit renormalization scheme dependence. Since in QCD the inclusive jet cross section is known to next-to-leading order, the renormalization scheme dependence is given by one condition that is the dependence on the renormalization scale μ_R ¹. Therefore we have to choose the scale which will be best for our measurement. As mentioned before, usually μ_R is chosen to be of the order of the characteristic scale of the process. We can also vary μ_R to estimate the sensitivity of the measurement to the choice of renormalization scale.

We changed the $\mu_R = \mu_F$ scales from $\mu_R = E_T/2$ to $\mu_R = 2E_T$ in the input to the JETRAD program and repeated the whole procedure to extract $\alpha_s(E_T)$ and $\alpha_s(M_Z)$. The sensitivity of our measurement can be estimated from the shift in α_s as μ_R is changed from $E_T/2$ to $2E_T$. In Fig. 7.6 we plot $\alpha_s(M_Z)$ as a function of E_T

¹At NNLO the choice of μ_R is not equivalent to the choice of the renormalization scheme and both must be specified.

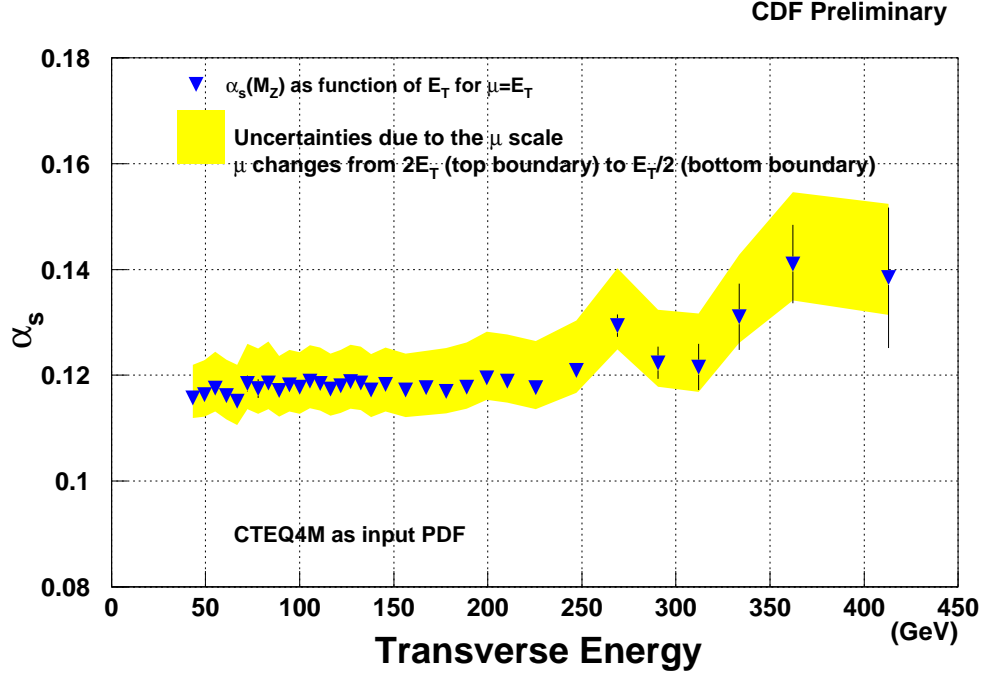


Figure 7.6: Uncertainties due to the change in renormalization scale.

with the corresponding error band due to the μ_R scale. Over the E_T range from 50 to 250 GeV the uncertainty amounts to a normalization uncertainty of 4 – 6% and is flat in shape.

The numbers cited above are given for comparison with other α_s measurements and general understanding of how this uncertainty can affect our measurement. However, it is our understanding that assignment of the error on the average value of $\alpha_s(M_Z)$ would be ambiguous. The variation of μ scale over reasonable range gives us

understanding of the sensitivity of our results to the choice of renormalization scale, but assignment of the theoretical uncertainty by using this method will depend on a subjective judgment about the definition of “reasonable”. The resolution to this problem lies with the calculation of even more terms in the perturbative series. For inclusive jet production this method will provide a correct estimate of the μ -scale uncertainty, since non-perturbative effects are small.

7.2.2 Parton Distribution Functions

The dominant uncertainty on the measurement of α_s from the inclusive jet cross section comes from the choice of parton distribution functions. The initial requirement for interpreting the results is the consistency of α_s values generic to the PDF set used in the analysis and the “output” α_s obtained from the measurement. This condition is important to ensure the compatibility of the data with particular parton distributions. The α_s dependence of the PDF is a major disadvantage of measurements at hadron colliders in comparison to measurements of the strong coupling constant from the Z width at LEP. Before discussing particular choices of PDFs we elaborate a little more on the subject.

As discussed before (see Section 2.4), the distributions of quarks and gluons inside hadrons are described by the parton distribution functions. A lot of effort is devoted to studies of PDFs. The two main reasons for that are experimental and theoretical. First, a detailed knowledge of parton distribution functions is essential for the study of all hard interaction processes, and should be used to estimate the production rates of hard processes which may occur at present and future high energy colliders. The theoretical reason is the interest in the subject of parton structure by itself, especially in new studies at small x , such as diffractive studies at HERA and

the Tevatron [40].

At present there are three collaborations producing parton distributions which are used in high-energy collider phenomenology. They are MRS (Martin-Roberts-Stirling), CTEQ (Collaboration for Theoretical and Experimental Studies in Quantum Chromodynamics) and GRV (Glück-Reya-Vogt). The first two groups use a so-called “global” fit, which is based on the idea of adjusting the parton distribution functions to make theory and experiment agree for a wide range of processes. The GRV analysis is done in the context of the “dynamical parton model”, according to which the partons evolve from valence-like distributions at low Q^2 which are then tuned to fit the data at higher Q^2 . During the last few years there has been spectacular improvement in the precision and in the kinematic range of the experimental measurements in hard scattering processes. As a consequence the PDFs are much better known now, with tighter constraints on the gluon and the quark sea for x as low as 10^{-4} . Since most inclusive jet data are collected in the central rapidity region, the x -value of the PDF’s probed is around $x_T = 2E_T/\sqrt{s}$. For $50 \text{ GeV} < E_T < 450 \text{ GeV}$, the x range is approximately 0.06-0.5. Over this range the relative importance of the three parton subprocesses contributing to the jet cross section shifts continuously, as illustrated in Fig. 7.7. At largest energies the process is dominated by quark-quark scattering, and at low E_T by gluon-gluon scattering. The quark-gluon contribution is significant at all energies, even at high E_T , where it contributes around 20%. Since the momentum distributions of partons are universal, the PDFs could be derived from any process and applied to jet production. However the range covered by jet measurements extends to $x \sim 0.5$, which is not accessible to DIS experiments, so the question of how much independent measurements of parton distributions would constrain our knowledge of PDFs at large x is still open.

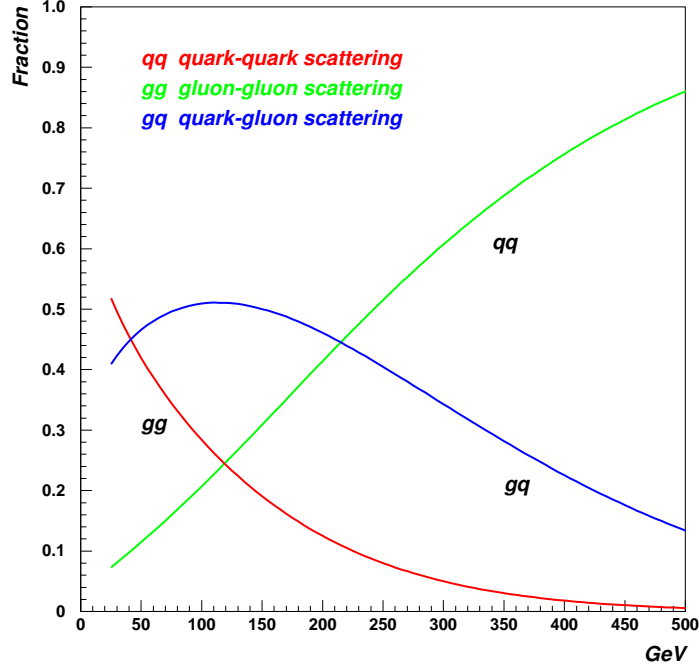


Figure 7.7: Various processes contributing to the inclusive jet cross section.

To better understand how the PDFs can contribute to the uncertainties on our results, we now describe how the PDFs are produced in the global fitting scheme. One chooses an initial scale $\mu \sim \text{few GeV}$; the $f_i(x, Q^2)$ - PDFs are written as functions of several parameters for $g, u, \bar{u}, d, \bar{d}, s, \bar{s}$. For example, $f_i(x, Q^2)$ could have the form of:

$$f_i(x, Q^2) = Ax^B(1-x)^C(1+Ex^D), \quad (7.1)$$

where A, B, C, D, E are free parameters. Typically 20 to 28 parameters are needed to describe the data very well. Some of the parameters are constrained by flavor conservation and momentum sum rules.

The deep-inelastic structure functions directly constrain the valence and sea quark distributions to within a few percent at large x ($x > 0.2$), translating to a

maximum 5% uncertainty on the jet cross section. The situation with the gluon distributions is not that simple. Despite the sensitivity of many processes to the gluon distributions it is still difficult to put constraints in the range of $x \geq 0.2$, where the gluon distributions become small. The MRS group used prompt photon data from the the WA70 experiment to determine gluons, however this process suffers from scale dependence and effects of intrinsic k_T . In the small- x domain the gluon distributions are well constrained by the observed behavior of $\partial F_2/\partial \log Q^2$. However this presents additional difficulty for our analysis in particular since there is an α_s -gluon correlation, due to $\partial F_2/\partial \log Q^2 \sim \alpha_s P^{qg} \otimes g$. A study by CTEQ collaboration shows that a change of α_s by 8% results in a 3% change in the gluon distributions for $x < 0.15$ at $Q = 110$ GeV. The study of uncertainties associated with $\alpha_s \otimes g$ correlation by MRS collaboration also showed that the jet cross section is more sensitive to the variation in α_s than to the change in the gluon distribution [43].

CTEQ4 PDF sets

Many uncertainties in the PDFs arise from uncertainties in the data used for global fits, extrapolation from the fits, and evolution to different energy scales, since most of the data is obtained from energies lower than those at the Tevatron. Recent PDF sets have started to quantify some these uncertainties by producing families of PDFs in which some of parameters can vary, for example α_s . One of the first studies of flexibility of parton distribution functions was originated by the CTEQ collaboration [41] to explain the excess over theory observed in the CDF Run1A inclusive jet cross section. It was shown that gluon distributions are flexible enough at high x to produce a significant increase in the inclusive jet cross section at high energies, while still having good agreement with data in the global fit. After including

high precision DIS data and Tevatron jet data (all data published before 1996) in the global fit, the family of CTEQ4 PDFs were produced, from which CTEQ4HJ was a particular PDF with a modified gluon distribution and a higher statistical weight assigned to the Tevatron jet events with high E_T . CTEQ4HJ gives a better description of the CDF inclusive jet data from Run 1B (see Fig. 7.8) in comparison to the standard CTEQ4M set. Both CTEQ4M and CTEQ4HJ obtained $\alpha_s(M_Z)=0.116$ from the global fit.

We repeated the extraction of α_s using CTEQ4HJ with estimates of the experimental systematic uncertainties. The results are presented in Fig. 7.9 and Table 7.4. As expected, the extracted $\alpha_s(M_Z)$ has a higher value than the $\alpha_s(M_Z)$ corresponding to CTEQ4M. The somewhat excessive behavior of $\alpha_s(M_Z)$ as function of E_T at high E_T values is more in line with the theory predicted independence with respect to E_T .

The series CTEQ4A were produced with the purpose of pinpointing the uncertainty associated with the variation of $\alpha_s(M_Z)$. There are five PDFs, each corresponding to a different α_s value: CTEQ4A1 with $\alpha_s=0.110$, CTEQ4A2 with $\alpha_s=0.113$, CTEQ4A3 or CTEQ4M with $\alpha_s=0.116$, CTEQ4A4 with $\alpha_s=0.119$, and CTEQ4A5 with $\alpha_s=0.122$. The χ^2 per point from CTEQ global fit are 1.07, 1.02, 1.02, 1.07, 1.19 respectively. The further lowering of values of α_s is disfavored by data from HERA DIS experiments and further increase of α_s values disfavored by fixed-target DIS experiments. The corresponding α_s functions are presented in Fig. 7.10. The PDF set producing the best agreement in the shape of $\alpha_s(M_Z)$ as a function of E_T is defined as the default set. For our analysis the best agreement was obtained for the CTEQ4M PDF.

Other recent PDFs used in our analysis are those produced by the MRS

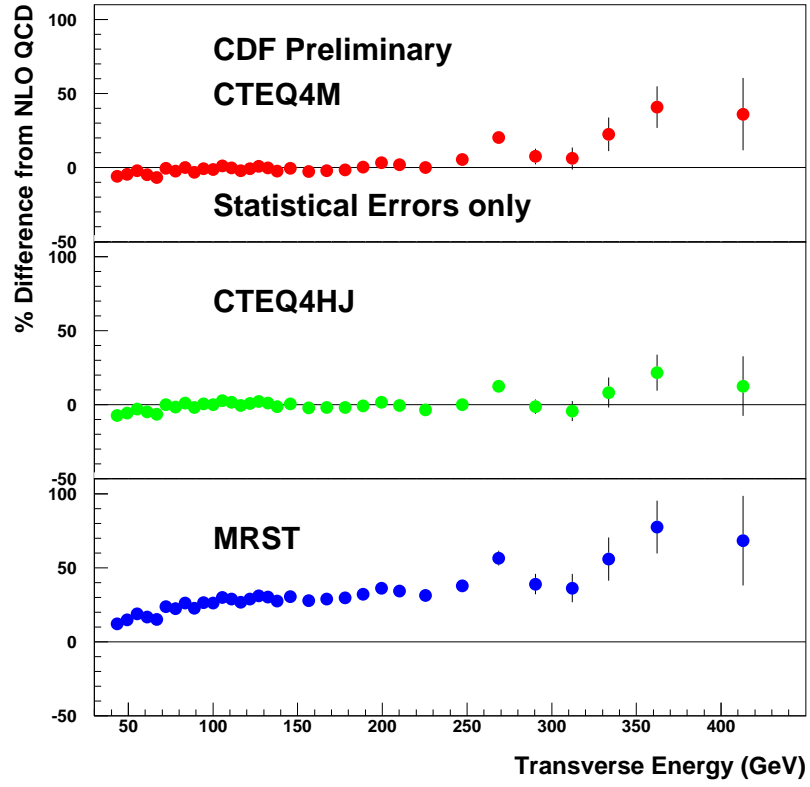


Figure 7.8: The percent difference between the preliminary Run1B inclusive jet cross section and QCD predictions for a variety of current PDFs [39].

CDF Preliminary

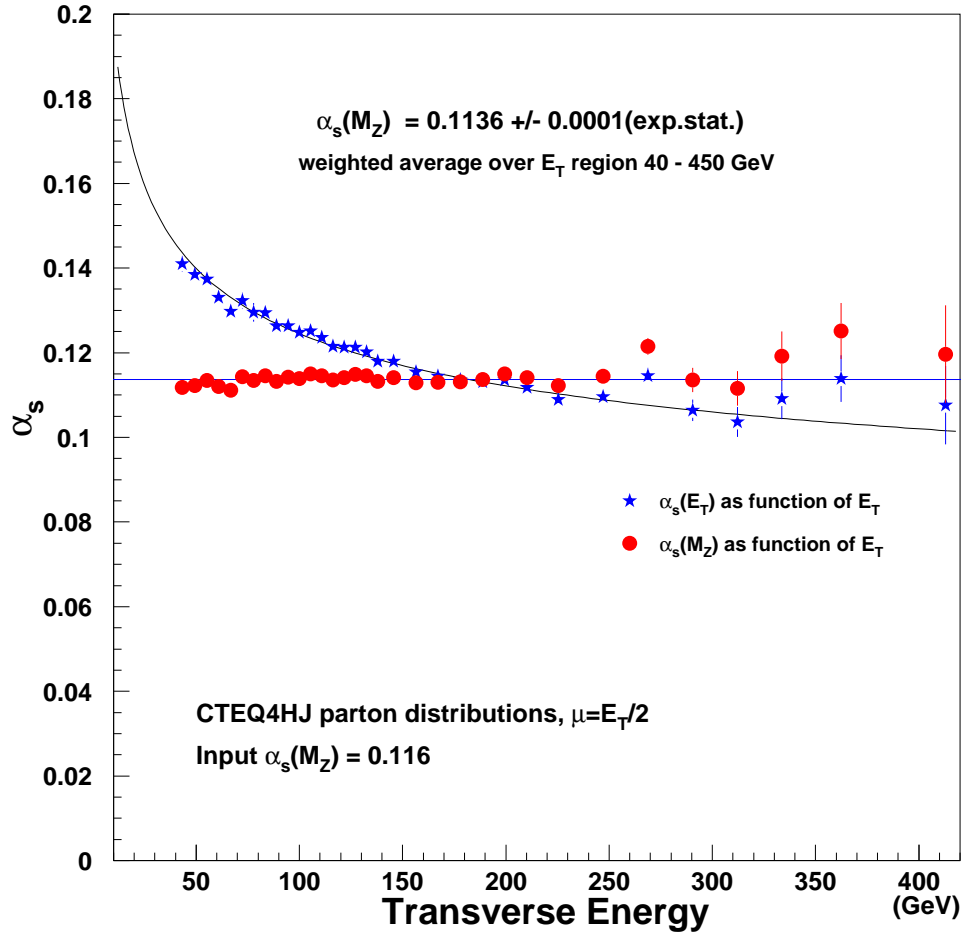
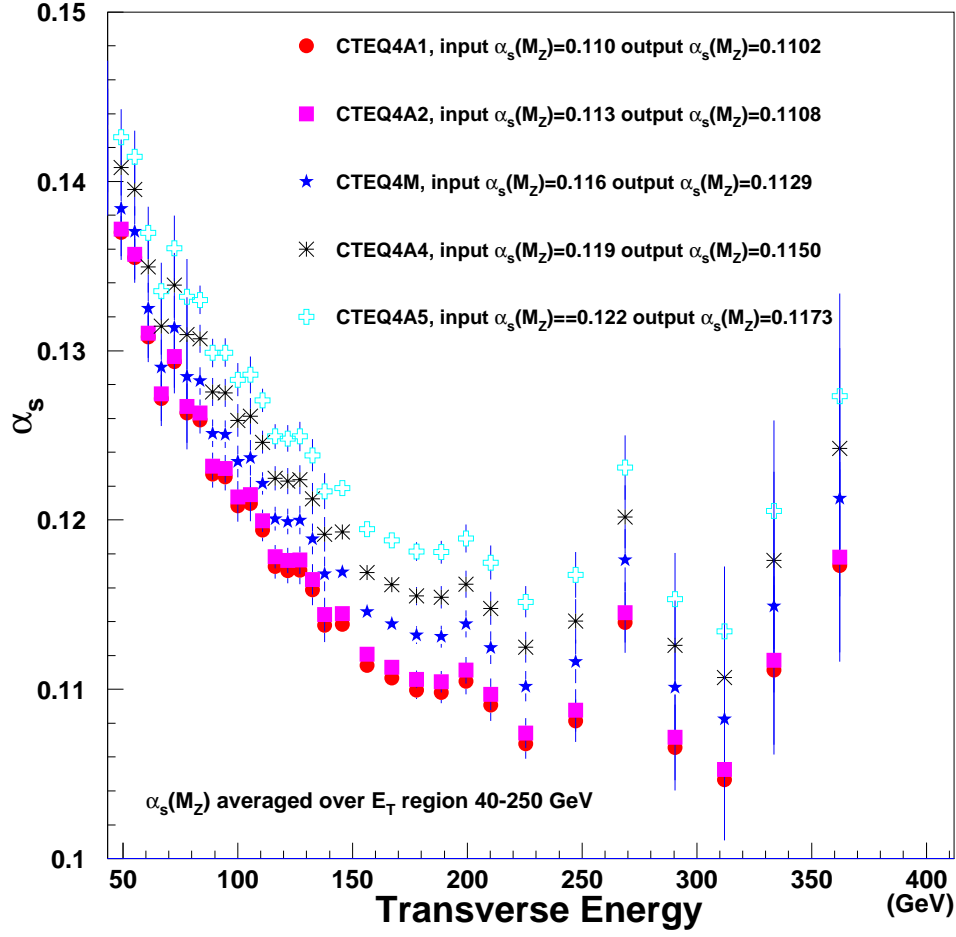


Figure 7.9: α_s using the CTEQ4HJ PDF set.

Source of Uncertainty	α_s	$\Delta\alpha_s$	$\Delta\alpha_s/\alpha_s$ (%)
Standard	0.1136	–	–
Calorimeter Electron Response	0.1150 0.1114	+0.0014 –0.0022	+1.2% –1.9%
Underlying Event Energy Subtraction	0.1161 0.1115	+0.0025 –0.0021	+2.2% –1.8%
Jet Fragmentation Functions	0.1183 0.1096	+0.0047 –0.0040	+4.1% –3.5%
Jet Energy resolution	0.1149 0.1124	+0.0013 –0.0012	+1.1% –1.1%
Calorimeter Low P_T Pion Response	0.1162 0.1107	+0.0026 –0.0029	+2.3% –2.6%
Calorimeter High P_T Pion Response	0.1169 0.1106	+0.0033 –0.0030	+2.9% –4.6%
Energy Scale	0.1158 0.1100	+0.0029 –0.0029	+2.6% –2.6%
Normalization	0.1159 0.1115	+0.0023 –0.0021	+2.0% –1.8%

Table 7.4: Experimental systematic uncertainty on the extracted $\alpha_s(M_Z)$ for the CTEQ4HJ PDF set.

Figure 7.10: α_s using the CTEQ4A series.

collaboration in the last few years.

MRSA' PDF sets

One of the oldest sets used for our analysis is MRSA' [42] which includes data published before 1994 and does not include Tevatron jet data. This family also has different PDFs for various values of α_s . Our interest in this set was motivated by the absence of the Tevatron jet data in the global fit. The results are presented

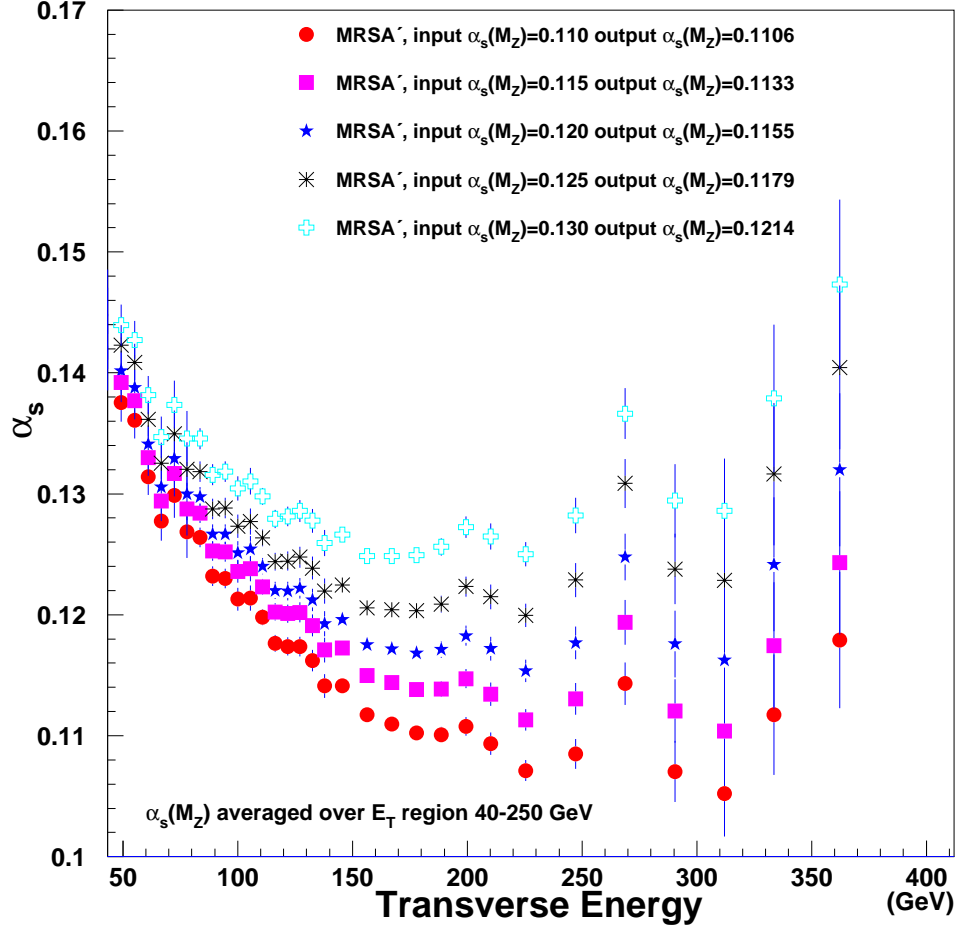


Figure 7.11: α_s using the MRSA' series.

in Fig. 7.11 and as one can see one of the PDFs - MRSA' with $\alpha_s(M_Z) = 0.110$ gives an average value of $\alpha_s(M_Z) = 0.1106$, which is almost the same as the input $\alpha_s(M_Z)$. The data points are very well described by MRSA' (Fig. 7.12).

MRS R PDF sets

The next set that came from the MRS collaboration was MRS R [43], which included high precision DIS measurements, especially HERA measurements of the

CDF Preliminary

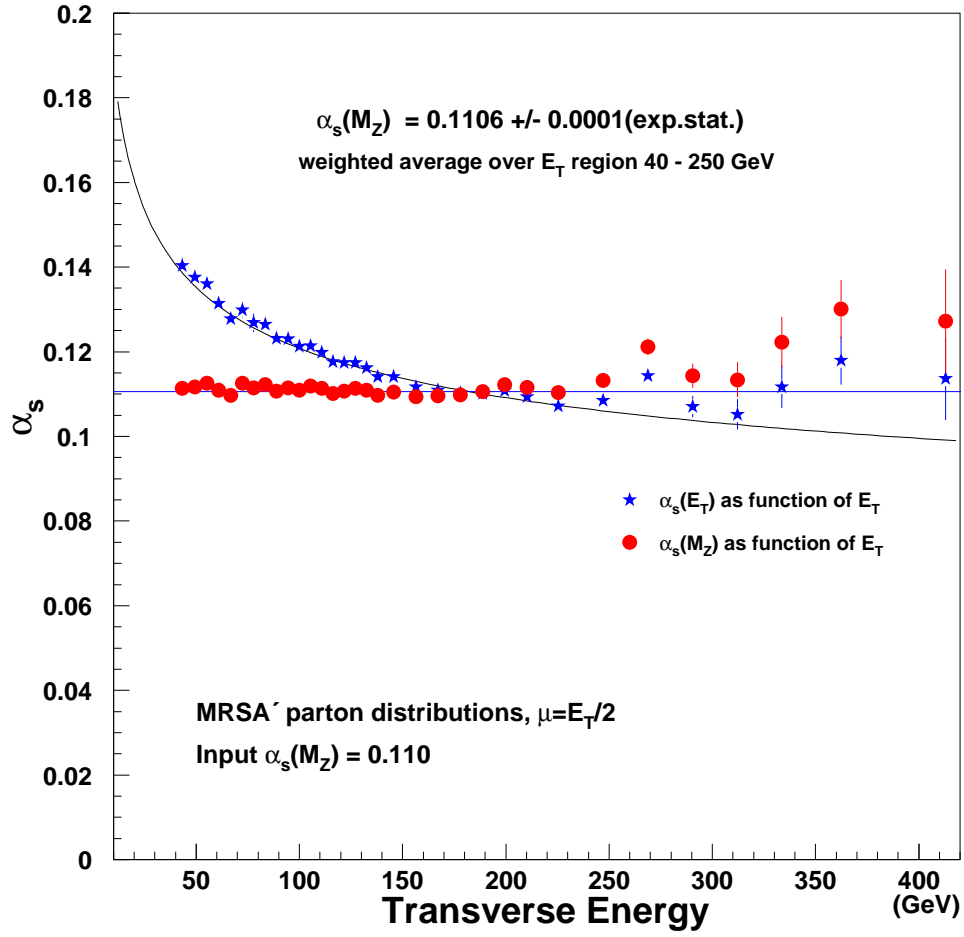


Figure 7.12: α_s using the MRSA' PDF set, input $\alpha_s(M_Z)$ is 0.110.

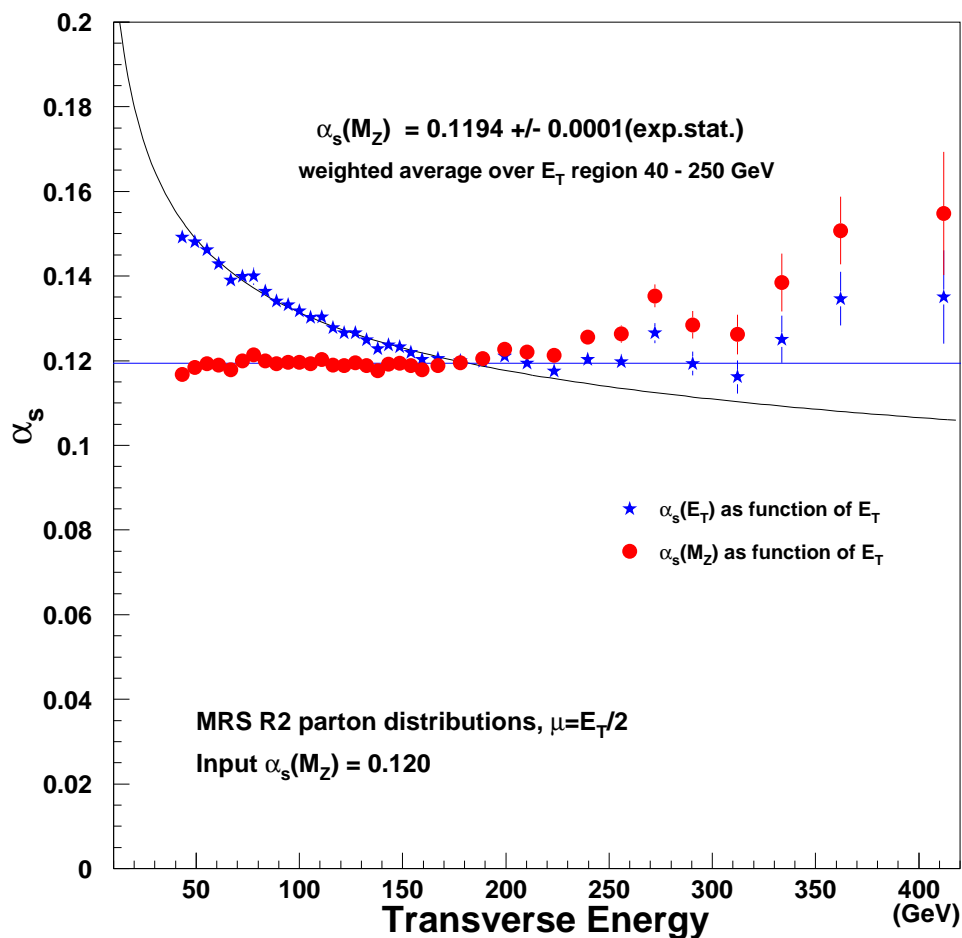


Figure 7.13: α_s using the MRS R2 PDF set, input $\alpha_s(M_Z)$ is 0.120.

proton structure function at small x , but still didn't include the Tevatron jet data. There are two sets: one intended for use with DIS experiments with lower α_s value and the other with $\alpha_s(M_Z) = 0.120$ to use with the theoretical predictions for colliders. We obtain good agreement for the MRS R2 set, with the results shown in Fig. 7.13.

Table 7.5: The various MRST PDF sets used in the analysis.

set	$\alpha_s(M_Z)$	comment
MRST	0.1175	default set with $\langle k_t \rangle = 0.4$ GeV
MRST($g \uparrow$)	0.1175	larger gluon at large x with $\langle k_t \rangle = 0.0$ GeV
MRST($g \downarrow$)	0.1175	smaller gluon at large x with $\langle k_t \rangle = 0.64$ GeV
MRST($\alpha_s \uparrow\uparrow$)	0.1225	larger α_s
MRST($\alpha_s \downarrow\downarrow$)	0.1125	smaller α_s

MRST PDF set

The latest MRS set is called MRST [44] and results from a NLO analysis in the \overline{MS} scheme. The degree of the flexibility of two parameters were studied, with; (a) variations of the average transverse momentum $\langle k_T \rangle$ in prompt photon production, which resulted in a range of gluon distributions at large x , and (b) variation in the value of $\alpha_s(M_Z)$. These uncertainties were reflected in the alternative sets of PDFs MRST($g \uparrow$), MRST($g \downarrow$), MRST($\alpha_s \uparrow\uparrow$), and MRST($\alpha_s \downarrow\downarrow$), see Table 7.5. For our analysis the set with values of $\langle k_T \rangle$ not equal to 0.0 GeV gives bad agreement with the data. The best overall agreement was produced by using MRST($g \uparrow$) which was basically the same MRS R set with the exception of using a lower value of $\alpha_s(M_Z)$ (Fig. 7.14). The plots for different $\alpha_s(E_T)$ functions for MRST PDFs are presented in Fig. 7.15.

We have presented the sensitivity of our measurement to the choice of parton distribution functions by plotting the different averaged values of $\alpha_s(M_Z) = \alpha_s^{output}$ obtained with these PDFs as a function of the input value $\alpha_s(M_Z)$. In Fig. 7.16 we plot for comparison the world average value with the associated error as a solid band. We estimate the uncertainty associated with the choice of parton distribution functions to be of the order of 10%. In Fig. 7.17 we illustrate dependence of results on

CDF Preliminary

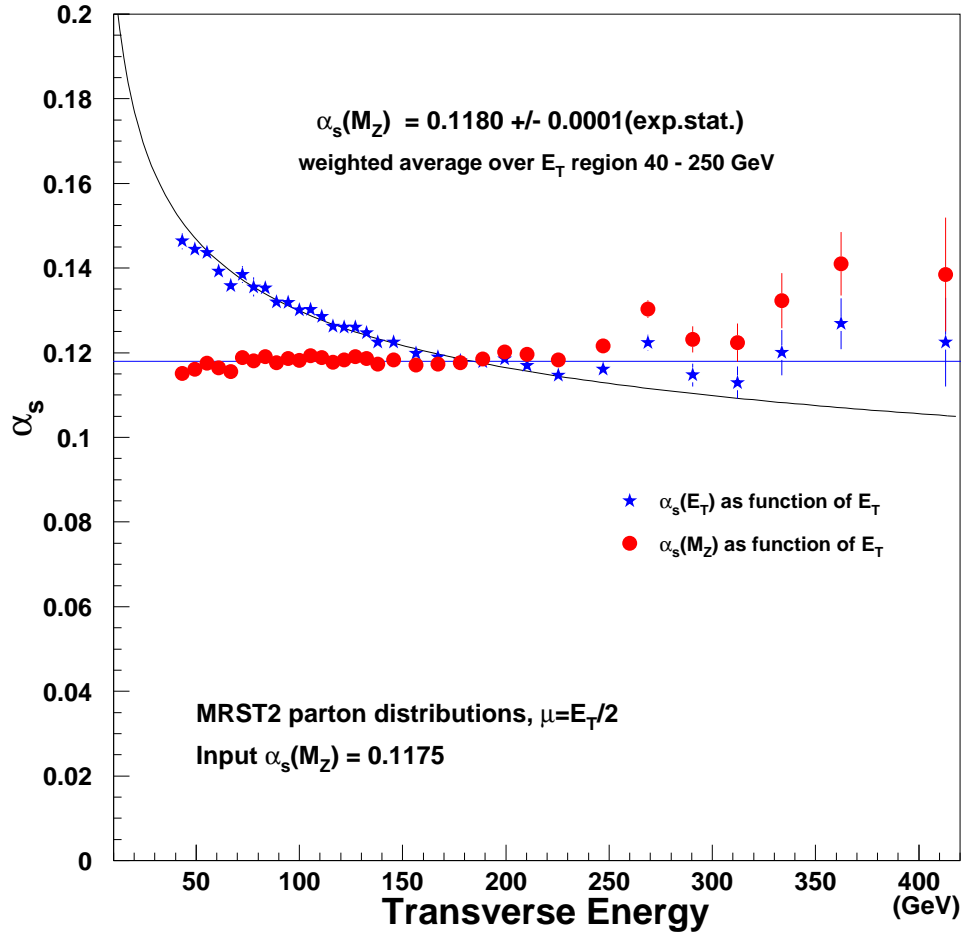


Figure 7.14: α_s using the MRST2 PDF set.

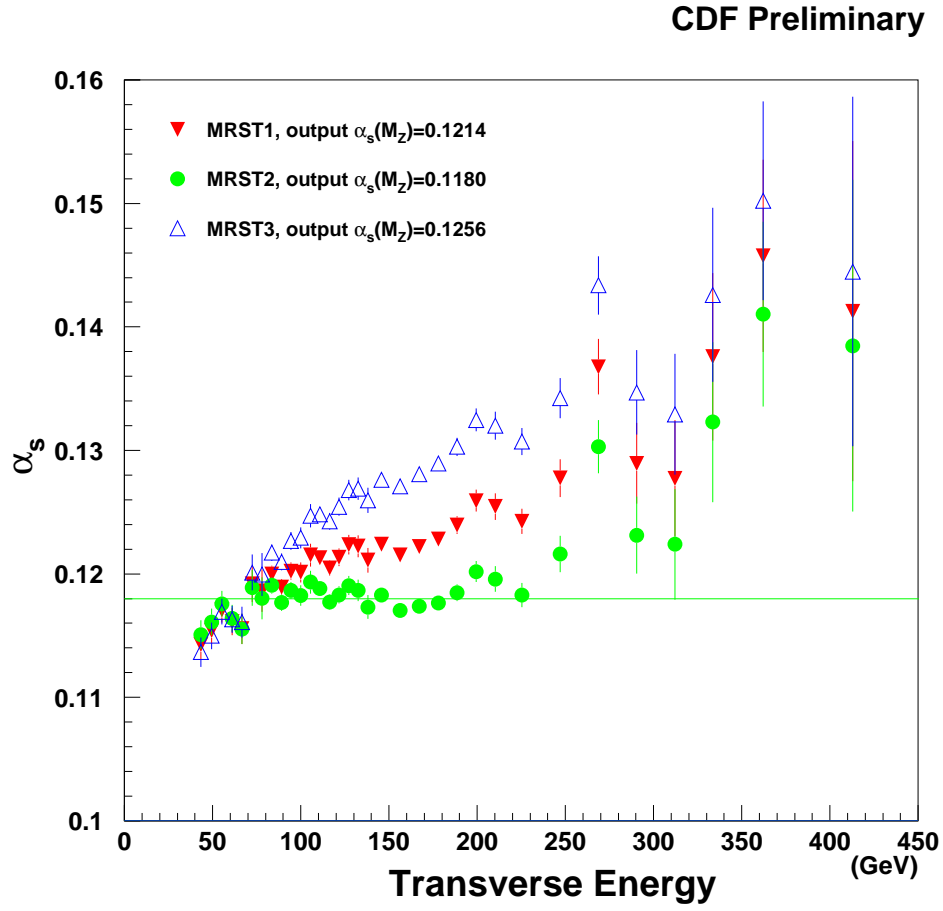


Figure 7.15: $\alpha_s(M_Z)$ as function of E_T using the MRST PDF sets.

CDF Preliminary

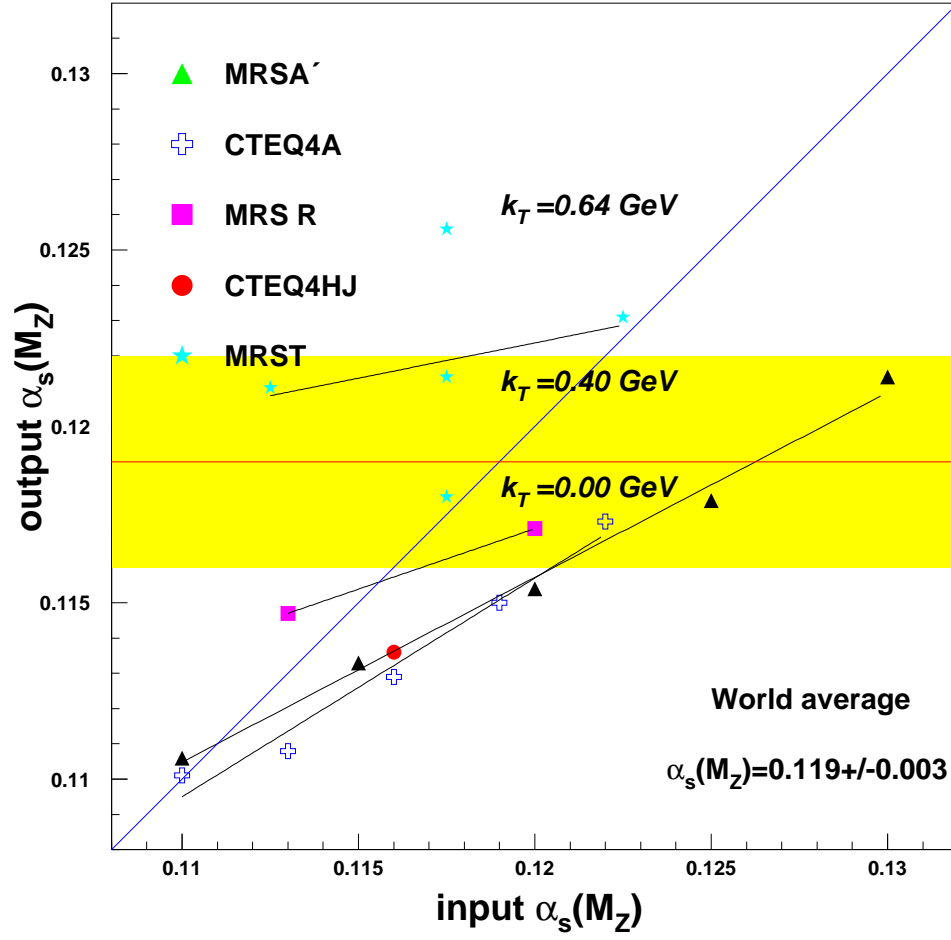


Figure 7.16: α_s extracted for different PDFs.

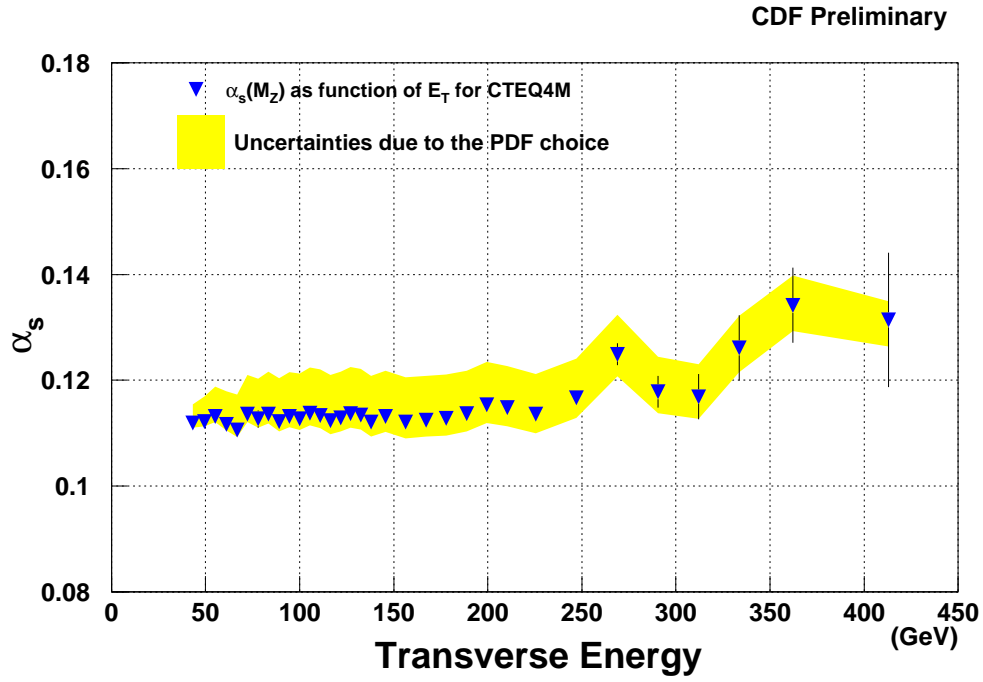


Figure 7.17: Uncertainties due to the choice of different PDFs. The bottom boundary corresponds to the CTEQ4A1 set with output $\alpha_s = 0.1102$ and top boundary corresponds to the MRST4 set with output $\alpha_s = 0.1211$.

PDF choice, the shaded area corresponds to the spread in $\alpha_s(M_Z)$ values for parton distributions which give reasonable χ^2 . Again one should note that only PDFs which produce values of α_s consistent with the input values are compatible with the CDF jet data, and can be used for future theoretical predictions of jet cross sections in Run II.

Chapter 8

Summary and Outlook

A precise measurement of the coupling constant and a verification of the running behavior of α_s remains a primary goal of experimental QCD studies. Enormous progress has been made in the determination of $\alpha_s(M_Z)$ during the past few years. It is important to notice that all different subsamples of results provide similar average values, with no systematic shifts between any of these subsamples.

In this chapter we discuss the current status of α_s measurements and put our own contribution in perspective.

8.1 Status of α_s

A wide range of methods is available for measuring the strong coupling constant α_s , with new measurements being continually reported. Before reviewing the current status of α_s we would like to comment on the phenomenon of the “shrinking error”. Since $\alpha_s(Q^2)$ is a function of Q^2 , the error in $\alpha_s(Q^2)$ is related to the error in

$\alpha_s(M_Z^2)$ in the following manner:

$$\frac{\delta\alpha_s(M_Z^2)}{\alpha_s(M_Z^2)} \sim \frac{\alpha_s(M_Z^2)}{\alpha_s(Q^2)} \frac{\delta\alpha_s(Q^2)}{\alpha_s(Q^2)}, \quad (8.1)$$

which means that the best relative precision is obtained at the lowest possible scale, where α_s is largest, since the relative error in α_s is shrunk by the ratio of $\alpha_s(M_Z^2)$ to $\alpha_s(Q^2)$. However, we should remember that at lower scales the non-perturbative corrections that might be negligible at higher scales can become important (for example due to possible sources of power-suppressed corrections ($1/Q^p$)), so the gain from measuring at low scales is compensated.

8.1.1 e^+e^- Annihilation

Over the last years a large amount of e^+e^- annihilation data in the energy range from 10 GeV to 189 GeV was accumulated at CESR, PETRA, PEP, TRISTAN, LEP, and SLC accelerators. The interaction $e^+e^- \rightarrow \text{hadrons}$ is the simplest possible QCD process to study. The energy scale of the process is exactly known and the hadronic interaction is limited to the final state. For many observables the hadronization corrections are proportional to $1/Q$ and are better understood now. Therefore many measurements of α_s came from LEP and PETRA. Due to the huge cross section at the Z^0 resonance several million hadronic events have been collected, allowing for a precise determination of $\alpha_s(M_Z)$ by each of the four LEP experiments.

Hadronic decay width

For the inclusive ratio:

$$R = \frac{\sigma(e^+e^- \rightarrow \text{hadrons})}{\sigma(e^+e^- \rightarrow \mu^+\mu^-)}, \quad (8.2)$$

the higher order QCD corrections have been calculated and the results can be expressed in terms of the factor:

$$R = R^{(0)} \left[1 + \frac{\alpha_s}{\pi} + C_2 \frac{\alpha_s^2}{\pi} + C_3 \frac{\alpha_s^3}{\pi} + \dots \right], \quad (8.3)$$

where $C_2 = 1.411$ and $C_3 = -12.8$. The principal advantage of this method is that there is no dependence on fragmentation models, jet algorithms, etc. α_s values extracted from this measurement by CLEO [45] yield $\alpha_s(10.52 \text{ GeV}) = 0.20 \pm 0.01 \pm 0.06$, which corresponds to $\alpha_s(M_Z) = 0.13 \pm 0.005 \pm 0.03$.

Measurements of the ratio of the hadronic to leptonic width of the Z boson at LEP and SLC yield $\alpha_s(M_Z) = 0.123 \pm 0.004$ [46]. Although this method has small theoretical uncertainties associated with QCD, it relies on the electroweak couplings of the Z boson to quarks. The theoretical errors are arising from the assumed value of the Higgs boson mass and from the choice of scale. Any appearance of new physics that will change the electroweak couplings via radiative corrections will modify the value of $\alpha_s(M_Z)$. However, excellent agreement of many measurements at the Z peak makes this method one of the most precise extractions of α_s today.

Event Shape Observables

In e^+e^- annihilation infra-red and collinear-safe observables can be constructed. At leading order they are directly proportional to α_s , so event shape variables that characterize the multijet topology are a common tool to measure α_s . An example of this kind of observable is the thrust $T = \max_{\vec{n}} (\sum_p |\vec{p} \cdot \vec{n}|) / (\sum_p |\vec{p}|)$. Another example is y_3 , defined by means of a jet clustering algorithm, where initially each particle is considered its own jet, then those two jets which are closest in phase space are combined by adding their 4-momenta. Iterating the procedure, y_3 is defined

as the distance where the event makes the transition from three to two jets. Common measures of the distance between jets i and j are the JADE metric [47] $y_{ij}^J = 2E_i E_j (1 - \cos \theta_{ij})/s$ and the Durham-metric [48] $y_{ij}^D = 2 \min(E_i, E_j)^2 (1 - \cos \theta_{ij})/s$, where in both cases θ_{ij} is the opening angle between the jets and s is the total invariant mass of the hadronic system. The theoretical predictions for these event shapes are known in NLO and for some of them the leading-logarithmic and next-to-leading logarithmic corrections have been resummed. However there are theoretical ambiguities associated with these measurements. The massive jets from these schemes cannot be directly compared to the massless jets from QCD. Different recombination schemes give different results from the same data, and the difference is used as a systematic error on the method. In addition the non-perturbative transformation from partons to hadrons gives rise to the power-law corrections, which are estimated by means of Monte-Carlo models and introduce additional hadronization corrections. The uncertainty of the scale at which α_s is measured also contributes to the theoretical uncertainty. Recently the DELPHI collaboration contributed a new measurement of α_s from oriented event shape distributions at LEP-1 energies. A good agreement between theory and data is obtained if both α_s and the renormalization scale μ are determined simultaneously [49]. Using 18 observables, DELPHI obtains $\alpha_s(M_Z) = 0.117 \pm 0.003$.

τ Decays

An inclusive quantity similar to R is the semi-leptonic branching ratio of the tau, $R_\tau = B_h/B_e$. The low energy scale involved requires good understanding of the non-perturbative (higher-twist) contributions, which are only suppressed by powers of the τ mass. However, it turns out that the non-perturbative corrections

are surprisingly small, which allows application of pQCD down to the scale of 1 GeV. Assuming the validity of the completeness relation for the tau branching ratios into hadrons, electrons and muons, and lepton universality, the ratio R_τ can be expressed as a function of B_e alone, (the larger mass of the muon leads to $B_\mu/B_e = 0.9726$):

$$R_\tau = \frac{1}{B(\tau \rightarrow e\nu\bar{\nu})} - 1.9726, \quad (8.4)$$

where B_e can be determined by direct measurement or again by assuming lepton universality from the mass and lifetime of the tau lepton and muon. Although the method has the potential of giving a very accurate measurement, the perturbative calculation does not converge well and the theoretical error is mostly due to the uncertainty in the perturbative prediction. The value of $\alpha_s(M_Z)$, averaged over the two determination of B_e , is $\alpha_s(m_\tau) = 0.35 \pm 0.03$, which corresponds to the $\alpha_s(M_Z) = 0.121 \pm 0.003$ [2].

8.1.2 Lepton-Hadron Scattering

The study of scaling violations in structure functions has the historical significance of establishing QCD as the theory of strong interactions. This continues to be an active field with the HERA ep collider at DESY.

An important theoretical issue is the presence of power-law corrections to the perturbative Q^2 -evolution of the structure functions $F_i(x, Q^2)$, or “higher-twist” (HT) contributions, of the form $1/Q^2$, which enter with x -dependent coefficients that cannot in general be calculated:

$$F_i(x, Q^2) = F_i(x, Q^2) + \frac{F_i(x, Q^2)^{(HT)}}{Q^2} \quad (8.5)$$

In cases where higher-twist contributions are important, the coefficient together with the value of α_s is extracted from fits to the data. The corresponding uncertainty

on α_s is assigned by varying the size of the higher-twist contribution within some reasonable range allowed by the data.

Sum rules

The structure functions can be resolved into singlet and non-singlet components. In QCD, singlet and non-singlet terms evolve differently with Q^2 . The singlet components receive a contribution from gluon splitting into $q\bar{q}$ pairs. As a consequence, the Q^2 evolution of the singlet term depends not only on the running coupling constant but also on the probability of gluon splitting, given by the gluon splitting function $g(x, Q^2)$. This dependence on the $g(x, Q^2)$ is not important if x is large enough (> 0.25) because the probability for gluon splitting at large x is small. Gluon splitting does not contribute to the non-singlet component of the structure function. The Q^2 evolution of this term depends on α_s only, not on x . Depending on the nature of the target (e.g. deuterium D_2 or hydrogen H_2), F_2 is either a pure singlet or a mixture of a singlet and a non-singlet, whereas F_3 is always a pure non-singlet.

The CCFR collaboration studied the Q^2 -dependence of the integral over x of xF_3 that defines the Gross-Llewellyn-Smith sum rule:

$$\int_0^1 dx (F_3^{\bar{\nu}p}(x, Q^2) + F_3^{\nu p}(x, Q^2)) = 6(1 - \Delta_{pert} - \Delta_{H.T.}), \quad (8.6)$$

where Δ_{pert} was calculated to NNLO and the higher twist correction (H.T.) was estimated using the QCD sum rule. The CCFR collaboration combines their data with that from other experiments [50] and gives $\alpha_s(\sqrt{3} \text{ GeV}) = 0.28 \pm 0.035(exp.) \pm 0.05(sys.) \pm 0.035(theory)$, which corresponds to $\alpha_s(M_Z) = 0.118 \pm 0.011$. The errors are dominated by higher-twist terms. A similar measurement is the extraction of α_s

from the higher order corrections to the Bjorken sum rules in polarized lepton-nucleon scattering.

Jet rates in ep collisions

A new method to determine α_s in ep collisions at intermediate to high scales is provided by measurements of jet production in deep-inelastic scattering (DIS) at HERA. At lowest order in α_s , the ep scattering process produces a final state of $1 + 1$ jets, one from the scattered quark in the process $e + q \rightarrow e + q$ and the other from the proton fragment. At NLO a gluon can be radiated, and a $(2+1)$ jet final state is produced. By comparing the rates for the $(2 + 1)$ to the $(1 + 1)$ jets processes a value of α_s can be obtained. An advantage over similar measurements at e^+e^- annihilation is the possibility to vary the range of the scales and test the running of α_s within the same experiment. The basic methodology is similar to the one used in our measurement. Combined results [51] from H1 and ZEUS yields $\alpha_s(M_Z) = 0.118 \pm 0.0015(stat) \pm 0.009(syst)$. Systematic errors mainly arise from the jet definition and the choices of scale and PDF.

8.1.3 Heavy Quarkonium Systems

Heavy quarkonium systems can be used to determine α_s either from the measured hadronic decay rate or via the strength of the binding provided by the strong potential; the latter is achieved in practice by comparing the measured energy-level splittings with a lattice QCD calculation.

Heavy Quarkonium Decays

If we assume that the short and long distance effects on decay widths of 3S_1 $Q\bar{Q}$ states can be factorized into the non-perturbative part depending on the confining potential, and a calculable perturbative part, then we can use the ratio to measure α_s . The ratio of the hadronic to the leptonic widths of a heavy quark-antiquark pair, with relativistic corrections taken into account will be:

$$\frac{\Gamma(q\bar{q} \rightarrow \text{hadrons})}{\Gamma(q\bar{q} \rightarrow \mu^+\mu^-)} = R_{pert} \left(1 + D \left\langle \frac{v^2}{c^2} \right\rangle \right), \quad (8.7)$$

with data available for $\Upsilon, \Upsilon', \Upsilon''$, and J/ψ . The theoretical corrections for this formulae are mostly due to the relativistic corrections ($v^2/c^2 \sim 0.1$ for Υ and ~ 0.25 for J/ψ), which are more important than the higher order perturbative corrections. The fit to the $\Upsilon, \Upsilon', \Upsilon''$ [52] gives $\alpha_s(M_Z) = 0.113 \pm 0.001(\text{exp.})$. There is an uncertainty of ± 0.005 from the choice of the μ scale, and slightly larger uncertainties due to the relativistic corrections.

The CLEO collaboration measured the strong coupling [53] from the ratio $\Gamma(\Upsilon \rightarrow gg\gamma)/\Gamma(\Upsilon \rightarrow ggg)$, which to leading order is proportional to α_{em}/α_s . The result at the scale of the Υ mass (9.45 GeV) is $\alpha_s(9.45 \text{ GeV}) = 0.163 \pm 0.002(\text{exp.}) \pm 0.014(\text{theory})$. The error is dominated by the uncertainty on the scale and a small uncertainty due to the photon production in fragmentation. The value corresponding to the M_Z scale is $\alpha_s(M_Z) = 0.110 \pm 0.001 \pm 0.007$.

Lattice Gauge Theory

Lattice gauge theory currently provides a successful tool for performing non-perturbative QCD calculations, although it is limited in applicability to static properties of hadrons. Experimental data on hadron properties, such as energy-

levels of $Q\bar{Q}$ systems, can be determined and used to extract α_s . Currently the precision of such determinations of α_s is limited by various theoretical uncertainties relating to lattice discretisation, treatment of “sea quarks”, and matching between different renormalization schemes used in lattice and perturbative calculations. Combination of results from the $n_f=0$ and $n_f=2$ approximations gives an average $\alpha_s(M_Z) = 0.116 \pm 0.003$ [54].

8.1.4 Hadron-Hadron Collisions

Determinations of α_s at hadron colliders have been performed by comparing direct photon, heavy quark and W boson plus jet cross section with next-to-leading order predictions. So far, the precision achieved in hadron-hadron determinations has been less than in e^+e^- annihilation. First of all, there are extra uncertainties associated with the parton distributions of incoming partons. The hadronic final state is also more complex, containing not only the products of hard subprocesses but also the soft remnants of spectator partons. Furthermore in most cases the nature and kinematics of the hard subprocesses are less well known.

$(W + 1\text{-jet})/(W + 0\text{-jet})$ Ratio in $p\bar{p}$ Collisions

Several experimental collaborations have attempted to determine α_s from the ratio R of the cross section for production of final states containing a W boson +1-jet and a W boson +0-jets; R is proportional to α_s at leading order, and many sources of experimental uncertainty are expected to cancel. The UA2 collaboration [55] determined α_s from these measurements, but their result has large uncertainties, since it depends on the details of the jet algorithm and is sensitive to fragmentation and underlying event corrections.

The D0 collaboration [56] also used the R ratio to measure α_s from Tevatron data, but it turned out to be rather insensitive to α_s , since for larger values of α_s the reduction of the structure functions in the evolution almost compensates the increased jet production rates from the matrix elements.

Direct Photon Production in pp and $p\bar{p}$ Collisions

Prompt photon production in hard parton-parton scattering is a Compton-like process of $\mathcal{O}(\alpha_{em}\alpha_s)$. The measurement in the same experiment of the production of direct photons in pp and $p\bar{p}$ collisions allows a clean isolation of the annihilation process ($q\bar{q} \rightarrow \gamma g$) from the difference $\sigma(p\bar{p} \rightarrow \gamma X) - \sigma(pp \rightarrow \gamma X)$. Using parton distribution functions fitted to BCDMS data, the UA6 collaboration obtains $\alpha_s(M_Z) = 0.1112 \pm 0.0016(stat.) \pm 0.0033(syst.)^{+0.0077}_{-0.0034} (theory)$. The error is dominated by the choice of μ scale [57].

8.2 Discussion of Results and Future Outlook

Quantum Chromodynamics has established itself as a theory of strong interactions. Today, studies of QCD left the phase of *tests* and moved to the stage of precision measurements. Since the strong coupling constant is the only fundamental parameter of QCD measured from experiments, there is no limit to the accuracy at which we want to measure it. New developments in the analytical and phenomenological understanding of the uncertainties in α_s measurements, for example from event shapes, is amazing. The incredible progress in this area is a proof that theoretical development is moving in the right direction. At the same time, this sets a stage for progress in precision QCD measurements from hadron colliders, which was difficult

to imagine just a few years ago.

Hadron colliders have a great potential to extend measurements of α_s to large values of the momentum transfer scale Q^2 and to considerably reduce the statistical uncertainties. Our measurement of α_s extends to approximately 450 GeV, providing values of α_s for energy ranges never measured before (Fig. 8.1). This is the first measurement of α_s coming from the Tevatron, which can be included in a fit for a world average of α_s . Since this measurement demonstrated that Tevatron results can be used to measure the strong coupling constant, the stage is prepared for new analyses at CDF on α_s extraction with jet data, for example based on energy partitions in 3-jet systems.

The precision of the measurement is comparable with other experiments, although it is not on the same footing as the results based on Z width measurements in e^+e^- annihilation. The main theoretical uncertainties studied in this thesis are the choice of renormalization scale, which is also the dominant uncertainty on many results discussed above, and the choice of parton distribution functions, which also affects α_s extraction from jet production at HERA.

As mentioned before, the major advantage of this measurement is the large range of scales covered. We were able to test and prove the running of the coupling constant in the *same* experiment, from the *same* set of experimental data over an E_T range from 45 to 420 GeV. To compare with the other experiments which were able to show the running of α_s : the HERA experiments reported evolution of α_s in the range of 7-50 GeV, and recent LEP results cover the range from 30 to 183 GeV.

The average value of $\alpha_s(M_Z)$ obtained from the error weighted contributions of our 33 measurements of $\alpha_s(M_Z)$ as a function of E_T is consistent with the new

world average [60]:

$$\alpha_s(M_Z)^{CDFaverage} = 0.1129 \pm 0.0001(\text{exp.stat.})^{+0.0078}_{-0.0089}(\text{exp.syst.}) \pm 0.0056(\text{theor.scale}) \pm 0.0113(\text{theor.PDF}), \quad (8.8)$$

$$\alpha_s(M_Z)^{world\ average\ 1999} = 0.119 \pm 0.003. \quad (8.9)$$

As discussed before the theoretical error from the choice of renormalization scale could be correctly estimated only from the comparison of NLO and NNLO predictions. The latter are not yet available for jet production at hadron colliders. We can therefore only estimate the sensitivity of our measurement to the choice of μ_R , which is at the level of $\pm 5\%$. The uncertainty due to the choice of PDF is estimated to be of the order of 10%. New developments in α_s measurements, which will be discussed later, and new constraints on the gluon distribution functions should reduced those uncertainties.

8.2.1 Future Plans

Hadron colliders have an impressive potential for measurements of α_s , and the first steps started with this analysis should be continued, especially with the perspective of higher energy runs at the Tevatron.

The future of this measurement lies with developments in two directions. The first possibility is to extract both α_s and gluon distribution functions from the same data set. This could be done by using the triply differential cross section:

$$\frac{d\sigma}{dE_T d\eta_1 d\eta_2} \propto \alpha_s^2 [f_{g_1}(x_1)f_{g_2}(x_2)A_{gg}(\eta) + f_{g_1}(x_1)f_{g_2}(x_2)A_{gq}(\eta) + f_{g_1}(x_1)f_{g_2}(x_2)A_{qq}(\eta)], \quad (8.10)$$

$$\eta = \frac{\eta_1 - \eta_2}{2}, \quad (8.11)$$

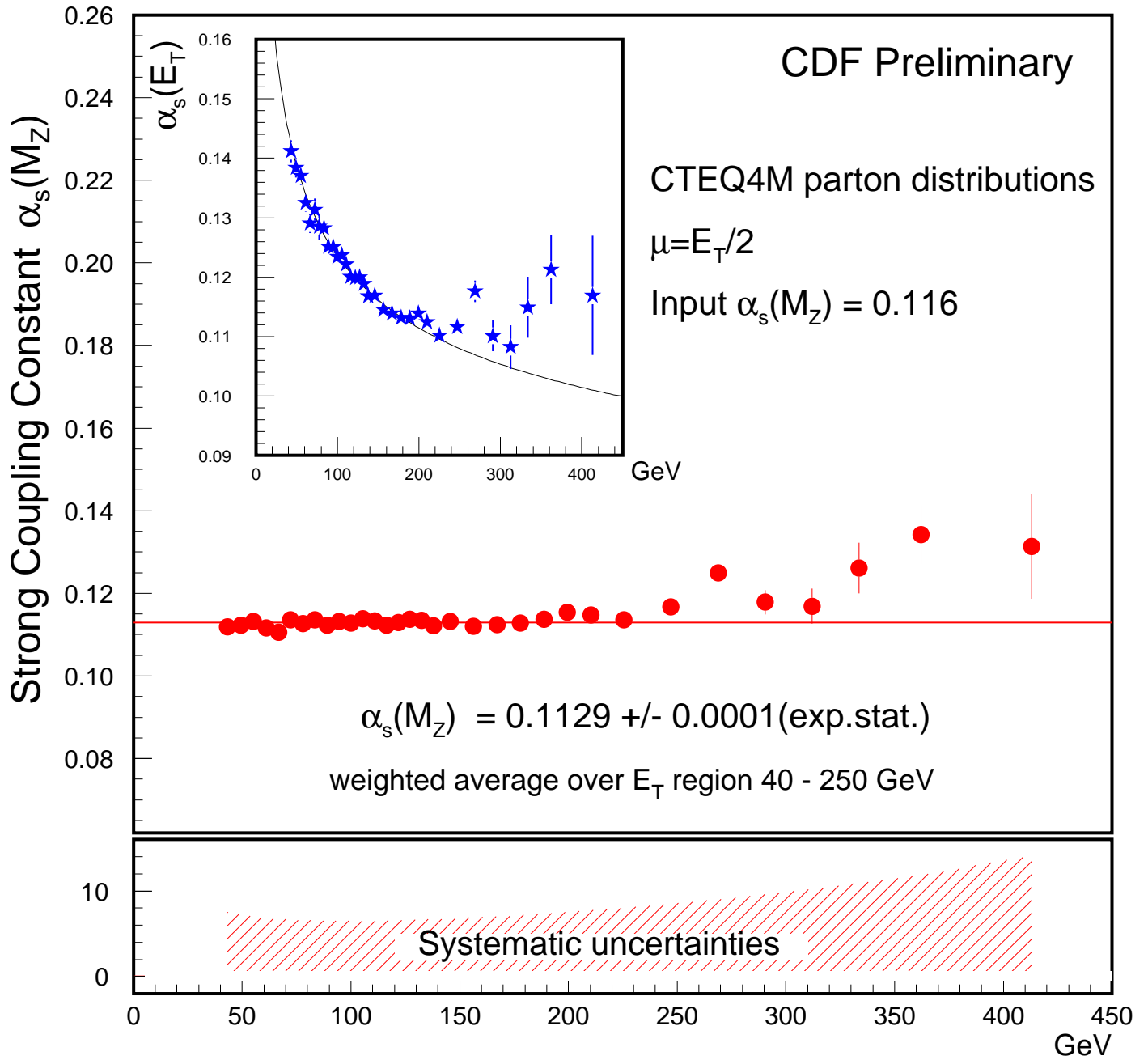


Figure 8.1: α_s measurement using CTEQ4M parton distributions.

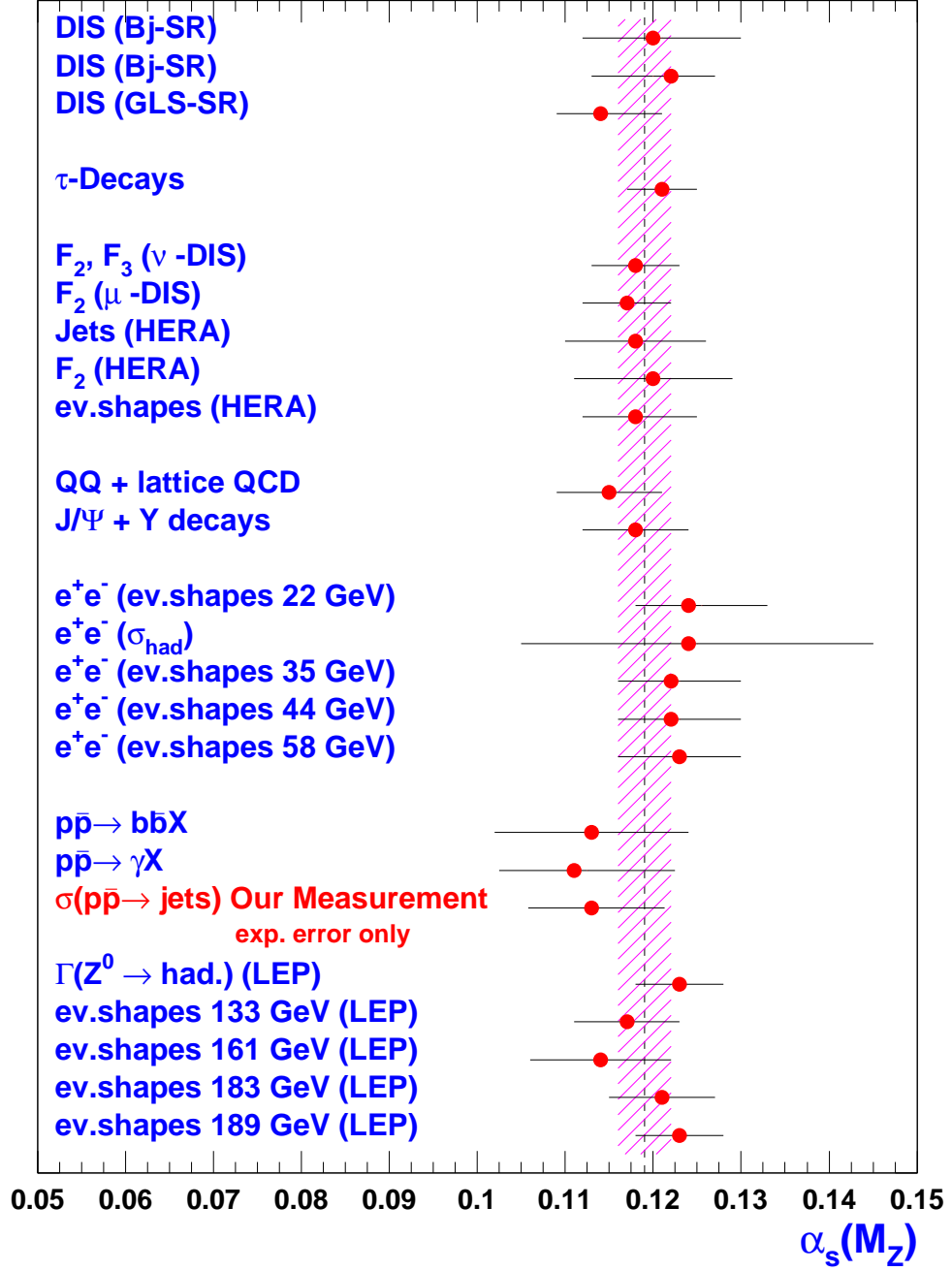


Figure 8.2: Summary of different measurements of $\alpha_s(M_Z)$. The dashed line corresponds to the world average of $\alpha_s(M_Z)$ with shaded band representing the uncertainty on this value.

$$x_{1,2} = \frac{2E_T}{\sqrt{s}}(e^{\pm\eta_1} + e^{\pm\eta_2}). \quad (8.12)$$

and simultaneously constraining α_s , the gluon distribution function $f_g(x, Q^2)$ and the non-singlet quark distribution function $F_2(x, Q^2)$, thus removing the uncertainty due to the poorly constrained parton distribution functions.

The second way is to extract α_s by means of a method recently suggested by Walter Giele and S. Keller [58]. The principal shortcoming of parton distribution functions obtained from global fits is that they come without an estimate of their uncertainties. At the same time these uncertainties are needed in the interpretation of the Tevatron data. The authors based their new method on the framework of statistical inference [59], which allows efficiently propagate uncertainties to new observables, assess compatibility with data and include new data in the fit. The method allows to include statistical and systematic experimental uncertainties with a point-to-point correlation matrix as well as theoretical uncertainties into the fit. The uncertainties do not need to be the Gaussian. Data sets can easily be included or excluded to investigate the effect of different experiments on the PDF of interest. This method makes it possible to extract α_s from different sets of experimental data, or from the inclusive jet spectrum only, allowing for rigorous studies of uncertainties.

The methods discussed have the potential of establishing Tevatron experiments as the source of new precision QCD measurements.

CDF COLLABORATION

T. Affolder,²¹ H. Akimoto,⁴³ A. Akopian,³⁶ M. G. Albrow,¹⁰ P. Amaral,⁷
S. R. Amendolia,³² D. Amidei,²⁴ K. Anikeev,²² J. Antos,¹ G. Apollinari,³⁶
T. Arisawa,⁴³ T. Asakawa,⁴¹ W. Ashmanskas,⁷ M. Atac,¹⁰ F. Azfar,²⁹ P. Azzi-
Bacchetta,³⁰ N. Bacchetta,³⁰ M. W. Bailey,²⁶ S. Bailey,¹⁴ P. de Barbaro,³⁵ A. Barbaro-
Galtieri,²¹ V. E. Barnes,³⁴ B. A. Barnett,¹⁷ M. Barone,¹² G. Bauer,²² F. Bedeschi,³²
S. Belforte,⁴⁰ G. Bellettini,³² J. Bellinger,⁴⁴ D. Benjamin,⁹ J. Bensinger,⁴
A. Beretvas,¹⁰ J. P. Berge,¹⁰ J. Berryhill,⁷ B. Bevensee,³¹ A. Bhatti,³⁶ M. Binkley,¹⁰
D. Bisello,³⁰ R. E. Blair,² C. Blocker,⁴ K. Bloom,²⁴ B. Blumenfeld,¹⁷ S. R. Blusk,³⁵
A. Bocci,³² A. Bodek,³⁵ W. Bokhari,³¹ G. Bolla,³⁴ Y. Bonushkin,⁵ D. Bortoletto,³⁴
J. Boudreau,³³ A. Brandl,²⁶ S. van den Brink,¹⁷ C. Bromberg,²⁵ M. Brozovic,⁹
N. Bruner,²⁶ E. Buckley-Geer,¹⁰ J. Budagov,⁸ H. S. Budd,³⁵ K. Burkett,¹⁴
G. Busetto,³⁰ A. Byon-Wagner,¹⁰ K. L. Byrum,² M. Campbell,²⁴ W. Carithers,²¹
J. Carlson,²⁴ D. Carlsmith,⁴⁴ J. Cassada,³⁵ A. Castro,³⁰ D. Cauz,⁴⁰ A. Cerri,³²
A. W. Chan,¹ P. S. Chang,¹ P. T. Chang,¹ J. Chapman,²⁴ C. Chen,³¹ Y. C. Chen,¹
M. -T. Cheng,¹ M. Chertok,³⁸ G. Chiarelli,³² I. Chirikov-Zorin,⁸ G. Chlachidze,⁸
F. Chlebana,¹⁰ L. Christofek,¹⁶ M. L. Chu,¹ S. Cihangir,¹⁰ C. I. Ciobanu,²⁷
A. G. Clark,¹³ A. Connolly,²¹ J. Conway,³⁷ J. Cooper,¹⁰ M. Cordelli,¹² J. Cranshaw,³⁹
D. Cronin-Hennessy,⁹ R. Cropp,²³ R. Culbertson,⁷ D. Dagenhart,⁴² F. DeJongh,¹⁰
S. Dell'Agnello,¹² M. Dell'Orso,³² R. Demina,¹⁰ L. Demortier,³⁶ M. Deninno,³
P. F. Derwent,¹⁰ T. Devlin,³⁷ J. R. Dittmann,¹⁰ S. Donati,³² J. Done,³⁸ T. Dorigo,¹⁴
N. Eddy,¹⁶ K. Einsweiler,²¹ J. E. Elias,¹⁰ E. Engels, Jr.,³³ W. Erdmann,¹⁰ D. Errede,¹⁶
S. Errede,¹⁶ Q. Fan,³⁵ R. G. Feild,⁴⁵ C. Ferretti,³² R. D. Field,¹¹ I. Fiori,³
B. Flaughner,¹⁰ G. W. Foster,¹⁰ M. Franklin,¹⁴ J. Freeman,¹⁰ J. Friedman,²² Y. Fukui,²⁰

S. Galeotti,³² M. Gallinaro,³⁶ T. Gao,³¹ M. Garcia-Sciveres,²¹ A. F. Garfinkel,³⁴
 P. Gatti,³⁰ C. Gay,⁴⁵ S. Geer,¹⁰ D. W. Gerdes,²⁴ P. Giannetti,³² P. Giromini,¹²
 V. Glagolev,⁸ M. Gold,²⁶ J. Goldstein,¹⁰ A. Gordon,¹⁴ A. T. Goshaw,⁹ Y. Gotra,³³
 K. Goulianos,³⁶ C. Green,³⁴ L. Groer,³⁷ C. Grosso-Pilcher,⁷ M. Guenther,³⁴
 G. Guillian,²⁴ J. Guimaraes da Costa,²⁴ R. S. Guo,¹ C. Haber,²¹ E. Hafen,²²
 S. R. Hahn,¹⁰ C. Hall,¹⁴ T. Handa,¹⁵ R. Handler,⁴⁴ W. Hao,³⁹ F. Happacher,¹²
 K. Hara,⁴¹ A. D. Hardman,³⁴ R. M. Harris,¹⁰ F. Hartmann,¹⁸ K. Hatakeyama,³⁶
 J. Hauser,⁵ J. Heinrich,³¹ A. Heiss,¹⁸ M. Herndon,¹⁷ B. Hinrichsen,²³ K. D. Hoffman,³⁴
 C. Holck,³¹ R. Hollebeek,³¹ L. Holloway,¹⁶ R. Hughes,²⁷ J. Huston,²⁵ J. Huth,¹⁴
 H. Ikeda,⁴¹ J. Incandela,¹⁰ G. Introzzi,³² J. Iwai,⁴³ Y. Iwata,¹⁵ E. James,²⁴
 H. Jensen,¹⁰ M. Jones,³¹ U. Joshi,¹⁰ H. Kambara,¹³ T. Kamon,³⁸ T. Kaneko,⁴¹
 K. Karr,⁴² H. Kasha,⁴⁵ Y. Kato,²⁸ T. A. Keaffaber,³⁴ K. Kelley,²² M. Kelly,²⁴
 R. D. Kennedy,¹⁰ R. Kephart,¹⁰ D. Khazins,⁹ T. Kikuchi,⁴¹ M. Kirk,⁴ B. J. Kim,¹⁹
 H. S. Kim,¹⁶ M. J. Kim,¹⁹ S. H. Kim,⁴¹ Y. K. Kim,²¹ L. Kirsch,⁴ S. Klimenko,¹¹
 P. Koehn,²⁷ A. Köngeter,¹⁸ K. Kondo,⁴³ J. Konigsberg,¹¹ K. Kordas,²³ A. Korn,²²
 A. Korytov,¹¹ E. Kovacs,² J. Kroll,³¹ M. Kruse,³⁵ S. E. Kuhlmann,² K. Kurino,¹⁵
 T. Kuwabara,⁴¹ A. T. Laasanen,³⁴ N. Lai,⁷ S. Lami,³⁶ S. Lammel,¹⁰ J. I. Lamoureux,⁴
 M. Lancaster,²¹ G. Latino,³² T. LeCompte,² A. M. Lee IV,⁹ S. Leone,³² J. D. Lewis,¹⁰
 M. Lindgren,⁵ T. M. Liss,¹⁶ J. B. Liu,³⁵ Y. C. Liu,¹ N. Lockyer,³¹ J. Loken,²⁹
 M. Loreti,³⁰ D. Lucchesi,³⁰ P. Lukens,¹⁰ S. Lusin,⁴⁴ L. Lyons,²⁹ J. Lys,²¹ R. Madrak,¹⁴
 K. Maeshima,¹⁰ P. Maksimovic,¹⁴ L. Malferrari,³ M. Mangano,³² M. Mariotti,³⁰
 G. Martignon,³⁰ A. Martin,⁴⁵ J. A. J. Matthews,²⁶ J. Mayer,²³ P. Mazzanti,³
 K. S. McFarland,³⁵ P. McIntyre,³⁸ E. McKigney,³¹ M. Menguzzato,³⁰ A. Menzione,³²
 C. Mesropian,³⁶ T. Miao,¹⁰ R. Miller,²⁵ J. S. Miller,²⁴ H. Minato,⁴¹ S. Miscetti,¹²
 M. Mishina,²⁰ G. Mitselmakher,¹¹ N. Moggi,³ C. Moore,¹⁰ E. Moore,²⁶ R. Moore,²⁴

Y. Morita,²⁰ A. Mukherjee,¹⁰ T. Muller,¹⁸ A. Munar,³² P. Murat,¹⁰ S. Murgia,²⁵
 M. Musy,⁴⁰ J. Nachtman,⁵ S. Nahn,⁴⁵ H. Nakada,⁴¹ T. Nakaya,⁷ I. Nakano,¹⁵
 C. Nelson,¹⁰ D. Neuberger,¹⁸ C. Newman-Holmes,¹⁰ C.-Y. P. Ngan,²² P. Nicolaidi,⁴⁰
 H. Niu,⁴ L. Nodulman,² A. Nomerotski,¹¹ S. H. Oh,⁹ T. Ohmoto,¹⁵ T. Ohsugi,¹⁵
 R. Oishi,⁴¹ T. Okusawa,²⁸ J. Olsen,⁴⁴ C. Pagliarone,³² F. Palmonari,³² R. Paoletti,³²
 V. Papadimitriou,³⁹ S. P. Pappas,⁴⁵ D. Partos,⁴ J. Patrick,¹⁰ G. Pauletta,⁴⁰
 M. Paulini,²¹ C. Paus,²² L. Pescara,³⁰ T. J. Phillips,⁹ G. Piacentino,³² K. T. Pitts,¹⁶
 R. Plunkett,¹⁰ A. Pompos,³⁴ L. Pondrom,⁴⁴ G. Pope,³³ M. Popovic,²³ F. Prokoshin,⁸
 J. Proudfoot,² F. Ptohos,¹² G. Punzi,³² K. Ragan,²³ A. Rakitine,²² D. Reher,²¹
 A. Reichold,²⁹ W. Riegler,¹⁴ A. Ribon,³⁰ F. Rimondi,³ L. Ristori,³² W. J. Robertson,⁹
 A. Robinson,²³ T. Rodrigo,⁶ S. Rolli,⁴² L. Rosenson,²² R. Roser,¹⁰ R. Rossin,³⁰
 W. K. Sakumoto,³⁵ D. Saltzberg,⁵ A. Sansoni,¹² L. Santi,⁴⁰ H. Sato,⁴¹ P. Savard,²³
 P. Schlabach,¹⁰ E. E. Schmidt,¹⁰ M. P. Schmidt,⁴⁵ M. Schmitt,¹⁴ L. Scodellaro,³⁰
 A. Scott,⁵ A. Scribano,³² S. Segler,¹⁰ S. Seidel,²⁶ Y. Seiya,⁴¹ A. Semenov,⁸ F. Semeria,³
 T. Shah,²² M. D. Shapiro,²¹ P. F. Shepard,³³ T. Shibayama,⁴¹ M. Shimojima,⁴¹
 M. Shochet,⁷ J. Siegrist,²¹ G. Signorelli,³² A. Sill,³⁹ P. Sinervo,²³ P. Singh,¹⁶
 A. J. Slaughter,⁴⁵ K. Sliwa,⁴² C. Smith,¹⁷ F. D. Snider,¹⁰ A. Solodsky,³⁶ J. Spalding,¹⁰
 T. Speer,¹³ P. Sphicas,²² F. Spinella,³² M. Spiropulu,¹⁴ L. Spiegel,¹⁰ J. Steele,⁴⁴
 A. Stefanini,³² J. Strologas,¹⁶ F. Strumia,¹³ D. Stuart,¹⁰ K. Sumorok,²² T. Suzuki,⁴¹
 T. Takano,²⁸ R. Takashima,¹⁵ K. Takikawa,⁴¹ P. Tamburello,⁹ M. Tanaka,⁴¹
 B. Tannenbaum,⁵ W. Taylor,²³ M. Tecchio,²⁴ P. K. Teng,¹ K. Terashi,⁴¹ S. Tether,²²
 D. Theriot,¹⁰ R. Thurman-Keup,² P. Tipton,³⁵ S. Tkaczyk,¹⁰ K. Tollefson,³⁵
 A. Tollestrup,¹⁰ H. Toyoda,²⁸ W. Trischuk,²³ J. F. de Troconiz,¹⁴ J. Tseng,²²
 N. Turini,³² F. Ukegawa,⁴¹ T. Vaiciulis,³⁵ J. Valls,³⁷ S. Vejck III,¹⁰ G. Velez,¹⁰
 R. Vidal,¹⁰ R. Vilar,⁶ I. Volobouev,²¹ D. Vucinic,²² R. G. Wagner,² R. L. Wagner,¹⁰

J. Wahl,⁷ N. B. Wallace,³⁷ A. M. Walsh,³⁷ C. Wang,⁹ C. H. Wang,¹ M. J. Wang,¹
T. Watanabe,⁴¹ D. Waters,²⁹ T. Watts,³⁷ R. Webb,³⁸ H. Wenzel,¹⁸ W. C. Wester III,¹⁰
A. B. Wicklund,² E. Wicklund,¹⁰ H. H. Williams,³¹ P. Wilson,¹⁰ B. L. Winer,²⁷
D. Winn,²⁴ S. Wolbers,¹⁰ D. Wolinski,²⁴ J. Wolinski,²⁵ S. Wolinski,²⁴ S. Worm,²⁶
X. Wu,¹³ J. Wyss,³² A. Yagil,¹⁰ W. Yao,²¹ G. P. Yeh,¹⁰ P. Yeh,¹ J. Yoh,¹⁰ C. Yosef,²⁵
T. Yoshida,²⁸ I. Yu,¹⁹ S. Yu,³¹ A. Zanetti,⁴⁰ F. Zetti,²¹ and S. Zucchelli³

(CDF Collaboration)

¹ *Institute of Physics, Academia Sinica, Taipei, Taiwan 11529, Republic of China*

² *Argonne National Laboratory, Argonne, Illinois 60439*

³ *Istituto Nazionale di Fisica Nucleare, University of Bologna, I-40127 Bologna, Italy*

⁴ *Brandeis University, Waltham, Massachusetts 02254*

⁵ *University of California at Los Angeles, Los Angeles, California 90024*

⁶ *Instituto de Fisica de Cantabria, University of Cantabria, 39005 Santander, Spain*

⁷ *Enrico Fermi Institute, University of Chicago, Chicago, Illinois 60637*

⁸ *Joint Institute for Nuclear Research, RU-141980 Dubna, Russia*

⁹ *Duke University, Durham, North Carolina 27708*

¹⁰ *Fermi National Accelerator Laboratory, Batavia, Illinois 60510*

¹¹ *University of Florida, Gainesville, Florida 32611*

¹² *Laboratori Nazionali di Frascati, Istituto Nazionale di Fisica Nucleare, I-00044 Frascati, Italy*

¹³ *University of Geneva, CH-1211 Geneva 4, Switzerland*

¹⁴ *Harvard University, Cambridge, Massachusetts 02138*

¹⁵ *Hiroshima University, Higashi-Hiroshima 724, Japan*

¹⁶ *University of Illinois, Urbana, Illinois 61801*

¹⁷ *The Johns Hopkins University, Baltimore, Maryland 21218*

- ¹⁸ *Institut für Experimentelle Kernphysik, Universität Karlsruhe, 76128 Karlsruhe, Germany*
- ¹⁹ *Korean Hadron Collider Laboratory: Kyungpook National University, Taegu 702-701; Seoul National University, Seoul 151-742; and SungKyunKwan University, Suwon 440-746; Korea*
- ²⁰ *High Energy Accelerator Research Organization (KEK), Tsukuba, Ibaraki 305, Japan*
- ²¹ *Ernest Orlando Lawrence Berkeley National Laboratory, Berkeley, California 94720*
- ²² *Massachusetts Institute of Technology, Cambridge, Massachusetts 02139*
- ²³ *Institute of Particle Physics: McGill University, Montreal H3A 2T8; and University of Toronto, Toronto M5S 1A7; Canada*
- ²⁴ *University of Michigan, Ann Arbor, Michigan 48109*
- ²⁵ *Michigan State University, East Lansing, Michigan 48824*
- ²⁶ *University of New Mexico, Albuquerque, New Mexico 87131*
- ²⁷ *The Ohio State University, Columbus, Ohio 43210*
- ²⁸ *Osaka City University, Osaka 588, Japan*
- ²⁹ *University of Oxford, Oxford OX1 3RH, United Kingdom*
- ³⁰ *Universita di Padova, Istituto Nazionale di Fisica Nucleare, Sezione di Padova, I-35131 Padova, Italy*
- ³¹ *University of Pennsylvania, Philadelphia, Pennsylvania 19104*
- ³² *Istituto Nazionale di Fisica Nucleare, University and Scuola Normale Superiore of Pisa, I-56100 Pisa, Italy*
- ³³ *University of Pittsburgh, Pittsburgh, Pennsylvania 15260*
- ³⁴ *Purdue University, West Lafayette, Indiana 47907*
- ³⁵ *University of Rochester, Rochester, New York 14627*
- ³⁶ *Rockefeller University, New York, New York 10021*
- ³⁷ *Rutgers University, Piscataway, New Jersey 08855*
- ³⁸ *Texas A&M University, College Station, Texas 77843*
- ³⁹ *Texas Tech University, Lubbock, Texas 79409*
- ⁴⁰ *Istituto Nazionale di Fisica Nucleare, University of Trieste/ Udine, Italy*

⁴¹ *University of Tsukuba, Tsukuba, Ibaraki 305, Japan*

⁴² *Tufts University, Medford, Massachusetts 02155*

⁴³ *Waseda University, Tokyo 169, Japan*

⁴⁴ *University of Wisconsin, Madison, Wisconsin 53706*

⁴⁵ *Yale University, New Haven, Connecticut 06520*

Bibliography

- [1] W. Giele *et al.*, Phys. Rev. **D 53**, 120 (1996).
- [2] Particle Data Group Review of Particle Properties 2000.
- [3] C. Mesropian, to be published in the proceedings of XXXIV Rencontres de Moriond, Les Arcs, France (Mar. 1999), FERMILAB-CONF-99-177-E.
- [4] M. Wobisch, International Conference on High Energy Physics (ICHEP'98), Vancouver, Canada (July 1998), hep-ph/9811210.
- [5] J. Womersley, International Conference on Lepton Photon Interactions, Stanford, USA (Aug. 1999), FERMILAB-CONF-99-353.
- [6] M. Gell-Mann, Phys. Lett. **8**, 214 (1964); Zweig G. CERN Rep. , **TH 401,412** unpublished
- [7] O. Greenberg, Phys. Rev. Lett. **13**, 598 (1964); M. Han, Y. Nambu, Phys. Rev. **B 139**, 1006 (1965).
- [8] M. Gell-Mann, Caltech-Report CTSL-20, (1961);
Y. Ne'eman, Nucl. Phys. **26**, 222 (1961).
- [9] R.P. Feynman, Phys. Rev. Lett. **23**, 1415 (1969); R.P. Feynman, Photon-Hadron Interactions, 1972.

- [10] C.N. Yang and R.L.Mills, Phys. Rev. **96**, 191 (1954).
- [11] G. 't Hooft, unpublished; D. Gross, F. Wilczek, Phys. Rev. Lett. **30**, 1343 (1973); H. Politzer, Phys. Rev. Lett. **30**, 1346 (1973).
- [12] E.C.G. Stueckelber and A. Peterman, Helv. Phys. Acta **26**, 499 (1953);
M. Gell-Mann and F.E. Low, Phys. Rev. **95**, 1300 (1954);
N.N. Bogoliubov and D.V. Shirkov, Dokl. Akad. Nauk SSSR **103**, 203 (1955);
K. Wilson, Phys. Rev. **179**, 1499 (1969);
C.G. Callan, Phys. Rev. **D 2**, 1541 (1970);
K. Symanzik, Comm. Math. Phys. **18**, 227 (1970).
- [13] L. Faddeev and V.N. Popov, Phys. Lett. **B 25**, 29 (1967).
- [14] Y. L. Dokshitzer *et al.*, Phys. Rep. **58 C**, 271 (1980).
- [15] F. Abe *et al.*, Nucl. Instr. and Meth. **A 271**(387) 1988.
- [16] P. Azzi *et al.*, Nucl. Instr. and Meth. **A 360**(137) 1995.
- [17] F. Snider *et al.*, Nucl. Instr. and Meth. **A 268**(75) 1988.
- [18] F. Bedeschi *et al.*, Nucl. Instr. and Meth. **A 268**(50) 1988.
- [19] L. Balka *et al.*, Nucl. Instr. and Meth. **A 267**(272) 1988; S. Bertolucci *et al.*,
Nucl. Instr. and Meth. **A 267**(301) 1988.
- [20] Y. Fukui *et al.*, Nucl. Instr. and Meth. **A 267**(280) 1988; G. Branderburg *et al.*,
Nucl. Instr. and Meth. **A 267**(257) 1988; S. Cihangir *et al.*, Nucl. Instr.
and Meth. **A 267**(249) 1988.

- [21] G. Ascoli *et al.*, Nucl. Instr. and Meth. **A 268**(33) 1988; K. Byrum *et al.*, Nucl. Instr. and Meth. **A 268**(46) 1988.
- [22] J. Jackson and J. Crawford, Fermilab's Collider Run I, FermiNews, Vol. 19, No.5, March 8, 1996.
- [23] P.N. Burrows *et al.*, hep-ex/9612012.
- [24] G. Hanson *et al.*, Phys. Rev. Lett. **35**, 1609 (1975); D.P.Barber *et al.*, Phys. Rev. Lett. **43**, 830 (1979).
- [25] M. Banner *et al.*, Phys. Lett. **B 118**, 203 (1982); F. Abe *et al.*, Phys. Rev. Lett. **70**, 1376 (1993).
- [26] J. Huth *et al.*, "Research Directions for the Decade : Proceedings of the 1990 Summer Study on High Energy Physics ", ed. E. Berger, Singapore: World Scientific, 134 (1992).
- [27] R.K. Ellis and J. Sexton, Nucl.Phys.**B269** 445 (1986).
- [28] S.D Ellis *et al.*, Phys. Rev. **D 46**, 192 (1992).
- [29] W. Giele *et al.*, Nucl. Phys. **B403**, 633 (1993).
- [30] R.K. Ellis and J. Sexton, Nucl. Phys. **B269**, 445 (1986).
- [31] F. Abe *et al.*, Phys. Rev. Lett. **70**, 1376 (1993).
- [32] F. Abe *et al.*, Phys. Rev. **D 45**, 1448 (1992).
- [33] T. Hessing and S. Behrends, Internal CDF Note **1132**.
- [34] F. Abe *et al.*, Phys. Rev. Lett. **68**, 1104 (1992).

- [35] F. James, MINUIT (Function Minimization and Error Analysis) Reference Manual, CERN Program Library, **D506**.
- [36] H.D. Politzer, Phys. Rev. Lett. **30**, 1346 (1973); D.J. Gross and F. Wilczek, Phys. Rev. Lett. **30**, 1343 (1973); W.A. Caswell, Phys. Rev. Lett. **33**, 244 (1974); O.V Tarasov *et al.*, Phys. Lett. **B 93**, 429 (1980); S.A. Larin and J.A.M. Vermaseren, Phys. Lett. **B 303**, 334 (1993).
- [37] T. Applequist and J. Carazzone, Phys. Rev. **D 11**, 2856 (1975).
- [38] to be submitted to Phys. Rev. **D**, A.A. Bhatti Internal CDF Note **4678**.
- [39] G.C. Blazey and B.L. Flaugher, hep-ex/9903058, Ann. Rev. Nucl. Part. Sci. **49** (1999).
- [40] J.A. Crittenden, Proceedings of the EPIC'99 Workshop on Physics with an Electron/Polarized-Ion Collider, (1999);
K. Goulianos, Pub. Proceedings 34th Rencontres de Moriond: QCD and Hadronic Interactions, (1999).
- [41] H.L. Lai *et al.*, Phys. Rev. **D 55**, 1280 (1997).
- [42] A.D. Martin, R.G. Roberts, and W.J. Stirling, Phys. Lett. **B 354**, 154 (1995).
- [43] A.D. Martin *et al.*, hep-ph/9606345.
- [44] A.D. Martin *et al.*, hep-ph/9803445, *Eur. Phys. J. C* **4**, 463 (1998).
- [45] R. Ammar *et al.*, Phys. Rev. **D 57**, 1350 (1998).
- [46] G. Quast, presented at the 1999 EPS Conference, July 1999.
- [47] S. Bethke *et al.*, Phys. Lett. **B 213**, 235 (1988).

- [48] S. Catani *et al.*, Phys. Lett. **B 269**, 432 (1991).
- [49] DELPHI Collaboration, DELPHI 98-84 CONF 152.
- [50] J. Kim *et al.*, Phys. Rev. Lett. **81**, 3595 (1998).
- [51] T. Ahmed *et al.*, Phys. Lett. **B 346**, 415 (1995);
M. Derrick *et al.*, Phys. Lett. **B 363**, 201 (1995).
- [52] M. Kobel, DESY-F31-91-03 (thesis).
- [53] B. Nemati *et al.*, Phys. Rev. **D 55**, 5273 (1997).
- [54] J. Shigemitsu, *Nucl. Phys.* **B53** (Proc.Supp.), 16 (1997).
- [55] J. Alitti *et al.*, Phys. Lett. **B 263**, 563 (1991);
- [56] S. Abachi *et al.*, ICHEP conference, Warsaw, July 1996.
- [57] M. Werlen *et al.*, Phys. Lett. **B 452**, 201 (1999).
- [58] W. Giele and S. Keller, Phys. Rev. **D 58**, 094023 (1998).
- [59] G. D'Agostini, CERN Yellow Report 99-03.
- [60] S. Bethke, hep-ex/0001023.